eman ta zabal zazu

Universidad del País Vasco
Euskal Herriko Unibertsitatea

In-device spectroscopy at metal/organic semiconductor interfaces

Ainhoa Atxabal Arrasate

PhD Thesis

Supervisors: Prof. L. E. Hueso & Prof. F. Casanova

2018


CIC
nanoGUNE
nanoscience cooperative research center

Laburpena

1987an W. Tang eta S. van Slykek Estman Kodaken lehen erdieroale organikozko diodoa produzitu zuten eta honela elektronika molekularrari hasiera emanez. Alor berri hau fisikaren eta materialen zientziaren ezaguerez baliatuz propietate elektronikoak diztuzten molekula txiki eta polimeroen diseinu, sintesi, karakterizazio eta aplikazioetan datza. Erdieroale ez-organikoekin alderatuz material organiko edo molekularrek dituzten abantailak direla eta, interes handia piztu da gaiaren inguruan. Ikuspuntu teknologikotik, konposatu organikoak koste baxuko elektrononika produzitzeko estartegia direla dirudite, errez prozesatu baitaitezke esaterako plastikoa, beira edo metalezko harila bezalako substratu merkeetan. Horretaz gain, ez-purutasunek ez dute zertan ordezko defektu aktiborik sortzen eta beraz, material organiko batzuk huts ultra-altutik kanpo (ingelesez ultra-high vacuum, UHV) prozesatu daitezke. Horrela bada, materialak hutsetik kanpora manipula ahal izateak gailu elektronikoen produkzio kostua jaizten du. Hori baino zehatzago, arte grafikoetan eta industrian erabiltzen diren inprimatze teknikak elektronika molekularraren eskala handiko produkziorako egokitzea posible lirateke. Bestalde, molekula organikoen funtzionaltasuna maila molekularrean moldatu daiteke. Hau da, unitate molekularren aldaketa txikiek propietate elektroniko zein optikoak aldatu ditzazkete. Honek, goraka ari den industria teknologikoaren behar izanak betetzeko beharrezkoak diren propietateak espezifikoak dituzten molekulak diseinatzea ahalbidetzen du.

Material organikoetan oinarraturiko gailu (opto-)elektronikoak diseinatzeko molekulen inguruko hainbat parametro ezagutzea beharrezkoa da. Parametro horien artean garraiozko energia-tartea (transport energy gap ingelesez, garraioko E_G) eta, metalen eta erdieroale

organikoen arteko interfaseeen hesi energetikoak (ingelesez energy barrier) dira besteak beste garrantzitsuenetarikoak. Alde batetik, garraioko EG elkarren arteko loturarik gabeko elektroi-hutsune parea sortzeko muga energetiko da. Hau da, harturiko orbital molekular altuena (highest occupied molecular orbital ingelesez, HOMO) guztiz betea baldin badago, elektroiak ezingo dira materialean zehar mugitu. Elektroi batzuk HOMO-tik okupatu gabeko orbital molekular baxuenera (lowest unoccupied molecular orbital ingelesez, LUMO) transferitzen baldin badira ordea, korronte fluxua egon daiteke. Beraz, garraioko E_G konduktibitate elektrikoa eta molekula organikoaren izaera elektrikoa (eroalea, erdieroalea, isolatzailea) determinatzen duen paramtero nagusia da. Bestalde, metalen Fermi energiaren eta karga garraiatzen duten orbital molekularren arteko hesi energetikoek, metaletik erdieroale molekularrera injektatzen den karga elektrikoa mugatzen du. Ondorioz, hesi energetiko hauek berebiziko garrantzia eta eragina dute gailuen errendimenduan. Esaterako, argia igortzen duten diodo organikoen (organic light emitting diode ingelesez, OLED) eragiketa tentsioa, eremu elektrikoan oinarritutako trantsistore organikoen (ingelesez organic field effect transistors, OFET) atalase tentsioa eta zelula fotovoltaiko organikoen (organic photovoltaic devices ingelesez, OPV) zirkuitu tentsio irekia zehazten dute. Beraz, parametro hauen karakterizazio zehatzak errendimendu hobeko gailuen diseinuan ahalbidetzen du.

Berebiziko garrantzi izan arren, askotan parametro hauek ez dira ondo karakterizatu eta bereizten. Garraioko EG-aren kasuan, teknika fidagarri eta zuzenen gabeziak, era okerrean, molekulen oinarrizko, teoria, optiko edo interfaseko E_G-etara jotzea dakar. Hesi energetikoei dagokienez, elektroien fotoemisio espektroskopia (ingelesez electron photoemission spectroscopy), Kelvin zunda eta orain dela gutxitik gailu elektroniko bidezko espektrokopia molekularra (ingelesez in-device molecular spectroscopy, i-MOS) erabili izan dira neurketa teknika bezala. Lehen bi esperimentuetan substratu metalikoetan jarritako geruza molekular meheen lan funtzioaren aldaketak jarraituz energia mailen lerrokatzea ebazten da. Teknika hauetarako ekipamendu konplexua beharrezkoa da eta beraz, zaila da gailu elektronikoen geometrian inplementatea. Hirugarren metodoak gailuen funtzionamendu baldintzetan eta aurretik meterialen

inungo informaziorik izan gabe, metal eta erdieroale organikoen arteko hesi energetikoak kuantifikatzen ditu.

Gailu elektroniko bidezko espektrokopia molekularra (i-MOS) edo gailu bidezko elektroi energetikoen espektroskopia (ingelesez in-device hot-elecron spectroscopy) elektroi balistikoen emisio espektroskopian (ingelesez ballistic electron emission spectroscopy, BEEM) oinarritutako egoera solidoko esketroskopia metodo iraultzailea da. i-MOS-en kasuan tunel efektuzko miskroskopioaren (ingelesez scanning tunnelling microscope, STM) punta azalera handiko tunel junturagatik ordezkatzen da. Aldaketa honek metalen eta erdieroale molekularren arteko hesi energetikoak gailu elektronikoen funtzionamendu baldintzetan eta aurretiaz materialaren inguruko informaziorik ezagutu gabe neurtzea ahalbidetzen du. Horretaz gain, metalaren eta erdieroalearen interfasera iristen diren elektroiak balistikoak direnez, hau da, hesi energetikoaren gainetik injektatzen direnez, kontaktu-erresitentziak ez du eraginik neurketetan.

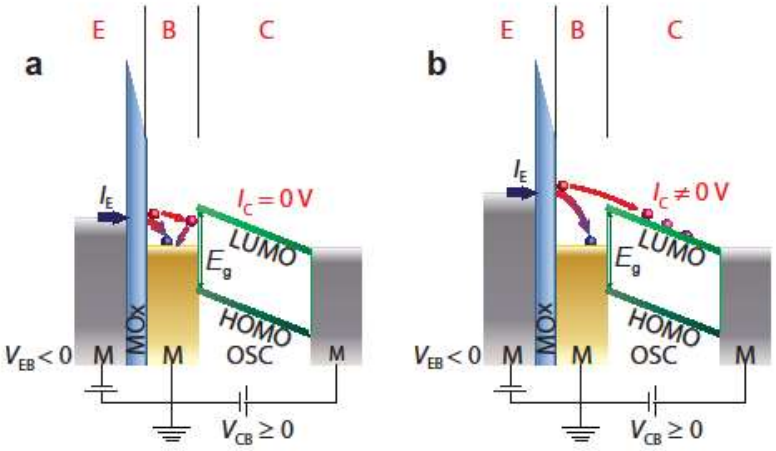

Irudia 1|Gailu elektroniko bidezko espektrokopia molekularraren (i-MOS) lan printzipioa. Tunel efektuan oinarrituta elektroiak igorletik, E, basera, B, igaro daitezke bi borne hauen artean V_{EB} tentsioa aplikatuz. **a**, V_{EB} metalaren eta erdieroalearen interfaseko energia hesia, Δ, baino baxuagoa bada, kargak ezingo dira orbital molekularrera sartu. Ostera, interfase horretan isladatu eta basera eroriko dira. **b**, Ezarritako V_{EB} Δ baino handiagoa bada, elektroi energetikoen frakzio bat erdieroalearen orbital molekularrean sartu eta goi kontaktu metalikoratza hedatuko dira. I_C korrontea neurtuko da. Elektroien korrontea basearen eta kolektorearen artean tentsiorik aplikatu barik edo tentsio positiboa aplikatuz detektatu daiteke.

i-MOS hiru terminalez osaturiko gailu bertikala da (ikusi Irudia 1). Borne hauek igorlea “E” (ingelesez emitter), basea “B” eta kolektorea “C” (ingelesez collector) dira. Igorlea metalezko geruza mehea da, zeina hutsetik atera gabe oxigeno plasmarekin oxidatzen den MOx-zko tunnel hesia sortzeko. Basea ere metalezko geruza fina da eta kolektorea berriz, erdieroale molekularra. Azken honen gainean, erdieroalea zeharkatzen duten kargak jasotzeko helburuarekin metalezko geruza mehea hazten da goi elektrodo bezala. Idealki, goiko metal honen Fermi mailak karga garraiatzean duen maila molekularrarekin kontaktu ohmikoa egitea desio da. Adibidez, n-motako erdieroaleen kasuan goiko metalaren Fermi mailak erdieroalearen LUMO mailarekin kontaktu ohmikoa egin beharko luke baina p-motako erdieroalearen kasuan berriz, HOMO mailarekin. Baseko eta goi elektrodoko metalen Fermi energien arteko desberdintasunak potentzial erantsia sortuko du erdieroalean zehar. Horrela bada, kanpotik gehitutako tentsio beharrik gabe kargak erdieroale molekularrean zehar mugitu daitezke. Bestalde, igorlearen eta basearen Fermi energien arteko lerrokadura terminal bi hau artean aplikatutako tentsio, V_{EB}, bidez kontrolatzen da. Basearen eta kolektorearen energia lerrokadura metalaren eta erdierloa organikoaren arteko hesi energetikotik dator.

V_{EB} tentsio negatiboa aplikatzean, elektroiek MOx barrera tunnel efektu bidez zeharkatuko dute, eta horrela I_E elektroi korrontea igorletik gailura injektatuko da. Elektroi hauen energia metalen Fermi energia baino altuago da eta karga hauen frakzio txiki batek basea balistikoki eta energia galerarik gabe igaroko du. Aplikatutako V_{EB} kanpo tentsioa hesi energetikoa baino baxuagoa bada, $\Delta > eV_{EB}$, (Irudia 1a) elektroi balistikoen korrotea metal eta erdieroalearen arteko interfasean isladatu eta basera jariatuko da, I_B. Beraz, ez da korronterik detektatuko kolektorean ($I_C = 0$). Bestalde, V_{EB} interfaseko hesi energetikoa baino handiagoa bada, $\Delta < eV_{EB}$, (Irudia 1b) elektroi hauen parte bat LUMO mailara sartu, goiko elektrodorantz mugitu eta kolektoreko korronte, I_C, bezala detektatuko da ($I_C \neq 0$). Injekzio energia, eV_{EB}, gehiago aplikatuz, kargak oinarrizko maila molekularraz gain LUMO+1 bezalako maila kitzikatuetara heldu ahalko dira. Basearen eta kolektorearen artean kanpo tentsio bat aplikatuz, V_{CB}, erdieroalean zeharreko potentsial erantsia handitu eta horrela, erdieroale molekularraren zeharreko karga garraioa erraztu daiteke. Hala ere, energia lerrokaduraren aurkako V_{CB} aplikatuz, potentsial erantsia neutralizatzea eta beraz, karga garraioa blokeatzea ere

posible da. Tesi honetako lehenengo eta bigarren kapituluetan teknikaren eta gailuen fabrikazioaren inguruko infomazio zabalagoa aurkitu daiteke.

Doktoretza-tesi honetan i-MOS-en oinarrituz teknika hobetu eta posibilitate eta aplikazio berriak ikertu ditugu. Orain arte i-MOS elektroi energetikoen injekzioan oinarrituz metalen Fermi energiaren eta UHV-n lurrudutako molekula txikien LUMO-aren arteko hesi energetikoaren zehazpenera mugatuta zegoen. Tesi honetan muga hori gainditu eta metal eta erdieroale molekularren interfasean gertatzen diren karga garrioko efektuak aztertu ditugu. Hau da:

Hirugarren kapituluan, i-MOSen oinarritu gara metal eta elektroiak garraiatzen dituen polimeroen interfaseko hesi energetikoa neurtzeko. Kontzeptu frogarako urrea eta poly{[N,N′-bis(2-octyldodecyl)-naphthalene-1,4,5,8-bis(dicarboximide)-2,6-dyl]-alt-5,5′-(2,2′ dithiophene)} [P(NDI2OD-T2), PolyeraActivInk N2200] polimeroa erabili ditugu. Urrea metal noblea da eta ez da errez oxidatzen, ondorioz gailu elektronikoen kontaktu bezala erabiltzeko material egokia da. N2200 polimeroa ez da airearekin kontaktuan degradatzen, elektroi mobilitate handia dauka eta guzti honek aplikazio teknologikoetarako materia interesgarria izatea dakar. Polimeroa kloroformotan disolbatu eta baseko urrezko kontaktuaren gainean zentrifugazio estaldura bidez ezarri dugu UHV-tik kanpo. Lortutako emaitzak fotoemisio ultramorezko espektroskopiaz neurtutako emaitzekin alderatu ditugu. Azken teknika hau n-motako polimerodun sistemetarako artezkoa izan ez arren, gehien erabiltzen den metodo experimentala da. Horrela bada, i-MOS metodo fidagarria eta zuzena dela frogatu dugu. Horretaz gain, lagina UHV-tik kanpora ateratzean baseko urrearen gainean sortzen den kutsadura geruzak kargen transporteari dagokion interfazeko hesi energetikoan ez duela inungo eraginik ebatzi dugu. Simulazio teorikoek emaitza hauek baieztatu dituzte. Ikeketa honek beraz, i-MOS teknika elektronika molekularraren industriara hurbiltzeaz gain, polimeroetan oinarritutako gailuen diseinurako tresna egokia dela frogatzen du.

Laugarren kapituluan i-MOS teknikaren funtsionalitatea hedatu eta erdieroale molekularraren garraiko E_G gailuaren funtsionamendu baldintzetan eta materialaren informazio beharrik gabe neurtzea ahalbidetzen duen teknika bezala garatu dugu. Horretarako, LUMO mailaren energia neurtzeaz gain HOMO ere neurtzen dugu. Maila hauek elektroein zein hutsuneen injekzio-detekzio zuzenaz zein scattering inelastikoa edo

Auger scatteringa bezalako bigarren mailako dispertsio talkak jasan ostean neur daitezke. Horretaz gain, erdieroale molekularrera kargak balistikoki bidaltzeak, lehen aldiz era zuzenean eta egoera solidoan Markusen inbertsio erregimena behatze ahalbidetu digu. Hiru terminaleko transistore honetan efektua erresitentzia diferentzial negatibo bezala ageri da. Zuzenean behatzeaz gain, erregimen hau tenperaturarekin, eremu elektrikoarekin eta argiarekin manipulatu daiteke. Behaketak C_{60} eta C_{70} erdieroale molekularretan oinarritu dira eta baseko metalaren independente dira.

Bostgarren atalean, i-MOS flexibleak fabrikatu ditugu Kaptonezko zintak sustratutzat erabiliz. Lagin hauek hainbat toleste angelutan funtzionatzen dutela frogatu dugu. Horrela, gailuak tolestean tentsio mekanikoa aplikatzen da laginean zehar eta honek metalen eta erdieroale molekularren interfaseko hesi energetikoan duen eragina aztertu dugu. Tolestu gabe eta toleste angelu desberdinetan ez dugu hesi energetikoen aldaketarik ikusi, eta beraz, garraioko hesi energetikoak ez duela tentsio mekanikoaren dependentsiarik ebatzi dugu. Esperimentuak urrea baseko metal bezala eta C_{60} molekula biribila eta PTCDI-C8 molekula laua erdieroale bezala erabili ditugu. Tolestean I_C korrontearen anplitudea C_{60}-ren kasuan ia ez dela aldatzen eta PTCDI-C8ren kasuan handitu egiten dela ikusi dugu. Molekulen arteko desberdintasunak geometria diferentzietan datza eta I_C korrontearen hazkuntza tentsiaorekin molekuletan zehar gertatzen den kargen transferentzia tasa kontrolatu dezakegulako dela ondorioztatu dugu.

Lan honek alde betetik i-MOS erdieroale organikoen maila molekularren energia eta garraiko E_G determinatzeko teknika espektroskopiko zurruna dela erakusten du. Horrela bada elektronika organikoaren komunitateari gailuen diseinurako tresna zuzen eta eskuragarria aurkezten diogu. Bestalde, kargen injekzio balistikoak Marcusen inbertsio erregimenetik erresistentzia diferentzial negatiboa ikustea ahalbidetzeak hiru terminaleko gailu hauen interesa handitzen du. Izan ere, efektu honetan oinarrituz anplifikadore organikoak eta eraginkortasunez galerarik gabeko osziladoreak eraiki daitezke. Azkenik, tolestura tentsioak kargen garraioan molekularen geometriaren arabera efektu nabaria duela ikusi dugu. Tesi honetan aurkeztutako emaitzek elektronika molekularraren oinarrizko ezagutza handitzean eta gailu eraginkorragoen diseinuan eragina dute.

Abstract

The engineering of molecular semiconductor-based (opto-)electronic devices requires a precise knowledge of molecular parameters such as the transport energy gap as well as the energy barriers at metal/semiconductor interfaces. On the one hand, the transport energy gap is the threshold for creating an electron–hole pair that is not bound together. In other words, if the highest occupied molecular orbital (HOMO) is completely full and the lowest unoccupied molecular orbital (LUMO) is completely empty, then electrons cannot move in the material. However, if some electrons transfer from the HOMO to the LUMO, then current might flow. Therefore, the transport gap is a major factor determining the electrical conductivity and the electrical nature (conductor, semiconductor or insulator) of the organic molecules. On the other hand, the interface energy barriers build up between the metal Fermi energy and the charge transporting molecular levels, limit the charge injection from the metallic contact to the molecular semiconductors. Consequently, they have a deep impact on the performances of the devices, determining the operation voltage in organic light emitting diodes, the threshold voltage of field-effect transistors and the open circuit voltages of the photovoltaic devices. Thus, an accurate characterization of these parameters serves for the engineering of improved performance of devices.

Besides the relevance, these parameters are not often well characterized. In the case of the transport gap the lack of reliable and straightforward techniques results in the erroneous adoption of the value of other energy gaps, such as the molecular fundamental, first principles, optical and interface ones. Regarding energy barriers different approaches such as electron photoemission spectroscopy, Kelvin probe and more recently in-device hot electron spectroscopy have been applied. In the first two

experiments the energy level alignment is extracted by monitoring the change in the work function for thin molecular layer evaporated on metallic substrates. They require complex equipment and are far from being implemented into device architecture. On the contrary, the third method enables the determination of energy barriers between metal and semiconductors in device operative conditions and without any prior knowledge of material parameters.

In this thesis we have based on in-device hot-electron spectroscopy to further explore the possibilities that this technique offers for the determination of metal/molecule interface energy alignment and for the first time, the transport gap. This brings us to rename the technique as in-device molecular spectroscopy (i-MOS). The thesis is organized as follows:

In Chapter 1, we motivate our work based on organic electronics and describe the typical metal/molecular interfaces to understand the parameters that are important when we deal with them. We also comment on the most used techniques for the characterization of metal/molecule interface energies and we give a detailed explanation of the basis, performance and mechanisms of i-MOS.

In Chapter 2, the equipment used for the fabrication and characterization of the samples is described. All the samples described in this thesis were produced in an ultra-high vacuum evaporator composed of one organic material chamber and two metal evaporation chambers. The electrical characterization of the devices was performed in four-probe measurement stations. Atomic force microscopy, X-Ray diffractometer and Raman microscopy were used for material characterization.

In Chapter 3, we measure metal/solution processed electron transporting polymer interface energy barriers by i-MOS. We compare the results with the ones obtained by ultraviolet photoemission spectroscopy to demonstrate that i-MOS is a reliable direct method for n-type polymers. We also resolve that the contamination layer coming from air exposure of samples does not play any significant role on the energy barrier alignment for charge transport.

In Chapter 4, we extend the functionality of i-MOS and we present it as a spectroscopy technique that allows measuring the transport energy gap of the molecular semiconductors seamlessly, in real device operative conditions and without any previous knowledge of the material parameters.

Moreover, the ballistic injection of hot carriers into a molecular film permits us directly observing transport phenomena, such as Marcus inversion regime. This is observed as an effective differential resistance state in a three-terminal device. We do not only observe but also manipulate it externally by temperature, electric field and light.

In Chapter 5, flexible i-MOS devices have been fabricated on Kapton tape. These devices have been measured for several bending angles in order to understand the dependence of the metal/molecule interface energy barriers with strain. No change has been observed in the energy barriers. Nevertheless, an increase of the collector current has been observed for planar molecules, which suggest that the hopping rate of the charges in the semiconductor is tuned with the bending.

Finally, in Chapter 6 we summarize the main conclusions of this thesis and comment on some possible experiments that could be the continuation of this thesis.

Contents

Laburpena V
Abstract XI
1. Introduction 1
1.1. Organic electronics 1
1.3.1 Organic semiconductors 2
1.2. Metal/organic semiconductor junctions 3
1.3. Interface energy barrier measurements 7
1.3.1 UPS/IPES 7
1.3.2 Kelvin probe 9
1.3.3 Hot and Ballistic Electrons 11
1.4 In-device molecular spectroscopy (i-MOS) 13
1.5 Modelling 18
1.5.1 Tunnel injection of charge carriers 18
1.5.2 Transport across the metal base 19
1.5.3 Transmission across the metal/organic semiconductor interface 20
1.6 This thesis 20
References 22
2. Experimental Methods 27
2.1 Sample Fabrication: Ultra High Vacuum Evaporation 27
2.1.1 Load-Lock 29
2.1.2 Metal Chamber Theva Evaporator 30
2.1.3 Organic Chamber Theva Evaporator 31

2.1.4 Metal Chamber Mantis Evaporator 32
2.2 Electrical Characterization: Probe Stations 34
2.3 Material Characterization 36
2.3.1 X-Ray Reflectivity 36
2.3.2 X-Ray Diffraction 37
2.3.3 Atomic Force Microscopy 38
2.3.4 Raman Spectroscopy 40
References 42
3. Energy Level Alignment at Metal/Solution-Processed Organic Semiconductor Interfaces 43
3.1 Fabrication of the devices 44
3.2 Electrical characterization 47
3.3 Ultraviolet photoemission spectroscopy measurements 49
3.4 Effect of the contamination layer on i-MOS 53
3.5 Modelling 53
3.6 Conclusions 55
References 56
4. Multilevel molecular spectroscopy and Marcus Inverted Region 59
4.1 Device fabrication 60
4.2 Device characterization 62
4.2.1 C_{60} based i-MOS 63
4.2.2 C_{70} based i-MOS 78
4.3 Marcus Inversion Region 88
4.3.1 C_{60} based device 88
4.3.2 Control experiments 98
4.4 Conclusions 104
References 106
5. Flexible in-device molecular spectroscopy 111
5.1 Device fabrication 112
5.2 Sample characterization 113
5.2.1 Topographical measurements 114
5.2.2 Tunnel Junction 116

5.2.3 Base-collector diode 118
5.2.4 Three-terminal measurements 119
5.3 Simulations 122
5.4 Conclusions 123
References 124
6. Final Conclusions & Outlook 127
Appendix A 131
List of acronyms 137
Acknowledgements 139
List of publications 143

Chapter 1

Introduction

1.1. Organic electronics

In 1987 Ching W. Tang and Steven van Slyke produced the first organic semiconductor based diode at Eastman Kodak [1,2]. That device was the very first of a new era within the field of electronics known as organic or molecular electronics. Organic electronics is defined as a field of physics and material science concerning the design, synthesis, characterization and application of small molecules or polymers that show desirable electronic properties such as conductivity.

The great effort put on this research area relies in the benefits compared to inorganic electronics. From a technological point of view, organic compounds seem to be the way to inexpensive electronics since they can be easily processed on a wide variety of low-cost substrates such as plastic, glass or metal coils [3]. Furthermore, some organic materials do not require ultra-high vacuum (UHV) conditions to be treated since impurities do not necessarily form electrically active substitutional defects [4]. Therefore, these materials can be ex-situ handled, reducing the production costs. Indeed, the printing techniques used in graphic arts and industry might be adapted to the production of large area/scale organic electronics [5]. Besides that, the functionality of organic materials can be tuned at the molecular level, where small modifications of fundamental units enable changing both their electronic and optical properties. This opens up the possibility of designing

materials on demand in order to fit into specific applications and satisfy any emerging technological demands [6,7].

1.3.1 Organic semiconductors

Organic semiconductors have emerged as a revolutionary field for both the basic research and the electronic devices industry thus, expanding and opening up novel fields. On the basic research side, organic semiconductors are fascinating systems with a wide range of transport and geometric properties. Regarding applied research, organic semiconductors make possible fully flexible devices for large area displays, solid-state lightning, more efficient and irradiation-angle independent solar cells and frequency identification tags [8–11].

Organic semiconductors can split into two main categories: polymers or small molecules. From a chemical point of view there are big differences between these two kinds of materials and this is also reflected in their technological aspects. Polymeric macromolecules are constituted by the repetition of fundamental units, monomers, and are typically soluble in organic solvents. Thus, they can be treated in liquid state and be spin-coated on a chip. The materials belonging to the second category are commonly named molecular materials, as they are composed of small molecules. Even if they are some soluble small molecules, they mostly must be thermally evaporated [12].

In general terms, organic semiconductors are comprised of amorphous structures of molecules, which are tied together by weak van der Waals forces. The result of these forces is a weak electronic coupling, which makes charge carrier states localized. These carriers may hop from one state to the next whenever the site of origin is occupied by a charge carrier and the target site can accept an additional one [13–15]. Thus, the electronic transport mechanism of organic semiconductors is understood by a sequential carrier transfer that goes on, in the case of electron transport, from an anion radical of a molecule to a neutral one though the lowest unoccupied molecular orbital (LUMO). This molecular orbital is the analogous of the conduction band in inorganic semiconductors. In the case of hole transport, the process happens as a sequential transfer of electrons from a neutral molecule to its cation radical through the highest occupied molecular orbital (HOMO) [16],

which is the organic analogous of the valence band. Molecular packing, disorder, temperature or pressure, among other factors, influences the rate in which hopping process happens. As in the case of inorganic semiconductors, organic semiconductors have an energy gap between the HOMO and LUMO levels (see Figure 1.1). This energy defines the electronic nature as well as the optical properties of the semiconductor.

Depending on the type of charge carrier that give rise to the electrical transport, organic semiconductors are labelled as n-type (electron transporting), p-type (hole transporting) or ambipolar (both, electron and hole transporting with the same or similar ease) [17]. This is usually determined by the energy of the molecular orbitals so, contrary to inorganic semiconductors, organic semiconductors do not need to be doped to achieve these properties that are intrinsic on them. Nevertheless, the deposition and work function of metal electrodes respect to the molecular orbitals can dramatically influence the charge injection to the organic semiconductor.

1.2. Metal/organic semiconductor junctions

The energetics of metal/molecule interfaces has been subject of intensive research over the last twenty years. When a metal and an organic semiconductor come into contact a dipole layer may be formed right at the interface, due to charge transfer across the interface, redistribution of electron cloud, interfacial chemical reactions, and other types of rearrangement of the electronic charge [18]. These dipoles rearrange the energy level alignment at metal/molecule interfaces, reducing or increasing the energy difference between the metal Fermi Energy and the molecular levels devoted to charge transport. These energy barriers limit the charge injection from metals to the molecular semiconductor, which in turn has a deep impact on the performance of the devices, such as determining the operation voltage in organic light emitting diodes (OLED) [19–21], the threshold voltage of organic field effect transistors (OFET) [22,23] and the open circuit voltages in organic photovoltaic cells (OPV) [24–26]. Therefore, an accurate knowledge of the energetics is necessary for the engineering of metal/organic interfaces and the consequent optimization of the performance of the devices. The fabrication of good metal/organic

interfaces is also not trivial [27]. The energy gaps between LUMO and HOMO are relatively big compared to inorganic semiconductors, which turns into an extra difficulty in the fabrication of ohmic contacts for electron and hole injection. Besides, the fragility and reactivity of the organic materials cause diffusion and damages at the metal/organic interfaces.

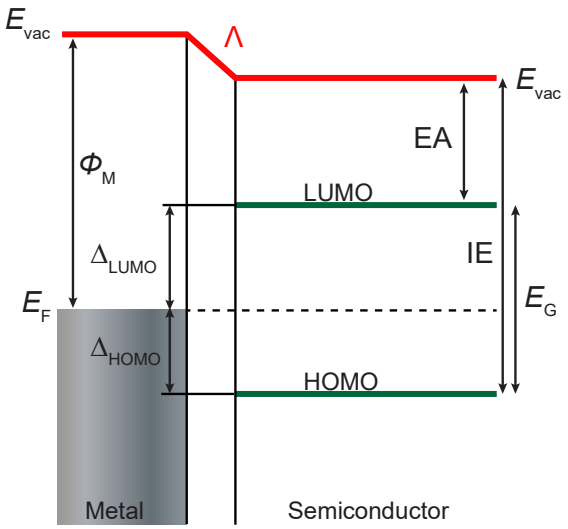

Figure 1.1| Schematic representation of a metal/organic semiconductor interface. Electronic structure of a metal/organic semiconductor interface. HOMO and LUMO corresponds to the highest occupied molecular orbital and the lowest unoccupied molecular orbital, respectively. E_F is the Fermi energy, E_{vac} the vacuum level, $\boldsymbol{\phi_M}$ the work function, IE the ionization energy and EA the electro affinity. Λ is the interface dipole. E_G is the energy gap of the semiconductor. Δ_{LUMO} and Δ_{HOMO} are the energy of LUMO and HOMO with respect to E_F of the metal.

When referring to metal/organic interfaces there are several parameters that one should consider. The main ones are indicated in Figure 1.1, where an interface electronic structure of a typical metal/organic semiconductor interface is shown. E_F corresponds to the Fermi level of the materials. HOMO and LUMO are the highest occupied molecular orbital (hole transporting level) and the lowest unoccupied molecular orbital (electron transporting level), respectively. The vacuum level of each material is indicated as E_{vac}. The work function of the metallic electrode (ϕ_M) is defined as the energy

difference between vacuum and Fermi level. In the case of the organic semiconductor, the ionization energy (IE) and the electron affinity (EA) are the energy difference between vacuum level and HOMO and LUMO, respectively. Δ_{HOMO} represents the interface energy barrier between the E_F of the metallic contact and the HOMO of the semiconductor, while Δ_{LUMO} is the energy barrier between E_F and LUMO. These two parameters together with the energy gap or energy difference between HOMO and LUMO, are essential for understanding electrical and optical performance. However, their determination is not straightforward. At metal-organic interfaces, the wave functions of the metals and the organic interact with each other giving rise to a new wave function at the interface. Due to this overlap, charge reorganization takes place at the interface and thus, an interface dipole Λ is formed. Therefore, the molecular energy levels are shifted with respect to the Fermi level of the metal. Various approximations and models have emerged in order to try to explain the complexity of these interfaces:

- **The Schottky-Mott model**: Non-interactive metal–semiconductor interfaces are assumed in this model. The energy of the molecular levels with respect to the E_F of the metal electrode is aligned to the vacuum level without considering any interface dipole, Λ =0. Thus, the electron injection barrier is equal to the difference between the electrode work function ϕ_M and the energy of the LUMO level, while the hole injection barrier is the difference in energy of ϕ_M and HOMO [27].
- **Reorganization of surface metal electronic structure: the "pillow effect":** The Coulomb repulsion between the electronic density of a molecule and the surface metal electrons locally suppresses the tail of electron wave function that spills into vacuum reducing the work function of the metal. This effect is generally larger for large work function noble metals such as gold [27].
- **Defect and chemistry-induced gap states:** Chemical bonds and/or defects between an organic semiconductor and a metal can create filled or empty electronic states that overlap with the original energy gap of the semiconductor. This effect typically happens when a metal is evaporated on an organic semiconductor or when the organic material is evaporated on a reactive metal [27].

- **The induced density of interface states (IDIS):** At a metal–semiconductor interface, the metal electron wave function tails into the semiconductor and the penetration depth depends exponentially on the energy gap of the semiconductor. The overlap between metal states and semiconductor states broadens the molecular levels of interface molecules and induces a density of interface states in the gap of the semiconductor, known as induced density of interface states (IDIS). This theory is used to explain weakly interacting molecular interfaces [27].

An important fabrication issue in metal-organic junctions is the interface formation sequence. It has been noticed that metal deposition from a hot source on a soft organic material film induces damage and diffusion into it. On the contrary, if organic materials are vacuum-deposited or spin coated on a cold metal surface abrupt interfaces are expected to be formed. Even if in this last case chemical reactions are also possible [27,28], its spatial extend is expected to be confined to the interface layer. Therefore, depending on the metal/organic pair, current density injection for organic/metal or metal/organic interfaces might change [27,29].

Typically, direct and inverse photoemission spectroscopies (PES and IPES respectively) [27,29], Kelvin probe measurements [30], ballistic-electron emission microscopy (BEEM) [31,32] and in-device molecular spectroscopy (i-MOS) [33–36] have been applied to the study of interfacial energy barriers. The first two methods are limited to extract the energy level alignment by monitoring the work function for thin molecular layers evaporated on the surface of a metal. They required complex equipment and are complex to be implemented into device architecture. The third one can extract the interface energy barrier in a more direct way, but it is a local method based on a scanning tunnelling microscopy, STM, probe and thus, it is also far from device operative conditions. The last one, i-MOS, is a solid-state device version of BEEM and has opened the possibility to determine the energy barriers between a metal and a semiconductor without using any material parameters and in-device operative conditions [33–36]. In the following sections these techniques will be further discussed.

1.3. Interface energy barrier measurements

1.3.1 UPS/IPES

The main experimental techniques used for the characterization of the energy level alignment at metal/organic interfaces are direct and inverse photoemission spectroscopies (PES, IPES) [18,27,37]. These techniques provide information on the energy distribution of occupied and unoccupied states at the surface and interface of films.

PES is based in the application of the photoelectric effect. The sample is exposed to a beam of ultraviolet or X-ray radiation, which induces photoelectric ionization. In other words, when the sample is irradiated, electrons from occupied states absorb the energy of the incoming photons and they are excited according to the absorbed energy. If these electrons get more energy than the needed to arrive to the vacuum level, they will be taken out from the material. The energies of the emitted photoelectrons are characteristic of their original electronic states, while depend also on vibrational state and rotational level. While X-ray photoemission spectroscopy (XPS) is used to study the energy levels of atomic core electrons, ultraviolet photoelectron spectroscopy (UPS) is suitable for investigating valence energy levels and chemical bonding, especially the one of molecular orbitals. This last technique, hence, permits the determination of the energy of the HOMO. The source of photons typically used is HeI ($h\nu = 21.2$ eV) and HeII ($h\nu = 40.8$ eV) radiation [27] Nevertheless, the UPS spectra can also provide information of the work function of the metal as well as the change in the work function by knowing the energy of the radiation source and measuring the secondary-electron (electrons that undergo inelastic scattering) cutoff, E_{cutoff} (see Figure 1.3). The formula for obtaining the work function is the following one:

$$\Phi = h\nu - E_{\text{cutoff}} \tag{1.1}$$

The change in work function can be tracked by remeasuring the E_{cutoff} after a deposition of a molecular film and calculating the difference in work function before and after the molecular deposition. Therefore, the relation between the occupied levels at a heterojunction can be measured, both in reference of the vacuum level and Fermi level [18,27,29].

In IPES, incident electrons with controlled kinetic energy (5-15 eV) penetrate the solid above the vacuum level and decay in an empty state [27]. The energy is released in the form of a photon, which is later captured by the detector. The number of photons collected as a function of electron energy provides the density of unoccupied states in the analysed material. In the case of molecules, it will give information of the LUMO level. The ratio between photon flux per incident electron in IPES and electron flux per incident photon in PES comes as the ratio between photon vector and electron wave vector. Considering that photon and electron energies involved in these experiments are of the order of 10 eV, the ratio is of the order of 10^{-5} (Ref 27). This confirms the difficulty of the IPES experiment, which suffers from low yield and signal-to-noise ratio, and thus requires relatively large incident electron currents, which in turn provokes damages in the organic films.

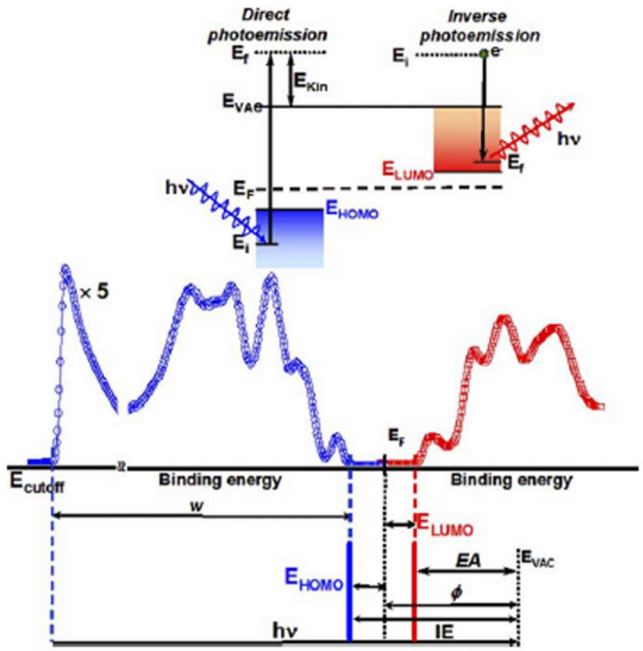

Figure 1.2| Photoemission spectrum. Combined UPS (blue line) and IPES (red line) spectra. UPS (top blue) and IPS (top red) mechanisms are also shown on top of the spectra. Image taken from *Technische Universität Chemnitz website.*

Figure 1.2 shows the composition of UPS and IPES [27]. The left spectrum (blue line) is the UPS spectrum of the occupied states while the right one (red line) is the IPES spectrum of the unoccupied states. A common energy scale was obtained for both spectrums by aligning the Fermi energy measured with both techniques. Both UPS and IPES spectra consist on a series of features corresponding to single or multiple occupied and unoccupied molecular levels, respectively. For most organic materials, the identification of HOMO and LUMO positions is not trivial because parameters such as the polaron energy and the lattice and molecular relaxation energies must be considered [18,27,29].

Figure 1.2 shows the composition of the data extracted by UPS and IPES[27]. The left spectrum (blue line) is the UPS spectrum of the occupied states while the right one (red line) is the IPES spectrum of the unoccupied states. A common energy scale was obtained for both spectrums by aligning the Fermi energy measured with both techniques. Both UPS and IPES spectra consist on a series of features corresponding to single or multiple occupied and unoccupied molecular levels, respectively. For most organic materials, the identification of HOMO and LUMO positions is not trivial because parameters such as the polaron energy and the lattice and molecular relaxation energies must be considered [18,27,29].

Once HOMO-LUMO energies are known, the calculation of the interface energy gap is the difference of the two energy levels. However, in order to translate the interface energy gap to bulk one, electronic polarization effects, such as image charge potential, should be considered [27]. Moreover, one should have in mind that as the molecular orbital levels are not measured in transport conditions, they do not provide information about how they affect to the charge injection from a metallic contact to the molecular orbitals.

1.3.2 Kelvin probe

Kelvin probe is a non-contact and non-destructive vibrating capacitor variant of atomic force microscope (AFM) that enables measuring the work function of conducting materials or surface potential of semiconductor and insulating surfaces (Figure 1.3). This technique is a surface method, which monitors typically one to three layers-atoms-thick surfaces [38–40].

The work function is the energy needed to release electrons from the surface of a material. When two materials with different work functions are brought together, electrons flow from the one with the lower work function to the one with the higher work function. In this geometry, the tip and the surface form a parallel plate capacitor. The voltage developed over this capacitor is called contact potential and it is measured by applying an external backing potential to the capacitor until the surface charges disappear and thus, the two potentials are equalized. The work function difference between two surfaces can be found by measuring the charge flow when the two conducting materials are connected [38–40]. Nevertheless, it has been probed that the measurements strongly depend on the cantilever and thus, results can vary from cantilever to cantilever.

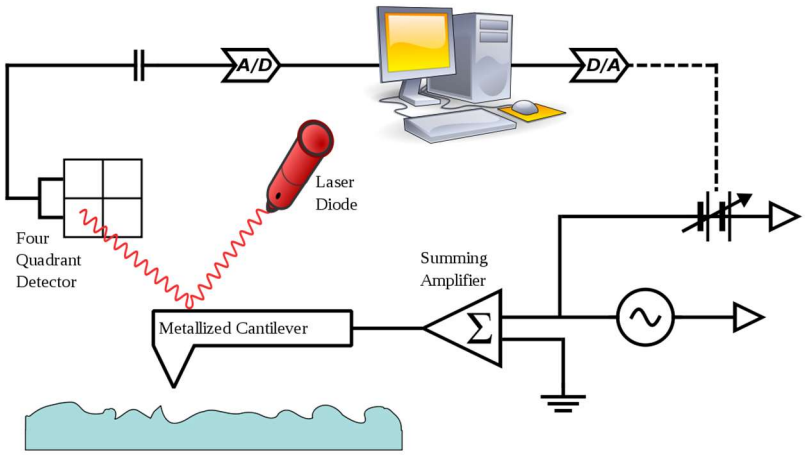

Figure 1.3| Setup of a Kelvin probe. In Kelvin probe microscopy, a conducting cantilever is scanned over a surface at a constant height while an AC+DC potential is applied. The frequency of AC signal matches the mechanical resonance of the cantilever. The oscillations of electrostatic forces between the surface and the cantilever drive the last one into oscillation. Using a four-quadrant detector and an AC to DC convertor to detect cantilever motion, the feedback circuit drives the DC signal to the surface potential. This minimizes the cantilever motion and results in a map of the work function of the sample surface. *Image taken from Wikipedia.*

In such experiments the energy level alignment is extracted by monitoring the change in the work function when thin molecular layers are evaporated on the surface of a metal. Therefore, it is not possible to monitor directly

how the measured energy level alignment limits the charge the electrical charge injection from the metallic contact to the organic semiconductor. Moreover, the use of cantilevers permits only obtaining local information of the energy level alignment and thus, this spectroscopy technique is far from device applications.

1.3.3 Hot and Ballistic Electrons

Hot charges, electrons or holes with energies higher than a few tenths of one electron volt (eV) above or below respectively the E_F of a material, have become important for the understanding of modern devices [41]. Charges contributing to the electrical conductivity in solids are free holes or electrons with few $k_B T (\approx 25\ meV$ at 300 K) above or below the Fermi level. Making an analogy of the electron energy to the crystal lattice temperature and considering $eV = k_B T$, electrons with 1 eV above E_F correspond to a temperature rise up to ≈ 1200 K [42]. Nevertheless, those energies are not accessible just by increasing the temperature of the material and thus, the kinetic energy of the hot charges must be considered.

Hot electrons can occupy free states above $E_{F,}$ while in contrast these levels are filled for thermal electrons. Therefore, the scattering mechanisms for hot-electrons and electrons at Fermi level are very different. The probability for hot-electrons finding empty states to scatter into is described by Fermi´s golden rule [43]. Fermi-Dirac distribution describes the filling of the bands for the electrons at the Fermi level.

Elastic or quasi-elastic (electron-phonon) scattering are the dominant scattering mechanisms at the Fermi level while inelastic electron-electron (e-e) scattering is more dominant at the higher energies. Inelastic scattering of hot electrons is caused by the Coulomb interaction with other electrons below E_F. Hot electrons lose a large part of their energy via this scattering event. Defects and impurity scattering are always present in any metal and cause a temperature and energy independent elastic scattering contribution [44]. However, if during the propagation through the metal no scattering event happens, these electrons will have a ballistic transport. Ideally, ballistic hot electrons do not have any energy lose and any change in the linear momentum [41,42].

In 1988 W. J. Kaiser and L.D. Bell [31,32] reported a novel spectroscopic technique based on scanning tunnelling microscopy (STM) and hot charges. The method, ballistic electron emission microscopy (BEEM), enables the study of metal/semiconductor interfaces by injecting ballistic charges from STM tip. In the following subsection we will discuss it in more details.

1.3.3.1 Ballistic Electron Emission Microscopy

BEEM is a modified form of scanning tunnelling microscope (STM) that allows the study of non-equilibrium carrier transport across buried interfaces. A BEEM setup has an additional back contact to the sample, three terminals in total, that makes possible the collection of the injected charges after having travelled through the entire device.

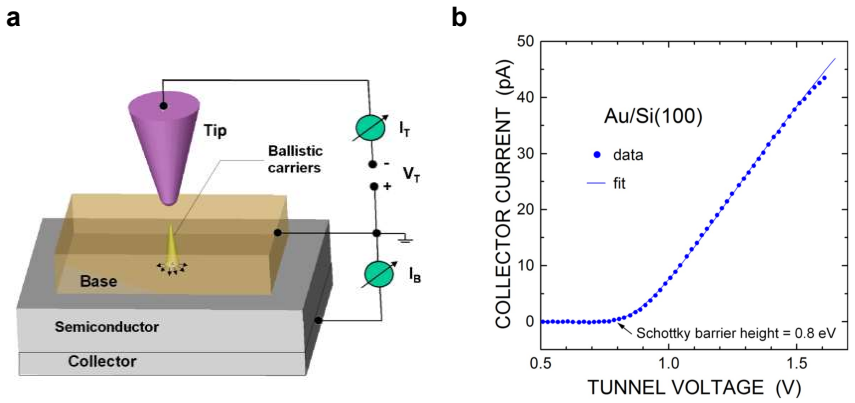

Figure 1.4| Ballistic emission microscopy (BEEM). a, Schematic setup of BEEM. A constant tunnelling current I_T is injected at variable tunnelling voltage V_T. The electrons that surpass the bulk semiconductor are detected as BEEM current I_B. (Figure taken from Ref. 46). **b,** Typical BEEM spectrum with collector current versus the tunnelling voltage. The onset of the current corresponds to the barrier height between the metal and the semiconductor. (Figure taken from Ref. 47).

BEEM can be used as a spectroscopic technique or as an imaging technique [45]. The most widely used mode is the spectroscopy one which provides information on local transport characteristics of hot electron between the STM tip and the semiconductor. As shown in Figure 1.4a the current is injected perpendicularly to the layer stack plane from a tip and by

tunnelling into unoccupied states of the thin metal base. Once injected, the hot charge carriers propagate through the metal film. When the carriers reach the interface and the energy of the charges is higher or the same as the energy barrier at metal semiconductor interface, $eV_T < \Delta$, and their transversal component of the linear momentum is conserved, they enter unto the semiconductor [31,32]. The BEEM current is only detected when the applied tip bias is high enough to overcome the onset corresponding to the Schottky barrier height between the Fermi level of a metallic contact and the molecular level of the organic semiconductor devoted to charge transport (see Figure 1.4b). The higher tip bias is, more electrons will contribute to the BEEM current. Finally, after being transported through the semiconductor, electrons are collected and form the BEEM current. Therefore, a BEEM spectra is obtained by recording the BEEM current with respect to the tip bias at fixed position. The BEEM spectrum provides the information about energy dependence of hot electron transport in the metal film as well as metal/semiconductor interface.

The BEEM imaging mode enables the acquisition of a direct spatial map of the BEEM transmission. Using the STM tip to scan the conducting surface, BEEM image can be mapped by simultaneously recording BEEM current at a fix tip bias above the threshold value. A comparison between the BEEM image and a surface image provides information about the transport characteristics with respect to the structural ones of the metal film and the metal/semiconductor interface [48].

1.4 In-device molecular spectroscopy (i-MOS)

In-device molecular spectroscopy (i-MOS) or in-device hot electron spectroscopy is a solid-state spectroscopy method based on ballistic emission spectroscopy [31,32,49]. However, in the case of i-MOS the STM tip used in BEEM is replaced by a large area tunnel junction, which enables the measurement of metal/organic semiconductor energy barrier in device operative conditions and without any prior material parameters. Moreover, as the electrons arriving to the metal/semiconductor interface are ballistic and thus, they are injected above the energy barrier, the measurements are not affected by the contact resistance.

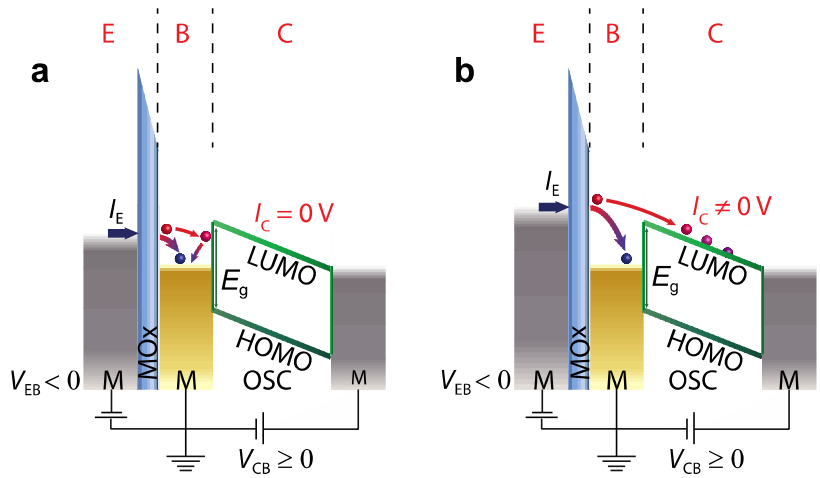

Figure 1.5| Energy level alignment and working principle of in-device molecular spectroscopy (i-MOS). Electrons can tunnel from the emitter to the base when a bias between the emitter and the base V_{EB}, is applied. **a**, if V_{EB} is lower than the metal/organic semiconductor interface barrier, Δ, ballistic electrons cannot enter into the molecular orbitals devoted to charge transport, in this case the lowest unoccupied molecular orbital LUMO, and they will be reflected back to the base. No collector current I_C will be measured. **b**, if the applied V_{EB} is higher than Δ, a fraction of the hot electrons flow into the LUMO of the organic semiconductor and they will diffuse to the top metallic contact. Non-zero I_C will be measured. Electron detection can be done with zero base collector bias V_{BC} or with positive V_{BC} in order to enhance the organic in-built potential.

i-MOS is a three terminal vertical device with emitter "E", base "B" and collector "C" (see Figure 1.5). The emitter is a metal thin film, which latter can be plasma-oxidized to create a metal-oxide thin film tunnel barrier. Another metal thin film composes the base while the collector is an organic semiconductor. A metal thin film is used as top electrode to receive the collector current from the semiconductor. This top electrode is desired to have an ohmic contact with the molecular level devoted to charge transport of the molecule, i.e. in the case of having n-type semiconductor we will look for ohmic contact between E_F of the top metal and the LUMO of the semiconductor, while in the case of p-type materials the alignment should be with the HOMO level. The energy difference between the base and top

metallic contacts form a built-in potential in the organic semiconductor. This enables charge transport through the organic semiconductor without any external bias. In these devices, the energy level alignment between the Fermi level of the emitter and the base is externally controlled with a bias between these two electrodes, V_{EB}, while the energy alignment at the base/collector interface is naturally given by the metal/organic semiconductor barrier Δ**.**

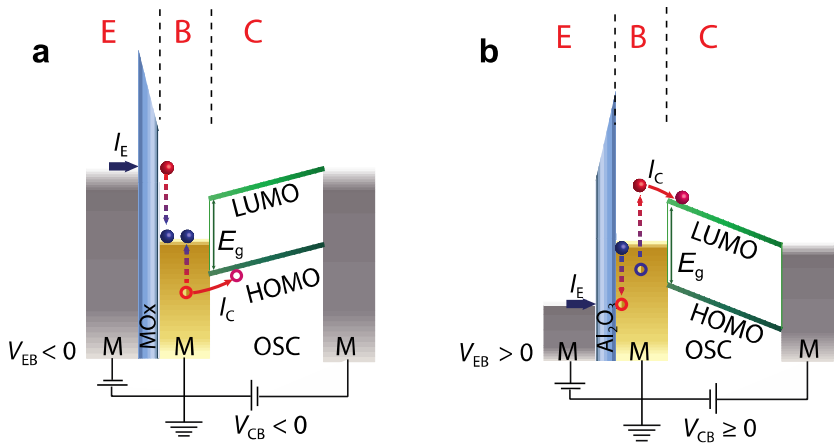

Figure 1.6| Direct and secondary hole injection into n-type semiconductor by in-device molecular spectroscopy (i-MOS). **a,** A negative bias is applied in order to inject electrons from the emitter to the base. However, the negative V_{BC} applied stops hot electron injection into the lowest unoccupied molecular orbital LUMO of the n-type semiconductor. Instead, holes which are created by the inelastic scattering of the incident hot electrons in the metal base with cold electrons (below Fermi level) are injected into the HOMO level of the semiconductor. **b**, Positive bias is applied in to inject holes from emitter to base. However, the negative V_{CB} applied avoids hot hole injection into HOMO of the semiconductor. Instead, incident holes inject excite secondary electron-hole pairs in the metal base and hot electrons are created. With sufficient energy they might be able to access LUMO level of the semiconductor.

When a negative V_{EB} is applied, electrons tunnel through the thin metal-oxide barrier and thus, an electron current I_E is injected from the emitter into the device. These electrons are “hot” in the base because they energy is

above the Fermi energy of the metal, and a fraction of them cross the base ballistically without energy attenuation [41]. If the applied external bias V_{EB} is lower than the energy barrier Δ (see Figure 1.5a), the ballistic electron current is reflected at the metal/semiconductor interface and no collector current ($I_C = 0$) is measured since it will flow instead into the base terminal I_B. On the contrary, if V_{EB} is higher than the barrier $\boldsymbol{\Delta}$ (see Figure 1.5b), some of the electrons enter into the LUMO level, diffuse towards the top metal electrode and non-zero current is measured in the collector ($I_C \neq 0$). If more energy, eV_{EB}, is applied, charges will not only be able to access ground molecular levels but also exited molecular orbital levels, such us LUMO+1. Externally applying a bias between the base and the collector, V_{BC}, one can externally enhance the built-in potential, which in turn facilitates charge transport through the organic semiconductor. Nevertheless, the built-in potential can also be neutralized and thus block charge transport by applying a V_{CB} opposite to the energy alignment.

In standard i-MOS experiments, a n-type bulk semiconductor is used as a collector while negative V_{EB} is applied to inject electrons from emitter to base. A fraction of injected hot electrons can then be collected as I_C, as it has been explained above. However, if a positive V_{EB} is applied, instead of electrons tunnelling from emitter to base, holes will be injected into the device, enabling the determination of the interface energy barrier between E_F and HOMO. This is an analogous mechanism to the electron injection.

However, one should bear in mind that electrons or holes are not the only carriers present in each of the mechanisms described above. In other words, together with these primary electrons/holes, secondary holes/electrons are created in the metal base, respectively. Inelastic scattering of incident hot electrons in the gold metal base with cold electrons (below the Fermi level) originates through the semiconductor, holes with sufficient energy to overcome the metal/semiconductor energy level might be able to access the HOMO level and flow towards the top electrode. Secondary electrons are the consequence of a scattering process known as Auger-like scattering, where incident holes excite secondary electron-hole pairs in the base metal (Figure 1.6b). If the electric field in the organic semiconductor is favourable, they might be injected into the material enabling the determination of the relative energy of LUMO level [50,51].

One of the main advantages of i-MOS is that it does not require complicate fittings of *I-V* curves for the determination of the relative molecular orbitals. Following Kaiser and Bell theory for inorganic semiconductors, Gobbi *et al.* [34] demonstrated that a linear interpolation of the growth of the current to the $I = 0$ is enough for this purpose. In other words, the collector current behaves as $I_C \propto (e|V_{EB}| - \Delta)$. This approach is only valid for direct charge injection and in the case of secondary processes, an extra power two coming from the anisotropic distribution of these at metal base should be included leading to $I_C \propto (e|V_{EB}| - \Delta)^3$ [49–53]. However, as it will be further discussed in chapter 4, this strategy is valid for low disorder organic semiconductors such as C_{60}, but in the case of higher disorder molecules, i.e. C_{70}, the onset of the I_C might be delocalized and thus, this approach might be non-accurate. Moreover, and even if the organic semiconductor has a low disorder, the determination of the energy of excited molecular levels, such as LUMO+1, might be difficult by linear extrapolation. Excited states have typically lower energy separation among them and the tale of the density of states, DOS, of a molecular level might be mixed with the DOS of the other. An alternative approach for determining the relative energy of the molecular orbital levels is to look at the onset of the derivative of the collector current, dI_C/dV. If the current values are very low or the measurements are noisy the derivative might not be possible and thus, one has to carefully evaluate in which situation the linear fitting or the approach of the derivative should be followed.

Playing with the bias enables the determination of the relative energy of the HOMO and the LUMO levels of the organic semiconductor. Hence, knowing the position in energy of these two levels and just by calculating their energy difference, the transport energy gap can be extracted. We emphasize the fact that it is transport energy gap because the HOMO and LUMO energies are determined in device operative conditions and so the energy gap. This is an extremely important application of i-MOS as it is the only method that enables the direct determination of transport energy gap of an organic semiconductor. This functionality of i-MOS will be further discussed in chapter 4.

1.5 Modelling

In order to better understand the performance of i-MOS and the charge transport through the device a theoretical model is developed. The fist theoretical description dealing with the transport of hot-charge carriers through a metal semiconductor system in a BEEM setup was proposed by Bell and Kaiser [31,52]. As it was explained in previous sections, i-MOS is the solid-state variant of BEEM, and thus great part of its theory is based on BEEM theory. Nevertheless, a more specific and detailed theory for i-MOS has been developed in our collaborative work with the group of Dr. F. Ortmann from TU Dresden. [43].

The transport of the charge carriers through i-MOS can be characterized into four different regions: Tunnel injection of the charge carriers, transport through the metal base, transmission across the metal/semiconductor interface and transport through the semiconductor. The processes described in this section are for hot electrons, but theory is also mainly valid for hot holes.

1.5.1 Tunnel injection of charge carriers

The bias between the emitter and the base, V_{EB}, determines the energy of the injected electrons. Tunnelling across the Al_2O_3 thin insulating barrier always result in a distribution of energy and momentum of the electrons. Similarly to common BEEM theory [31], [32], [52] the tunnel injection of non-equilibrium electrons is assumed to behave according to the planar tunnelling theory [54], [55]. Thus, the total emitter current I_E results from all electrons tunnelling through the barrier according to

$$I_E(U) = \int_0^U \mathrm{d}E\, I_t(U,E) \qquad \text{(Eq. 1.2)}$$

where $I_t(U,E) = I_0 t(U,E)$ is the energy-resolved tunnelling current and $t(U,E)$ the corresponding tunnelling probability, which has an exponential dependence with V_{EB} [43]. The energy E is counted from the base E_F. For $E < U$ $(U = -eV_{EB})$, the tunnelling probability is $t \propto \mathrm{e}^{bE}$, where b is a characteristic decay parameter describing the tunnelling. The tunnelling probability also depends on U due to the influence of the applied voltage on

the tunnelling barrier and on the maximum hot-electron energy (Fermi level of the emitter). As a result, at V_{EB} biases close to the threshold result in a sharply peaked distribution of the injected electrons perpendicular to the metal/semiconductor interface. The injected electrons have little momentum parallel to the metal base ($k_{\parallel} \ll k_{\perp}$).

1.5.2 Transport across the metal base

The scattering events occurred at the metal base broad the spatial and energetic distribution of the electrons. The hot electron attenuation length is described by a single parameter called the attenuation length $\lambda(E)$, which is energy dependent[42]. Moreover, it shows that the thicker the metal base more the current is attenuated. This comes due to the scattering events occurring in the metal base, which translates the total attenuation length λ as a parameter dependent of inelastic attenuation length λ_i and the elastic attenuation length λ_e [42]. This relation is given by Matthiessen´s rule:

$$\frac{1}{\lambda(E)} = \frac{1}{\lambda_i(E)} + \frac{1}{\lambda_e} \qquad \text{(Eq. 1.3)}$$

The spatial and energetic distribution of electrons in the metal base can be described by an exponentially decaying function depending on the injection angle θ, the metal film thickness d and the attenuation length:

$$\frac{I_B(t,E)}{I_T} \propto e^{\left(-\frac{d\cos\theta}{\lambda(E)}\right)} \qquad \text{(Eq. 1.4)}$$

Since the electrons are injected with nearly zero parallel momentum $k_{\parallel} = 0$, one can assume $\cos\theta \approx 1$, which simplifies Eq. 1.4 to

$$\frac{\boldsymbol{I_B(t,E)}}{\boldsymbol{I_T}} \propto \mathbf{e}^{\left(-\frac{\boldsymbol{d}}{\boldsymbol{\lambda(E)}}\right)} \qquad \text{(Eq. 1.5)}$$

1.5.2.1 Scattering mechanisms

All relevant scattering mechanisms for i-MOS experiment occur in the metal base.

Elastic scattering. This scattering mechanism changes the momentum of the electrons but conserves its total kinetic energy, which results in a broadening of the distribution of angular momentum. Electrons can scatter elastically at the boundaries of the base and move forth and back multiple times in the base. It can also occur in the bulk of the base and grain boundaries, impurities, defects or any inhomogeneities are the main elastic scattering sites [43].

Inelastic scattering. Inelastic scattering causes a lost in the energy of the electrons. There are two types of inelastic scattering. On the one hand, a direct relaxation to the Fermi level of the base can occur, where the electron loses its energy in a single step. Auger type scattering is one of these processes. On the other hand, there is a multiple process relaxation, where a small loss of energy happens many times. With each reflection at the metal/semiconductor interface there is a small probability of injection [43]. Typical processes of the later are coming from electron-phonon or electron-electron scattering [56,57].

1.5.3 Transmission across the metal/organic semiconductor interface

Electrons with emitter-base bias higher than the metal/organic semiconductor interface energy barrier $V_{EB} > \Delta$ can enter into the organic semiconductor. Electron states in the base can be "hot" (hot electron states) or thermalized at the Fermi level (thermal electron states). Only the latest exist in the collector current. Regarding transport hopping is allowed between the surface of the electrodes and the organic semiconductor. Once in the organic semiconductor, electrons hop from molecule to molecule following a Marcus hopping rate [58] or a Miller-Abrahams hopping rate [59], which depends on the nature (small molecule or polymer) of the organic semiconductor and the disorder level of the material.

1.6 This thesis

In this thesis, we base on in-device molecular spectroscopy, i-MOS, for the determination of energy level alignment at metal/organic semiconductor interfaces in device operative conditions. The work is organized as follows:

In chapter 1 we motivate our work and discuss the basic principles behind the i-MOS technique.

In chapter 2 we present the experimental techniques used to fabricate and characterize the three-terminal vertical devices.

In chapter 3 we attempt to study the energy barrier between the Fermi level of a metal and the LUMO level of an electron transporting polymeric semiconductor. We use the air-stable solution-processed poly{[N, N'-bis(2-octyldodecyl)-naphthalene-1,45,8-bis(dicarboximide)-2,6-dyl]-alt-5,5'-(2,2'-dithiophene)}[P(NDI2OD-T2), PolyeraActivInk N2200] as proof of principle. The *ex-situ* fabrication of the device permits us studying the effect that the contamination layer created between the metal and the polymer has in the energy barrier. We compare our results with ultraviolet photoemission spectroscopy and support them with a theoretical model.

In chapter 4, we extend the functionality of i-MOS determining not only the relative energy of the lowest unoccupied molecular orbital (LUMO), but also other molecular orbitals such as the first existed molecular level (LUMO +1) and the highest occupied molecular orbital (HOMO). We detect multiple molecular orbitals, and more particularly HOMO and LUMO, enables the determination of the transport gap of organic molecules. We also explore novel electronic transport regimes, such as an effective negative differential resistance (NDR) arising from Marcus Inversion phenomena. In this chapter we use C_{60}, C_{70} and PTCDI-C8 use n-type sublimated small molecules.

In chapter 5, we fabricate flexible i-MOS devices and we investigate the effects of the mechanical strain at the metal/molecule interface energy barrier with bending. We exemplify it with two structurally different electron transporting materials such as C_{60} and PTCDI-C8.

In chapter 6, we summarize the main conclusions of this thesis and we comment on the possible future projects that could be done as a continuation of this thesis.

References

1. Tang, C. W. Two-layer organic photovoltaic cell. *Appl. Phys. Lett.* **48,** 183–185 (1986).
2. Tang, C. W. & Vanslyke, S. A. Organic electroluminescent diodes. *Appl. Phys. Lett.* **51,** 913–915 (1987).
3. Forrest, S. R. The path to ubiquitous and low-cost organic electronic appliances on plastic. *Nature* **428,** 911–918
4. Kitaigorodsky, A. I. *Molecular crystals and molecules*. (Academic Press, 1973).
5. Singh, M., Haverinen, H. M., Dhagat, P. & Jabbour, G. E. Inkjet printing-process and its applications. *Adv. Mater.* **22,** 673–685 (2010).
6. Urdampilleta, M., Klyatskaya, S., Cleuziou, J., Ruben, M. & Wernsdorfer, W. Supramolecular spin valves. *Nat. Mater.* **10,** 502–506 (2011).
7. Nomura, K. *et al.* Room-Temperature fabrication of Transparent Flexible Thin-Film Transistors Using Amorphous Oxide Semiconductors. *Nature* **432,** 488–492 (2004).
8. Mesta, M. *et al.* Molecular-scale simulation of electroluminescence in a multilayer white organic light-emitting diode. *Nat. Mater.* **12,** 652–658 (2013).
9. Forrest, S. R. Electronic Appliances on Plastic. *Nature* **428,** 911–918 (2004).
10. Sirringhaus, H., Tessler, N. & Friend, R. H. Integrated Optoelectronic Devices Based on Conjugated Polymers. *Science (80-.).* **280,** 1741–1744 (1998).
11. Yan, H. *et al.* A high-mobility electron-transporting polymer for printed transistors. *Nature* **457,** 679 (2009).
12. Bernier, P., Bidan, G. & Lefran, S. *Advances in Synthetic Materials: Twenty Years of Progress in Science and Technology*. (1999).
13. Tessler, N., Preezant, Y., Rappaport, N. & Roichman, Y. Charge transport in disordered organic materials and its relevance to thin-film devices: A tutorial review. *Adv. Mater.* **21,** 2741–2761 (2009).
14. Groves, C. Simulating charge transport in organic semiconductors and devices: A review. *Reports Prog. Phys.* **80,** 26502–37 (2017).
15. Coropceanu, V. *et al.* Charge transport in organic semiconductors. *Chem. Rev.* **107,** 926–952 (2007).

16. Shirota, Y. & Kageyama, H. Charge Carrier Transporting Molecular Materials and Their Applications in Devices. *Chem. Rev.* **107,** 953–1010 (2007).

17. Zaumseil, J. & Sirringhaus, H. Electron and Ambipolar Transport in Organic Field-Effect Transistors. *Chem. Rev.* **107,** 1296–1323 (2007).

18. Ishii, B. H., Sugiyama, K., Ito, E. & Seki, K. Energy Level Alignment and Interfacial Electronic Structures at Organic / Metal and Organic / Organic Interfaces. *Adv. Mater.* **11,** 605–625 (1999).

19. Friend, R. H. *et al.* Electroluminescence in conjugated polymers. 121–128 (1999).

20. Chamberlain, G. A. Organic solar cells: a review. *Sol. Cell* **8,** 47–83 (1983).

21. Burroughes, J. H. *et al.* Light-emitting diodes based on conjugated polymers. *Nature* **347,** 539–541 (1990).

22. Koezuka, H. Field-effect transistors with polythiophene thin film. **18,** 699–704 (1987).

23. Sirringhaus, H. Device Physics of Solution-Processed Organic Field-Effect Transistors. *Adv. Mater.* **17,** 2411–2425 (2005).

24. Lo, M. F. *et al.* Limits of open circuit voltage in organic photovoltaic devices Limits of open circuit voltage in organic photovoltaic devices. *Appl. Phys. Lett.* **96,** 113303 (2012).

25. Kippelen, B. & Bredas, J. L. Organic photovoltaics. *Energy Environ. Sci.* **2,** 251–261 (2009).

26. Benanti, T. L. & Venkataraman, D. Organic solar cells : An overview focusing on active layer morphology. *Photosinthesis Res.* **87,** 73–81 (2006).

27. Hwang, J., Wan, A. & Kahn, A. Energetics of metal – organic interfaces : New experiments and assessment of the field. *Mater. Sci. Eng. R* **64,** 1–31 (2009).

28. Schwarze, M. *et al.* Band structure engineering in organic semiconductors. *Science (80-.).* **352,** 1446–1449 (2016).

29. Braun, S., Salaneck, W. R. & Fahlman, M. Energy-Level Alignment at Organic / Metal and Organic / Organic Interfaces. **21,** 1450–1472 (2009).

30. Pfeiffer, M., Leo, K. & Karl, N. Fermi level determination in organic thin films by the Kelvin probe method. **80,** 6880–6883 (1996).

31. Bell, L. D. & Kaiser, W. J. Observation of Interface Band Structure by

Ballistic-Electron-Emission Microscopy. *Phys. Rev. Lett.* **61,** 2368–2371 (1988).

32. Kaiser, W. J. & Bell, L. D. Direct investigation of subsurface interface electronic structure by ballistic-electron-emission microscopy. *Phys. Rev. Lett.* **60,** 1406–1410 (1988).

33. Atxabal, A. *et al.* Energy Level Alignment at Metal / Solution-Processed Organic Semiconductor Interfaces. *Adv. Mater.* **10,** 1606901–6 (2017).

34. Gobbi, M. *et al.* Determination of energy level alignment at metal/molecule interfaces by in-device electrical spectroscopy. *Nat. Commun.* **5,** 4161–4168 (2014).

35. Jiang, J. S., Pearson, J. E. & Bader, S. D. Direct Determination of Energy Level Alignment and Charge Transport at Metal - Alq 3 Interfaces via Ballistic-Electron-Emission Spectroscopy. *Phys. Rev. Lett.* **106,** 156807–4 (2011).

36. Parui, S. *et al.* Reliable determination of the Cu/n-Si Schottky barrier height by using in-device hot- electron spectroscopy. *Appl. Phys. Lett.* **107,** 183502–5 (2015).

37. Braun, B. S., Salaneck, W. R. & Fahlman, M. Energy-Level Alignment at Organic / Metal and Organic / Organic Interfaces. *Adv. Mater.* **21,** 1450–1472 (2009).

38. Ziegler, D. *et al.* Variations in the work function of doped single- and few-layer graphene assessed by Kelvin probe force microscopy and density functional theory. *Phys. Rev. B - Condens. Matter Mater. Phys.* **83,** 235434–235441 (2011).

39. Palermo, V., Palma, M. & Samori, P. Electronic characterization of organic thin films by Kelvin probe force microscopy. *Adv. Mater.* **18,** 145–164 (2006).

40. Nonnenmacher, M., O'Boyle, M. P. & Wickramasinghe, H. K. Kelvin probe force microscopy. *Appl. Phys. Lett.* **58,** 2921–2923 (1991).

41. Balkan, N. in *Hot electrons in semiconductors* 385–427 (Clarendon Press, 1998).

42. Parui, S. Hot electron transport in metallic spin valve and graphene-silicon devices at the nanoscale. (University of Groningen, 2013).

43. Arnold, T., Atxabal, A., Parui, S., Hueso, L. E. & Ortmann, F. Hot Electrons and Hot Spins at Metal-Organic Interfaces. *Adv. Funct. Mater.* **20,** 1706105–15 (2018).

44. Crowell, C. R. & Sze, S. M. Ballistic Mean Free Path Measurements of

Hot Electrons in Au Films. **15,** 659–661 (1965).

45. Milliken, A. M., Manion, S. J., Kaiser, W. J., Bell, L. D. & Hecht, M. H. Probing hot-carrier transport and elastic scattering using ballistic-electron-emission microscopy. *Phys. Rev. B* **46,** 12826–12829 (1992).

46. Kajen, R. S., Chandrasekhar, N., Su, H., Feng, X. & Klaus, M. Vibrational excitations in molecular layers. *Nanotechnology* **22,** 435701–435707 (2011).

47. Bell, L. D. Ballistic electron emission microscopy and spectroscopy: Recent results and related techniques. *J. Vac. Sci. Technol. B, Nanotechnol. Microelectron. Mater. Process. Meas. Phenom.* **34,** 040801-27 (2016).

48. Sirringhaus, H., Lee, E. Y. & Kanel, H. Von. Atomic-Scale Variations of the Tunneling Distribution in a Scanning Tunneling Microscope Observed by Ballistic-Electron-Emission Microscopy. *Phys. Rev. Lett.* **74,** 3999–4002 (1995).

49. Ludeke, R. & Prietsch, M. Ballistic electron emission spectroscopy of metals on GaP(110). *J. Vac. Sci. Technol. A* **9,** 885–890 (1991).

50. Yi, W. *et al.* Bandgap and band offsets determination of semiconductor heterostructures using three-terminal ballistic carrier spectroscopy. *Appl. Phys. Lett.* **95,** 112102–3 (2009).

51. Yi, W., Narayanamurti, V., Lu, H., Scarpulla, M. A. & Gossard, A. C. Probing semiconductor band structures and heterojunction interface properties with ballistic carrier emission: GaAs/ Alx Ga 1-x As as a model system. *Phys. Rev. B* **81,** 235325–13 (2010).

52. Bell, L. D., Hecht, M. H., Kaiser, W. J. & Davis, L. C. Direct spectroscopy of electron and hole scattering. *Phys. Rev. Lett.* **64,** 2679–2682 (1990).

53. Li, W. *et al.* Ballistic electron emission microscopy studies of Au/molecule/n-GaAs diodes. *J. Phys. Chem. B* **109,** 6252–6256 (2005).

54. Simmons, J. G. Electrodes Separated by a Thin Insulating Film. *J. Appl. Phys.* **34,** 1793–1803 (1963).

55. Appelbaum, I., Sheth, R., Shalish, I., Russell, K. J. & Narayanamurti, V. Experimental test of the planar tunneling model for ballistic electron emission spectroscopy. *Phys. Rev. B* **67,** 155307–4 (2003).

56. Grimvall, G. The Electron-Phonon Interaction in Normal Metals. *Phys. Scr.* **14,** 63–78 (1976).

57. Bardeen, J. & Pines, D. Electron-Phonon Interaction in Metals. *Phys.*

Rev. **99,** 1140–1150 (1953).

58. Marcus, R. A. Chemical and electochemical electron-transfer theory. *Annu. Rev. Phys. Chem.* **15,** 155–196 (1964).

59. Miller, A. & Abrahams, E. Impurity Conduction at Low Concentrations. *Phys. Rev.* **120,** 745–755 (1960).

Chapter 2

Experimental Methods

In this chapter we describe the equipment used in the fabrication and characterization of the three-terminal hot-electron devices employed in this thesis.

2.1 Sample Fabrication: Ultra High Vacuum Evaporation

All the devices described in this thesis have been produced in a ultra-high vacuum (UHV) evaporator fabricated by *Theva* and *Mantis* companies [1], [2]. The system is composed by three main chambers and a load-lock (Figure 2.1). One of the main chambers is dedicated for the organic molecule deposition while the other two are for the metals. The load-lock allows the insertion of samples in the system without breaking the vacuum in the main chambers. All chambers are provided with independent turbo pump systems. After bake-out process, the pressure in the main chambers arrives below 10^{-10} mbar. The bake-out process is different for each part of the system: A heating sleeve covers the *Theva* chambers while an internal filament is used for *Mantis* chamber.

The samples are clamped onto a copper sample holder (see Figure 2.2a), which is transferred from one chamber to the other with a magnetic arm without vacuum breaking. The sample holder is designed to fit substrates with a maximum size of 10×10 mm^2.

The top flanges of the main chambers are composed of a sample stage to fit the sample holder, a thickness monitor, a shutter and a mask holder. Sample stages are typically cooled with water although liquid nitrogen can

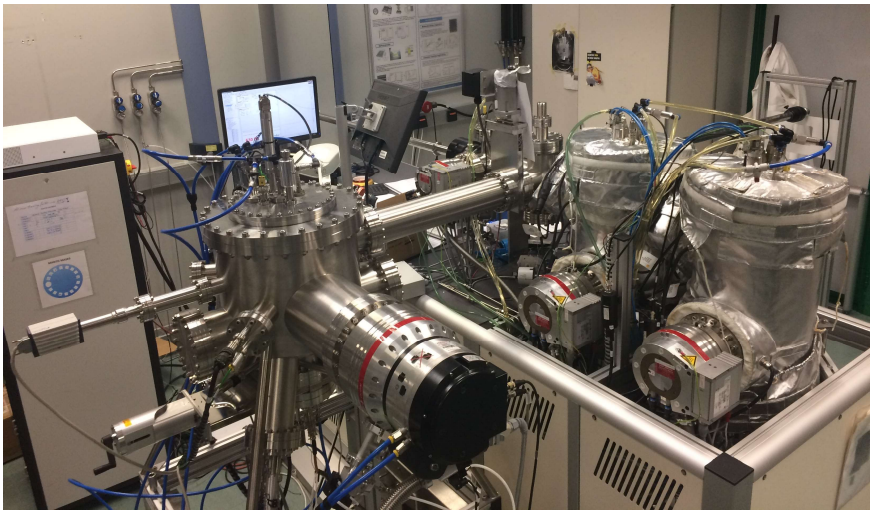

Figure 2.1| Photo of the UHV evaporator cluster.

be employed to reach a minimum temperature between 100-150 K. On the other side, the sample stage in the organic chamber and in the load-lock can be heated up to 250 °C with a resistance. A thermocouple is used for temperature monitoring.

The top flanges of the main chambers are composed of a sample stage to fit the sample holder, a thickness monitor, a shutter and a mask holder. Sample stages are typically cooled with water although liquid nitrogen can

be employed to reach a minimum temperature between 100-150 K. On the other side, the sample stage in the organic chamber and in the load-lock can be heated up to 250 °C with a resistance. A thermocouple is used for temperature monitoring.

A crystal monitor measures the amount of evaporated material. This is calibrated by measuring with X-Ray reflectivity the actual thickness of the deposited layer. A shutter between the sample and the material source can be opened and closed by a pneumatic actuator controlled by software and thus, the deposition of the material is only started when the desired rate is achieved.

The three main chambers incorporate a shadow mask system. A picture of the shadow mask and their holder is shown in Figure 2.2b. Indeed, all the devices described in this thesis have been patterned by evaporating throw these shadow masks on the substrate. The mask, a stein less steal foil with a patterned drilled, is placed in the proximity of the sample during the

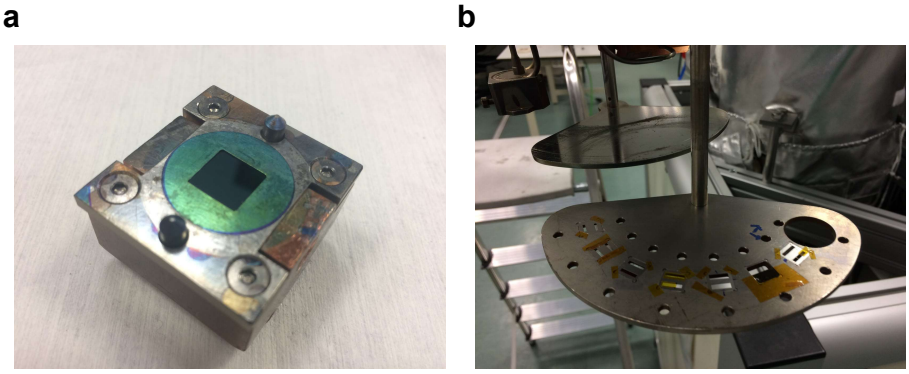

Figure 2.2| Sample and mask holders. a, Picture of the sample holder. **b,** Photo of the mask holder with seven different shadow masks.

deposition. Therefore, the material is only deposited on the substrate through the apertures in the mask, so that the pattern in the substrate mimics the shape of the mask. This fabrication technique allows in-situ device patterning without any kind of lithography. The feature size is limited to the order of 100 μm due to the accuracy of the drilling process. Each main chamber of *Theva* evaporator has a mask holder with 8 different shadow masks while the chamber of Mantis evaporator can host until 16 different.

2.1.1 Load-Lock

The load-lock is the chamber devoted to sample insertion and extraction without breaking the vacuum in the main chambers (Figure 2.3). In this way, the main chambers are vented and opened only to refill or change materials for evaporation.

Moreover, low power plasma treatments are done in the load-lock. Once a base pressure below 10^{-6} mbar is reached, it is possible to insert oxygen or argon into the chamber with the turbo pump on but at reduced speed (200 Hz instead of 1000 Hz). The gas pressure stabilizes around 0.1 mbar, and the plasma can be ignited by applying a high voltage between the sample stage and a glow discharge plate. The maximum plasma power is 60 W (1200 V and 50 mA). The oxygen plasma has been extensively used for

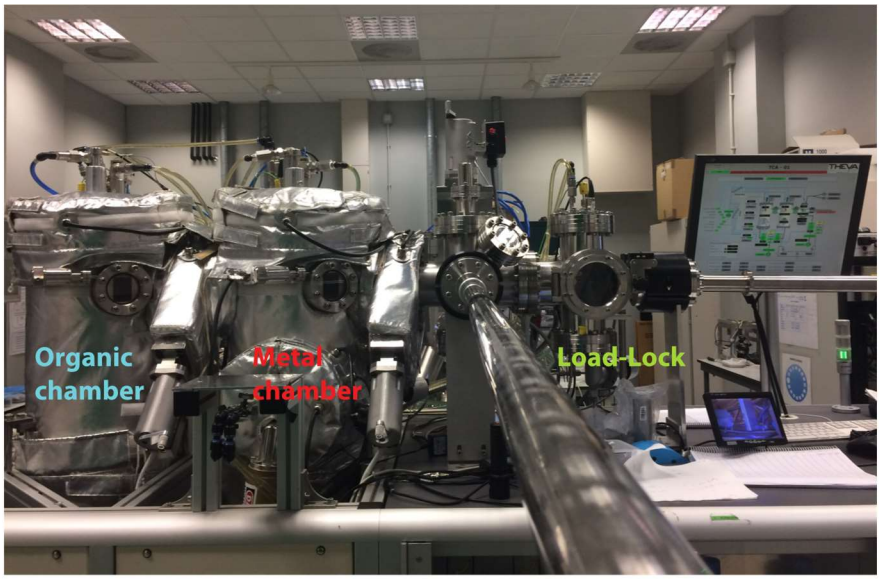

Figure 2.3| Theva evaporator cluster. The three parts that composing the *Theva* ultra high evaporator chamber are shown in this figure: the load-lock (green), the metal evaporator chamber (red) and the organic evaporator chamber (blue).

oxidizing aluminium films and form aluminium oxide tunnel barriers. This has been done by combining maximum power plasma (1200 V and 50 mA) and lower power plasma (1200 V and 10 mA). It is of extreme important the prior stabilization of the plasma for the uniform oxidation and good quality films

2.1.2 Metal Chamber Theva Evaporator

Metals are evaporated by electron-beam evaporation3 in a chamber dedicated exclusively to this purpose (Figure 2.3). For this technique, an electron beam is generated for thermionic emission by passing current through a filament (see Figure 2.4a). A perpendicular magnetic field and a high voltage focuses and accelerates the beam towards the evaporation material. The impact of the electrons with the material converts part of the kinetic energy of the electrons into heat. This causes material sublimation and deposition onto the substrate. A radiation shield protects the filament and materials from contamination (see Figure 2.4b).

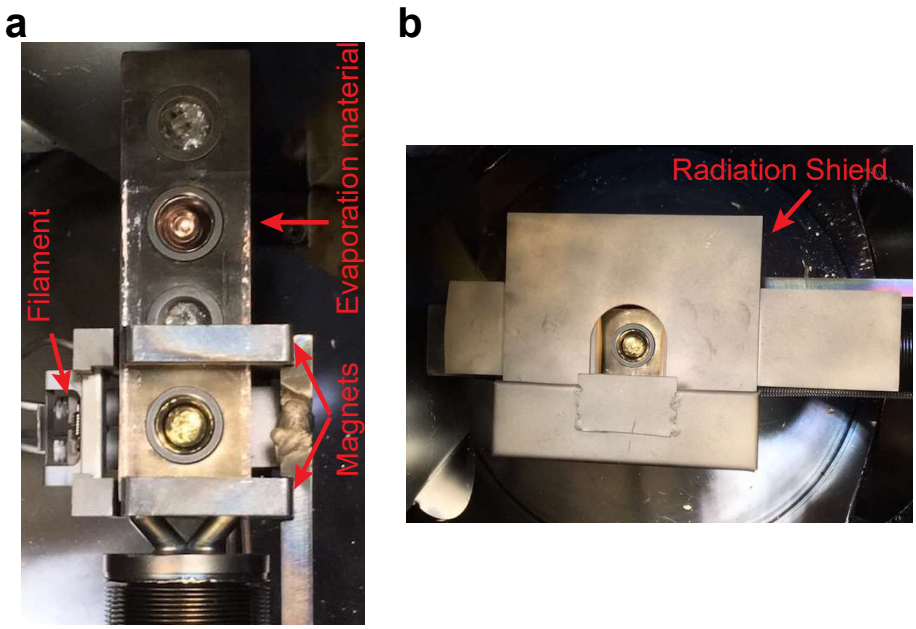

Figure 2.4| Inner view of the metal chamber. a, Photo of the e-beam evaporator of the metal chamber. The filament emits electrons, which are accelerated by a high voltage and deflected by permanent magnets towards the evaporation material. **b,** Picture of the radiation shield.

A UHV compatible *Telemark* 528 e-beam source with four pockets (see Figure 1.3a)[4] is used in our evaporator. The e-beam power supply has 3 kW maximum power, and each pocket has a capacity of 1.5 cc. The material source is placed just at 20 cm from the sample. While such a small distance is an advantage for the efficiency of the evaporation as the amount of deposited material on the chamber walls is minimized, it is a disadvantage for metal deposition on molecular layers because the radiation emitted during the e-beam evaporation might damage them [5-7].

2.1.3 Organic Chamber Theva Evaporator

Organics are thermally evaporated in a dedicated chamber (Figure 2.5). The chamber is equipped with three effusion cells and a low-temperature effusion cell from *MBE komponenten*[8]. Molecules in powder and into an elongated Quartz crucible from *MBE komponenten* [8] are used. A small filament uniformly heats the crucible along its entire length. When the

temperature is high enough, the molecules sublimate and are deposited onto the sample.

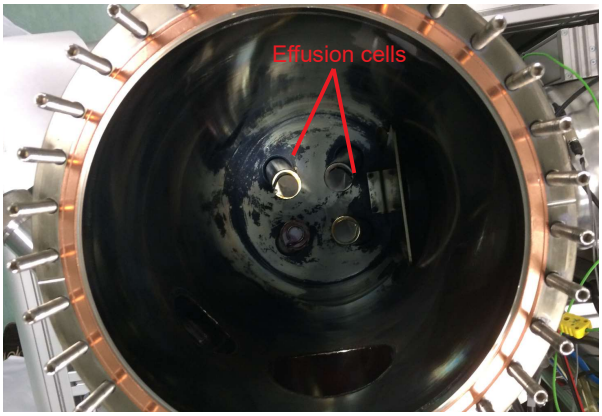

Figure 2.5| Inner view of the organic chamber. The chamber has four effusion cells.

The temperature is measured by a thermocouple in direct contact to the crucible wall and it is controlled by software through an *EpiTemp* controller. Besides the shutter under the sample stage, each effusion cell possesses also one. In this way, while the temperature is ramped up, the molecules are deposited on the shutter and not on the chamber walls. The maximum temperature that cells can reach is 800 °C. The organic evaporation is an easy process that only requires setting the sublimation temperature in the software and controlling the deposited thickness via the quartz crystal monitor. The base pressure is in the low 10^{-9} mbar range, and during molecule sublimation remains below 10^{-8} mbar.

2.1.4 Metal Chamber Mantis Evaporator

This chamber, which was incorporated later to the *Theva* evaporator, is exclusively devoted to metal evaporation (see Figure 2.6). Three different evaporation methods are integrated in this chamber: e-beam evaporator, thermal evaporation by boat source or by effusion cells. For the first method, four pocket mini e-beam evaporators *Quad-EV-C* are designed for the controlled evaporation of materials under UHV conditions. The sources are intended for applications in which film of thickness ranging from a

fraction of a monolayer to around 100 nm are to be deposited. The sources can be used to heat the target material to temperatures in excess of 3000 °C.

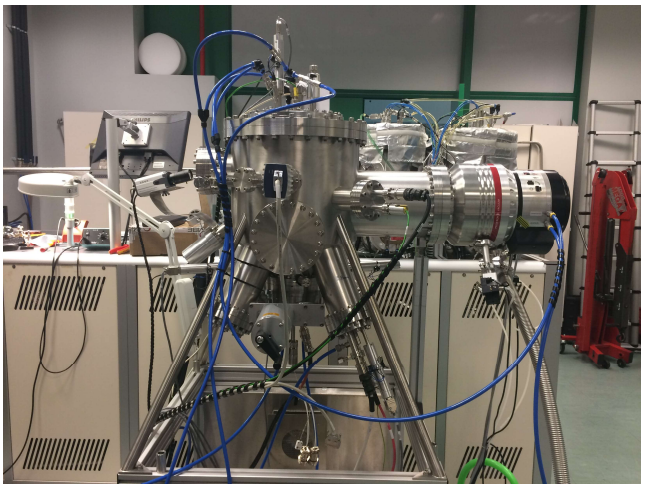

Figure 2.6| Picture of the metal chamber Mantis evaporator.

The principle of thermal boat source evaporation is to put the material to evaporate into a conductive boat, which is then heated by passing a high electrical current through it. As the temperature of the boat rises, the material in the boat starts to evaporate. In this way, the evaporation rate of the material is controlled by the amount of applied current. Four boats are separated with cross-contamination shielding and protected by individual shutters mounted on the main source flange. The source design ensures that every boat is equidistant from the central axis, which provides optimum film uniformity. The operation range is limited to a current of 100A, passing through the resistive element, which is roughly equivalent to a maximum boat temperature of around 2250°C (depending on type of boat used and type/amount of material loaded).

The two comcells of this chamber are thermal sources that contain wound tungsten filament to heat a conical crucible made of Pyrolytic Boron Nitride (PBN). The temperature of the material in the crucible can be controlled to an accuracy of better than ± 1 °C over a temperature range of several hundred degrees. This allows for very precise control of the deposition rate. The temperature is measured using a C-type basket that is

in contact with the crucible in several locations and provides an averaged measurement of the crucible temperature. The filament can handle a maximum power of 700 W, while the comcell tolerates a maximum operating temperature of 1300 ºC. The source is provided with an in-situ shutter that can b either manually or electrically actuated.

Even if the chamber offers the possibility of evaporating many different materials by the techniques explained above, we have limited its use only to aluminium thermal evaporation. The comcells were placed in angle arms what was creating diffraction patterns when the evaporation was done through shadow masks. Considering the convenience of this technique, which is softer than e-beam, for metal evaporation on organic layer and the good aluminium quality obtained, the effusion cell was moved to a vertical position with respect to the sample.

2.2 Electrical Characterization: Probe Stations

All vertical measurements presented in this thesis have been performed in one of two similar *LakeShore* probe stations (PS) shown in Figure 2.7a [9]. Four tips controlled by micrometric actuators and connected via triaxial cables to the measuring instrument make the electrical contact to the sample. Each probe station contains two radiation shields for minimizing external noise (see Figure 2.7b).

The two probe stations can perform measurements in vacuum with an applied magnetic field and at low temperatures. The base pressure at room temperature is 2×10^{-5} mbar, sufficient for the prevention of rapid degradation of molecular layers. A magnetic field in-plane to the sample can be applied with a maximum value of 0.6 T. The main difference of the two probe stations comes from the cooling system: one is equipped with a compressor which can cool the sample stage down to 4.9 K, while the other one arrives until 7 K with externally supplied liquid nitrogen or liquid helium. In both cases, special attention is required for low temperature performance of the system due to the thermal contraction of tips, which need to be positioned after the temperature is stabilized.

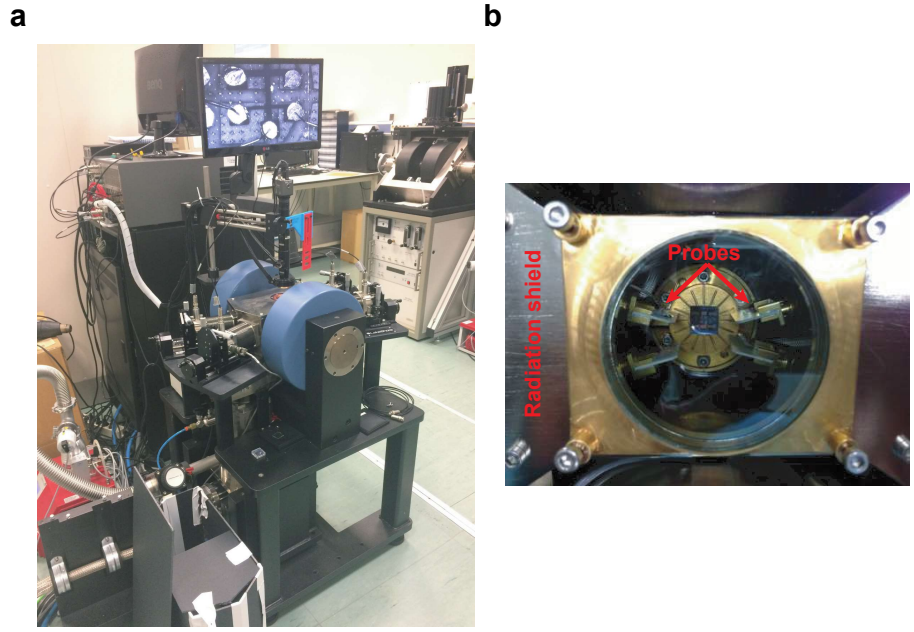

Figure 2.7| Picture of the chamber of the probe station. a, Set-up of the probe station. **b,** Photo of the tips on the sample stage.

Electrical measurements have been performed with a Keithley 4200 [10] equipped with three source-measurements units (SMU), two of which possess a current amplifier with sub-femto ampere nominal resolution. Triax cables and the radiation shield of the system enable to have a noise level below 10 fA when the circuit is open (tips not touching any sample). During actual measurements the mechanical instability of the contact between tips and sample is the main source of noise. In this sense, the noise level strongly depends on the material to be contacted, on its thickness and measurements conditions. Indeed, the compressor that lowers the temperature to 4.9 K introduces an unavoidable vibration that generates noise. This mechanical noise can be improved by using cold-pressing indium on the contacts and leaning the tips against the indium.

The control and synchronization of the electrical measurements with the magnetic field and the temperature were achieved by the implementation of basic programs in *Labview*. For in-device hot-electron spectroscopy, two software programs were used. The first one is set for current-voltage (*I-V*)

measurements in two terminals. The other one is also used for *I-V* measurements but in three terminals.

2.3 Material Characterization

In this section we briefly describe the basic principles of the techniques we use for material characterization.

2.3.1 X-Ray Reflectivity

X-ray reflectivity is a non-destructive method for surface and thin film characterization [11]. In this technique a very low incident angle X-ray beam hits a thin-film sample and then the intensity of the reflected ray is measured. The incidence angle scans only 2-3 degrees. For electromagnetic radiation with wavelength within the X-ray wavelength spectrum, the refractive index of any material is typically below unity. In this condition the Snell law for reflection determines that there is a critical angle below which X-ray will not penetrate into the material but will be completed reflected back. Above the critical angle, the electromagnetic waves penetrate into the sample and their intensity decreases down to a point where no reflection is detected. However, in between these two scenarios, there is a range in which the incoming radiation is partly reflected back at the film surface and partly enters into the sample to be reflected at the interface between substrate and the sample thin-film (Figure 2.8a).

Depending on the difference in the optical path, the two reflected rays will interfere constructively or destructively. Ergo, it is possible to detect interference peaks superimposed to the decay of the reflected beam intensity by scanning few degrees the incidence angle[11]. The peak position provides information about the separation between the reflecting planes and thus, the thickness of the film. A modified formula of the Bragg´s law is used to extract film thickness:

$$m\lambda' = m\left(\frac{\lambda}{n}\right) = 2d\sin\omega_{|} \qquad \text{Eq.(2.1)}$$

where m is the interference order, λ' and λ are the wavelength in the film and in air respectively, n is the film refractive index, d is the film thickness and $\omega_{|}$ is the incident angle.

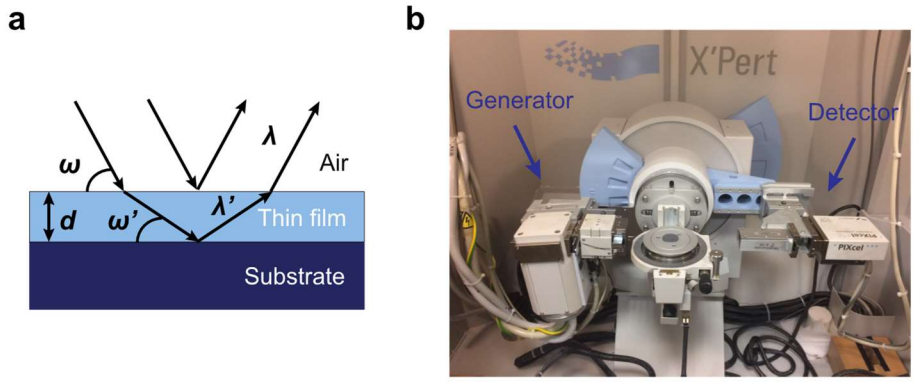

Figure 2.8| X-ray diffractometer. a, Scheme of X-ray diffractometer working principle. An X-ray with incident angle ω, both reflects and penetrates the surface of a thin film with thickness d. The ray that penetrates into the film reflects on the surface and between the film and the substrate, and return back to air. There, interference of both rays happens. **b**, Photo of the *Panalytical* X-ray diffractometer.

The surface roughness influences the way in which the X-rays are reflected. Indeed, a too rough surface would scatter incoherently the incident ray in every direction, and no interference would occur. Therefore, an accurate fit of the XRR spectra allows estimating interface and substrate roughness. The wide X-ray beam used, 2×2 mm^2, makes possible the acquisition of the long-range surface quality related roughness.

As the refractive index and the critical angle depends on the electronic density of the film, information about this last parameter can be also extracted from XRR scan.

Figure 2.8b shows the *Panalytical* X-ray diffractometer used in this thesis for both, X-ray reflection and diffraction measurements [12].

2.3.2 X-Ray Diffraction

In this technique an X-ray beam is irradiated with an angle ω to a three-dimensional periodically structured material and a especially well-

distributed intensity is scattered. This is the diffraction pattern and it is characteristic of the specific crystalline structure [13], [14]. The condition of constructive interference is given by Bragg´s law:

$$n\lambda = 2d \sin \theta \qquad \text{(Eq. 2.2)}$$

where d represents the interplanar spacing, λ the wavelength and n the reflection order. Changing symmetrically ω and θ angles and recording the intensity spectrum I (θ) all the possible diffraction peaks of the structure can be detected.

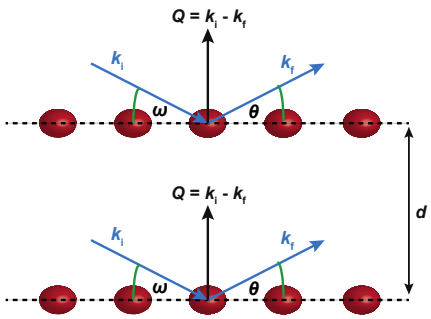

Figure 2.9| Schematic illustration of X-ray scattering in crystalline samples.

The angles at which constructive interference happens are directly related to the distance between planes d (Figure 2.9), which are perpendicular to the scattering vector Q, i.e. difference between incoming and scattering wave vectors. The diffracted peaks are associated to different crystallographic planes that satisfy Bragg´s law. Miller indexes classify these crystallographic planes.

2.3.3 Atomic Force Microscopy

Atomic Force Microscopy (AFM) is a high-resolution scanning probe technique in which the surface is scanned by a sharp tip with an atomic size termination, attached to a cantilever (see Figure 2.10a)). When the tip gets closer to the sample surface, it interacts with the surface and bends due to different forces, such as mechanical contact, van der Waals, electrostatic and magnetic forces. This bending is monitored by recording the deflection of a laser been on the cantilever by using a photodetector (see Figure 2.10a).

When tip/sample interaction begins, the piezoelectric actuator enables the surface scan. The result is a spatially resolved mapping of the forces between the tip and the surface.

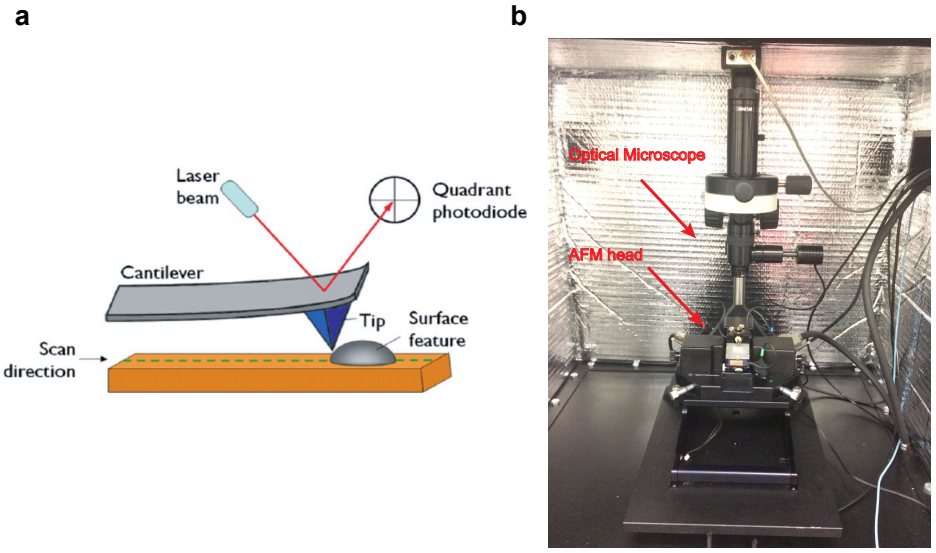

Figure 2.10| Atomic force Microscope (AFM). a, Schematic representation of an AFM. a, The figure shows the working principle of AFM. The tip deflects the cantilever when it faces a change in the morphology of the surface, and thus the laser beam is deviated. These deviations are measured by the photo-detector array. **b**, Picture of the AFM used in this thesis. It is enclosed into a cage to reduce the noise, and equipped with an optical microscope for positioning the cantilever in the desired position of the simple.

Drawing upon the different forces acting on the tip, diverse information can be extracted. We used tapping mode for the characterization of the topography of the samples. In this mode, a piezoelectric mounted in the tip holder makes the cantilever oscillate close to its resonance frequency. Tip-sample distance determines the oscillation amplitude, decreasing when tip gets close to the substrate and increasing when it moves away. A feedback loop keeps the cantilever vibrating at a fixed amplitude by moving the tip vertically closer or further to the sample when the oscillation amplitude tends to increase or decrease, respectively. In this way, the tip senses the surface morphology and the map of the vertical displacement of the tip as function of the in-plane coordinates result in a 3D graph that reproduces the

sample topography. Moreover, it has been shown that controlling the atomic composition of the very apex of the tip allows direct imaging of individual atoms inside a molecule lying on a surface and of the bonds inside the molecule. [15], [16] The resolution of the AFM depends among others, on the radius of curvature of the tip and the stability of the piezo.

The AFM instrument we used is from *Agilent Technologies* [17] (see Figure 2.10b). It is enclosed in a cage to minimize external noise. Even if the piezoelectric scanner allows obtaining images of 100 × 100 μm^2 size, in this project we were interested in measuring the nanometric scale roughness of organic semiconductor layers, so the typical image size was between 5 × 5 μm^2 and 25 × 25 μm^2. We employ commercial AFM Si/SiO_2 tips from Nanosensors, with a tip radius typically below 7 nm, which allow a lateral resolution below 50 nm.

The *Gwddion* software was used to analyse the AFM data. It allows a colour-scale 2D and 3D rendering of the topography as well as the extraction of surface roughness parameters such as RMS, which represents the "dispersion" of the heights with respect to the mean height by calculating the root mean square of the heights in every point. Peak to peak distance or the absolute difference between the highest and the lowest point in the image can also be extracted. Finally, it is possible to extract the average grain size of the sample.

2.3.4 Raman Spectroscopy

Raman spectroscopy is a technique used for the measurement of low frequency excitation modes in a system. It consists in shining a material with monochromatic light, usually from a laser in the visible, near infrared, or near ultraviolet range and detecting the energy shift of the backscattered light due to inelastic scattering events in the material. This energy shift is referred as Raman shift gives information about the vibrational modes of the material, which are fingerprints by which materials and their characteristics can be identified.

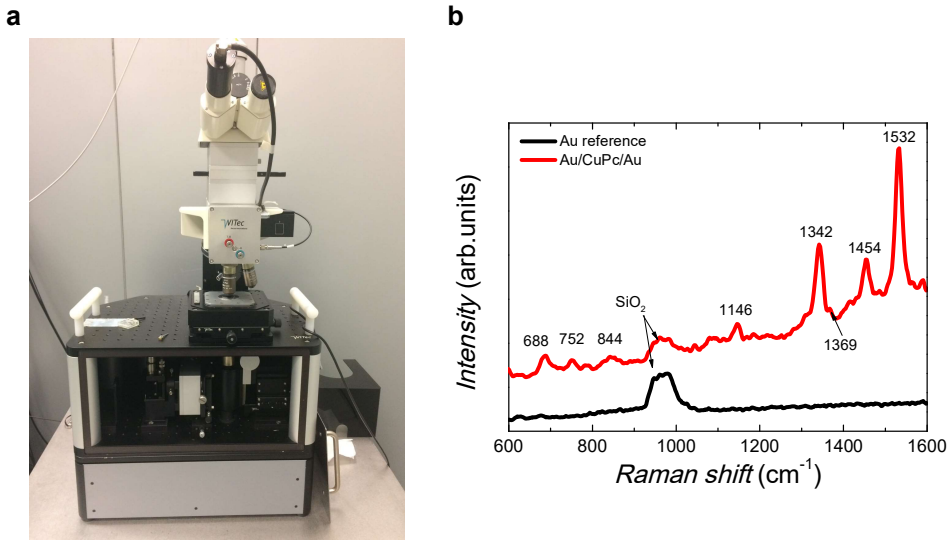

Figure 2.11| Raman spectroscopy. a, Photo of *WITec* confocal Raman spectrometer. **b,** Raman spectra for 20-nm-thick gold sample (black solid line) and 20 nm-thick gold sample sandwiched with 50 nm of CuPc (red solid line).

Figure 2.11a shows the *WITec* Confocal Raman system that we have used [18]. The sample is illuminated with a green laser (wavelength $\lambda \sim 532$ nm) and then, the electromagnetic radiation from the illuminated spot is collected with a lens and sent through a monochromator. The Rayleigh scattering or the elastic scattered radiation at the laser line is filtered out by while the rest of the collected light is dispersed onto a detector.

Raman spectroscopy has been widely used among other fields in chemistry for the identification of molecules, since vibrational information is specific to the chemical bonds and symmetry of molecules [19],[20]. Therefore, analysing the vibrational spectrum (see Figure 2.11b), the presence of molecules in samples can be resolved. The fingerprint region of organic molecules is in the (wavenumber) range of 500–2000 cm^{-1} Ref(19).

References

1. Theva. *www.theva.com*
2. Mantis. *www.mantisdeposition.com*
3. Sree Harsha, K. S. *Principles of physical vapor deposition of thin films*. (Elsevier, 2006).
4. Telemark. *www.telemark.com*
5. Haick, H., Ghabboun, J. & Cahen, D. Pd versus Au as evaporated metal contacts to molecules. *Appl. Phys. Lett.* **86,** 84–87 (2005).
6. Haick, H. & Cahen, D. Contacting organic molecules by soft methods: Towards molecule-based electronic devices. *Acc. Chem. Res.* **41,** 359–366 (2008).
7. Rybicki, J. *et al.* Tuning the performance of organic spintronic devices using X-ray generated traps. *Phys. Rev. Lett.* **109,** 076603-5 (2012).
8. MBE Komponenten. *www.mbe-komponenten.de*
9. LakeShore Probe Stations. *http://www.lakeshore.com* **18,** 25 (2005).
10. Keithley 4200. *http://www.tek.com/keithley-4200-scs-parameter-analyzer*
11. J. Als-Nielsen and D. McMorrow. *Elements of Modern X-Ray Physics*. (John Wiley & Sons, Ltd, 2001). doi:10.1002/9781119998365
12. Panalytical. *http://www.panalytical.com/Xray-diffractometers.htm*
13. Cullity, B. D. & Stock, S. R. *Elements of X-ray diffraction*. (Prentice Hall, 2001).
14. Birkholz, M. *Thin film analysis by X-ray scattering*. (Wiley-VCH, 2006).
15. Gross, L. *et al.* The Chemical Structure of a Molecule Resolved by Atomic Force Microscopy. *Science (80-.).* **325,** 1110–1114 (2009).
16. Agilent Technologies. *www.agilent.com/home* doi:10.1126/science.1227726
17. Agilent Technologies. *www.agilent.com/home*
18. WITec. www.witec.de/techniques/raman.
19. Lin-Vien, D., Colthup, N. B., Fateley, W. G. & Grasselli, J. G. *The Handbook of Infrared and Raman Characteristic Frequencies of Organic*. (Academic Press, 1991).
20. Jiang, N. *et al.* Observation of Multiple Vibrational Modes in Ultrahigh Vacuum Tip- Enhanced Raman Spectroscopy Combined with Molecular- Resolution Scanning Tunneling Microscopy. *Nano Lett.* **12,** 5061–5067 (2012).

Chapter 3

Energy Level Alignment at Metal/Solution-Processed Organic Semiconductor Interfaces

Intensive research efforts have been done over the last twenty years for the optimization of the performance of organic-based devices such as organic photovoltaic cells (OPV), organic light emitting diodes (OLED) and organic field effect transistors (OFET) [1–4]. This has led to the understanding of the impact of the energy barriers built up between the Fermi level of the metal and the molecular levels devoted to charge transport have on the device performance [5–7]. Typically, techniques such as electron photoemission spectroscopy, Kelvin probe measurements, and in-device molecular spectroscopy (i-MOS) have been applied to the study of interfacial energy barriers [8–13]. The first two methods are limited to extract the energy level alignment by monitoring the work function for thin molecular layers evaporated on the surface of a metal. These methods are far from device structure due to the complex equipment that they require. The third method, i-MOS, has however opened up the possibility to determine energy barriers between a metal and an organic semiconductor without using any material parameters and in-device operative conditions [12,13]. This is feasible due to its possibility of monitoring the current flow in a three-terminal

device, which is directly related with the charge injection into the metal/semiconductor interface. However, challenges and questions still remain regarding to this technique. In this chapter we tackle a twofold problem.

First, i-MOS devices have not been demonstrated in ex-situ fabrication conditions with polymers. As these materials can be processed over large area at low cost, they are closer to industrial plastic electronics (OPV, OLED, OFET, etc.) than many small molecules. Establishing this method as a quick, direct procedure for the measurement of the metal/polymeric semiconductor energy barriers is of great interest. So far, there are no suitable methods that enable the measurement of metal/lowest unoccupied molecular orbital (LUMO) energy barrier alignment when dealing with polymers. The most powerful one is probably inverse photoemission electron spectroscopy (IPES) [14]. However, the low resolution obtained with this technique and the damage it creates to the organic film by exposing the sample to energetic electrons limits its use to only well stabilised small molecules such as C_{60} or 3, 4, 9, 10-perylenetetracarboxylic dianhydride [14]. Second, it is not still clear the effects of ex-situ fabrication of the devices; i.e. how the impurity layer created between the metal and the organic semiconductor affects the charge injection into the last one. In order to solve this question and translate it into industrial application a device approach is required.

In this chapter, we measure the interfacial energy barrier between a metal and a solution processed electron-transporting polymer by using i-MOS and we compare them with standard ultraviolet photoemission spectroscopy (UPS) measurements [9]. The data is complemented with the development of a theoretical model, which connects the results coming from the two techniques, i-MOS and UPS.

3.1 Fabrication of the devices

The i-MOS devices described in this work are three terminal devices composed of an emitter, a base and a collector (see Figure 3.1). The emitter is a 13 nm thick aluminium contact, which later is plasma-oxidized in-situ to create an AlOx tunnel barrier. Plasma oxidation is done for three minutes at 1200V, 50 mA and 0.1 mbar. All the metallic parts described in this chapter were evaporated by e-beam in UHV conditions and with a shadow mask

system. The base consists of a 10-nm thick layer of gold. Gold was chosen for being a commonly used material for device contacts. Its air stability and noble properties make it a suitable metal for, among others, prepatterned devices.

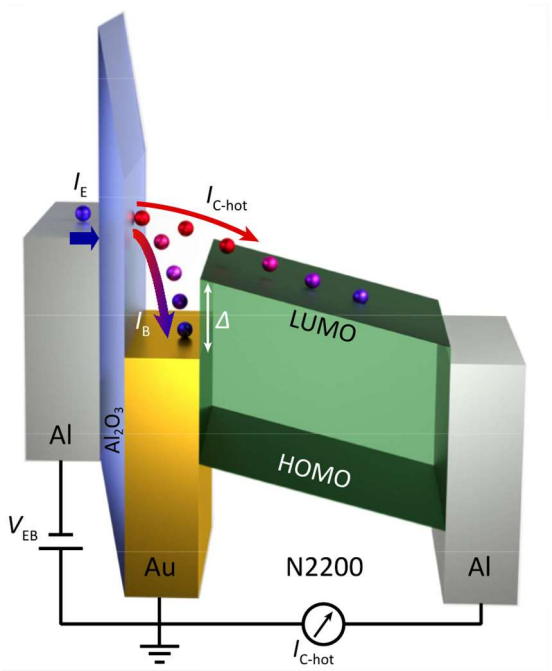

Figure 3.1|Scheme of the working principle and the energy levels of the device in rigid band approximation. The tunnelling current I_E flows from the emitter to the base when a negative bias V_{EB} is applied at the emitter/base terminals. A major part of this injected current is attenuated in the base and collected as I_B while the other part of I_E flows ballistically to the base/collector interface. When the bias V_{EB} is higher than Δ, a fraction of the I_E flows into the N2200 and is measured as I_C. This current is collected without any external bias applied between the base and the collector terminals.

This emitter-base sample is then spin coated with a solution of poly{[N, N'-bis(2-octyldodecyl)-naphthalene-1, 4, 5, 8-bis(dicarboximide)–2, 6–dyl]-alt-5, 5'-(2, 2'-dithiophene)} [P(NDI2OD-T29, PolyeraActiveInk N2200] [15] (see the chemical structure in Figure 3.2a). We chose this particular polymer due

to its high electron mobility and stability under ambient conditions. These properties make of this polymer a promising material for future technological applications [15–17]. The solution was prepared with 5 mg of N2200 (>99.9%) dissolved in 1 mL of $CHCl_3$ (99.9%) (extra dry, stabilized, AcroSeal). 90 µL of this solution were spin coated on the sample for 60 s at 4000 rpm and 1000 rpm s^{-1} in the clean room. This concentration and spin coating recipe were the optimal ones for maximizing electron detection in the collector and minimizing the top metal and minimizing filaments coming from metallic top contact. In order to evaporate the residual solvent in the sample before the evaporation of the top metallic contact, this was kept in vacuum (10^{-6} mbar) for two hours. Profilometry measurements were performed on several concentration solution processed polymer thin films in order to determine the thickness of the organic layer (see Figure 3.2b). The thickness of the polymer thin film used in i-MOS sample is ≈ 90 nm.

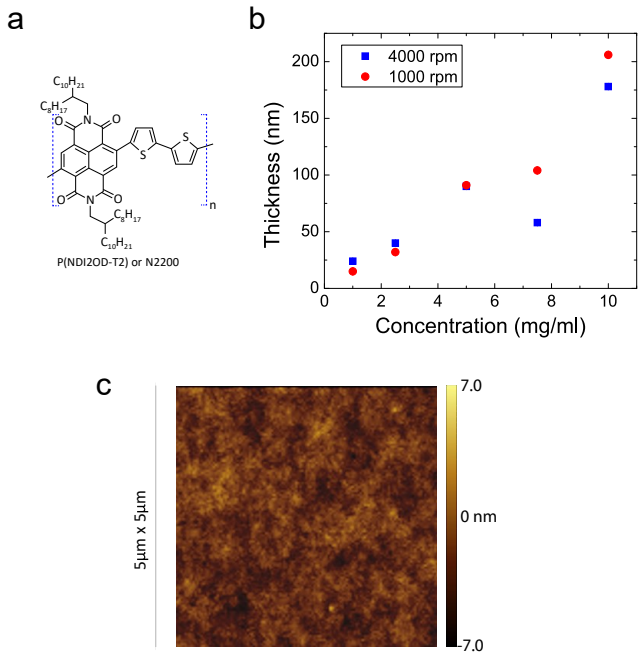

Figure 3.2| Chemical structure of N2200 and N2200 thin film characterization. **a,** Chemical structure of N2200 polymer. **b,** Profilometry measurements of thin film samples of 1, 2.5, 5, 7.5 and 10 mg mL^{-1} concentrated N2200 solution. Each concentration is compared for 1000 rpm and 4000 rpm of spin coating speed. **c**,

Atomic force microscopy (AFM) image of N2200 film on SiO_2 substrate. The root mean square (RMS) roughness of the films is determined to be 3.6 ± 0.1 nm.

The top electrode is a 13 nm thick aluminum film. This metal was chosen as top electrode due to the good energetic matching of its Fermi level with the LUMO of the N2000 polymer. In order to minimize the damage of the organic surface and avoid penetration of the metal in the organic semiconductor a double step evaporation is followed in its fabrication. Firstly, 4 nm-thick Al is evaporated at 1 Å s^{-1} in order to cover the roughness of the N2200 layer and avoid penetration. Atomic force microscopy (AFM) was performed in order to determine the roughness (see Figure 3.2c). Secondly, 9 nm thick Al is evaporated at 1 Å s^{-1}. The evaporation rate is increased in this second step in order to reduce the heating of the sample due to prolonged evaporation and thus avoid damaging the organic layer surface.

3.2 Electrical characterization

The first method used for the extraction of metal/solution processed organic semiconductor interface energy barriers is i-MOS. Although this technique has already been applied for the determination of the energy level alignment at metal/inorganic semiconductor and metal/small molecule semiconductor interfaces, in this work we use i-MOS for the determination of energy barriers between a metal and a polymeric semiconductor [10,12,13,18].

Figure 3.3 shows the characterization of the device for temperatures from 290 K to 110 K. The I_E - V_{EB} characteristics of the tunnel junction, Al/AlOx/Au are shown in Figure 3.3a. The resistance slightly increases when lowering the temperature, which confirms that we have non-leaky tunnel junction [19] as intended. Regarding the Au/N2200/Al stack, applying an external bias between base and collector, V_{CB}, the diode current, I_{diode}, is measured in Figure 3.3b. On the one hand, a rectifying behaviour is observed with I_{diode} higher when electrons are injected by the top Al layer ($V_{CB} < 0$) than when they are coming from the base gold ($V_{CB} > 0$). This result suggests the formation of high-energy barriers at the Au/N2000 interface.

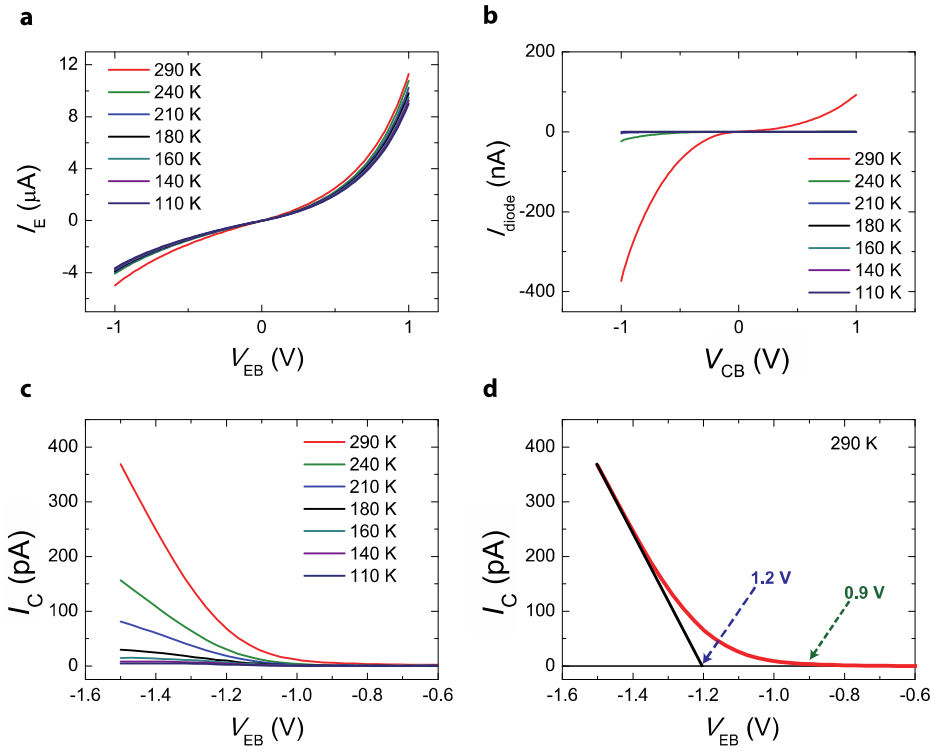

Figure 3.3| Electrical characterization of the device. a, Temperature dependence of the emitter current I_E measured at two terminals in the Al/AlOx/Au tunnel junction as a function of the applied bias V_{EB}. **b**, Temperature dependence of the I_{diode} current measured at two terminals in the Au/N2200/Al stack as function of applied bias V_{CB}. **c**, Hot electron current $I_{C\text{-}hot}$ measured in the Au/N2200/Al stack as function of applied bias V_{EB} for temperatures from 290 K to 110 K. **d**, I_C measured as function of the applied bias between the emitter and the base V_{EB} at 290 K and the linear fit to $I_C = 0$ to obtain the barrier height Δ.

On the other hand, the temperature evolution of the measured I_{diode}-V_{CB} shows a considerable decrease of I_{diode}, typical of transport through a thick-layer organic semiconductors [20]. Once we have verified that the individual parts of the device (tunnel junction and diode) work properly, we proceed to the hot electron current measurement, i.e. I_C - V_{EB}. Figure 3.3c shows the I_C - V_{EB} characteristics for temperatures from 290 K to 110 K. The current I_C is measured without any external applied bias between the base and the collector, and thus, I_C can be considered as a purely diffusive current. This is

possible due to both the momentum of the injected electrons perpendicular to Au/N2200 interface and to the built-in potential created by sandwiching the polymer with two metallic contacts with different work functions [21,22]. We can see that I_C is four orders of magnitude lower than I_E, which is characteristic of hot electrons in semiconductors [12]. Figure 3.3d shows also I_C - V_{EB} curved but only at 290 K and together with the linear fit of the growth of the current $I_{C\text{-hot}} = 0$ line [21,22]. Even if more complex fittings that consider the tunnelling probability and the density of states of the semiconductor can be used, Gobbi *et al.* [12] have already demonstrated that the linear fitting of the linear increase in $I_{C\text{-hot}}$ is reliable strategy. So, using this straightforward method, the energy barrier Δ between gold and N2200 is estimated to be 1.2 ± 0.1 V (dotted blue arrow). We fabricated four chips containing several working devices in different deposition rounds. The average barrier value measured is 1.2 ± 0.1 V. The device-to-device variation in each chip is lower than the measurement precision, while the maximum variation from chip to chip is ± 0.1 V. The dotted green arrow points out the onset of the nonzero I_C at 0.9 ± 0.1 V. This value corresponds to the energy barrier for charge injection into the polymer interface states [12].

3.3 Ultraviolet photoemission spectroscopy measurements

i-MOS provides two important information about the metal/semiconductor interfaces: the value of energy barrier in device operative conditions and an evidence of how this interfacial energy barrier determines the charge injection into the semiconductor. However, as i-MOS is a relatively novel technique for the study of metal/organic semiconductor energy barriers, there can be some apprehension in the organic electronics community to make use of it. In order to vanish any doubt regarding the reliability of i-MOS, we have complementary compare our results with well-stabilised method as UPS [9,23]. Contrary to IPES, UPS is an indirect method as it can only probe occupied states and thus, many approximations must be done for reaching a metal/LUMO energy value. However, the damage produced in the organic film and the low resolution obtained with the former method have made UPS a more suitable technique for the extraction of metal/LUMO

energy barrier. For this purpose, we have collaborated with the group of Prof. Mats Fahlman from Linkoping University in Sweden, whose group is expert on UPS measurements on organic materials. They have performed all the UPS measurements shown in this chapter, which were done on samples that we provided to them (gold on Si_2O_3, N2200 on Si_2O_3 and N2200 on gold).

Figure 3.4a shows the HeI survey scan of an N2200 film on gold. The frontier edge of the occupied electronic structure is typically taken as the vertical ionization potential (IP) referenced to the Fermi energy (0 eV) in the figure. To get an IP value referenced to the vacuum level, the work function of the sample is determined from the so-called secondary electron cut-off, Figure 3.4b. The UPS measurements carried out gave an IP of 5.7± 0.1 eV with work functions of 4.7 ± 0.1 eV.

Spin-coated films of conjugated polymers such as N2200 are typically polycrystalline or amorphous, yielding significant variation in the local order of the polymer chains and creating a distribution of ionization energies. Every polymer (segment) in such a film will consequently feature an individual IP and electron affinity (EA). The frontier parts of the resulting occupied and unoccupied state distributions forming the energy gap are often modeled as being either Gaussian or exponential and the most easily oxidized/reduced states in a organic semiconductor film are commonly referred to as tail states or gap states. The energy level alignment at weakly interacting metal/polymer interfaces obtained from physisorbed films can be described by the so-called integer charge transfer (I_{CT}) model. Spontaneous charge transfer across the interface occurs when the substrate work function is larger (smaller) than the energy required to oxidize (gained from reducing) a polymer at the interface forming an integer charge transfer state. The integer charge transfer state ($I_{CT+,-}$) energies depends on the inter- and intramolecular order, just as for the bulk ionization energies, so that at a given interface there hence will be a distribution of I_{CT+} and I_{CT-} energies. The $I_{CT+,-}$ energies are generally different from the bulk ionization (IP/EA) values due to the interaction with the image charge (pushing the ICT states into the gap as compared to the bulk) but also due to that the substrate surface (roughness, surface energy) can induce a different film morphology at the interface than in the bulk. The most easily oxidized (or

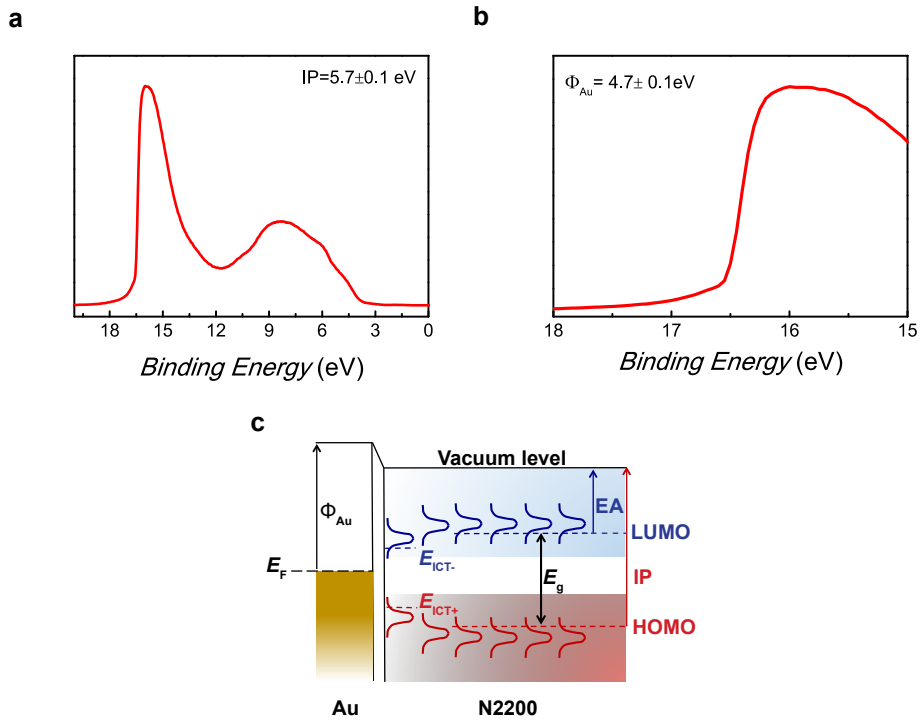

Figure 3.4| Ultraviolet photoemission spectroscopy (UPS) measurements. a, Ionization potential of the N2200 measured with UPS (Ultraviolet Photoemission Spectroscopy). A 90-nm-thick N2200 layer is spin coated on Au (14 nm)/AlOx (20 nm)/SiOx (200 nm)/Si. **b,** Work function of gold measured with UPS. The gold is deposited on top of AlOx (20 nm)/SiOx (200 nm)/Si and is covered with 90 nm of N2200. **c,** Au/N2200 interface energy diagram. E_F is the Fermi energy and Φ_{Au} the work function of gold. LUMO corresponds to the lowest unoccupied molecular orbital, HOMO to the highest occupied molecular orbital, IP to the ionization potential, EA to the electron affinity and E_g to the energy band gap of the N2200 polymer. The integer charge transfer states are represented as E_{ICT+} and E_{ICT-}.

reduced) polymer segments adjacent to the interface are "used up" in the spontaneous charge transfer process until enough charge has been transferred across the interface to create a potential step that equilibrates the Fermi level, with the resulting pinning energies being referred to as the $E_{ICT+,-}$. These values can be calculated using a variety of computational approaches or measuring by among others, UPS techniques. In our case, a

negative pinning energy of 3.9± 0.1 eV has been obtained, which is in good agreement with Kelvin probe derived results in literature [24]. The small variation in work function (± 0.1 eV) between films is partly the experimental error but also due to variation in the starting gold surface as well as film formation at the Au/N2200 interface, and is in the range of previous studies of polymer-gold interfaces [25].

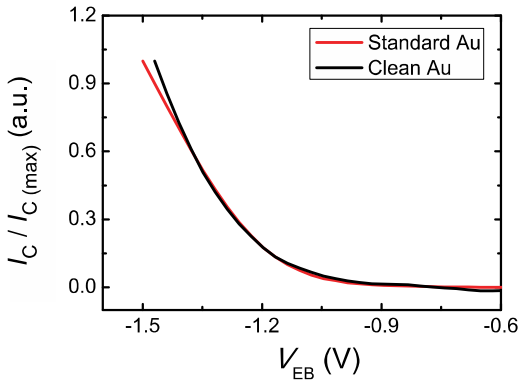

Figure 3.5| Comparison of the energy barrier of clean gold and untreated gold. Measured hot electron current normalized to $I_C / I_{C\,(max)}$ as a function of the applied bias V_{EB} at 290 K. $I_{C\text{-}hot\,(max)}$ corresponds to the maximum value of the measured hot electron current. The red curve corresponds to the standard device with non-clean base gold and the black curve corresponds to oxygen-plasma-cleaned base gold device.

Therefore, the electron injection barrier at the Au/N2200 interface can be estimated from the UPS values as 4.7 eV (ϕ_{Au}) – 3.9 eV (LUMO energy) = 0.8 ± 0.1 eV. However, we must consider that this barrier represents the injection of an electron into the edge of the N2200 n-polaron (relaxed singly-occupied LUMO) distribution at the gold interface, where the image charge effect shifts the energy deeper into the gap compared to the bulk n-polaron distribution (see Figure 3.4c), a well-known effect from both device physics and interface energy level alignment [26–28]. The size of the shift from interface to bulk depends on a variety of factors, which include the organic film morphology and its dielectric constant, with values in literature ranging between 0.3 eV up to 0.7 eV [27–29]. Hence, the electrons injected into the edge states are bound at the interface and will not make it to the collecting

contact as no driving voltage is applied (see section 1.5). In fact, only electrons injected near the center (~0.5 σ, being $\sigma$the width of the Gaussian energy disorder) of the bulk n-polaron distribution are expected to contribute to the current under these conditions (see Figure 3.4c) [30,31]. Taking the lower value of 0.3 eV for the image charge-induced shift between interface and bulk we get a total barrier for the conditions of ballistic injection current in the device as 0.8 eV + 0.3 eV =1.1 eV. Both the interface energy barrier and bulk energy barrier values are in good agreement with the direct experimental observation performed by in-device hot electron spectroscopy, albeit if several approximations have been needed for the extraction of the bulk energy barrier.

3.4 Effect of the contamination layer on i-MOS

Figure 1.4b shows a change in the work function of gold after having exposed it to air. This is a well-known experimental result for UPS measurements, but it is not still clear if such contamination layer might modulate the transport energy barrier when it is measured by i-MOS. In order to disentangle this question, we fabricate a hot electron device in which the gold interface is cleaned with oxygen plasma for five minutes in the clean room just before the spin coating of the polymer. Figure 3.5 shows I_C of the clean gold (black solid line) and the untreated gold (red solid line) samples normalized to the maximum value this current $I_C/I_{C\,(max)}$ as function of V_{EB} at 290 K. No difference is the energy barrier value is observed when we compare both samples. This result indicates that the contamination layer coming from air exposure of gold does not affect substantially the carrier injection.

3.5 Modelling

For a better understanding of our results we have collaborated with the group of Frank Ortmann from TU Dresden in Germany, who has developed a theoretical model for the hot-electron transistor. The model is kept simple but includes the different parts of the device as illustrated in Figure 3.6a. The central part is the polymer film, represented as hopping sites by balls

and which is sandwiched between gold and aluminum electrodes. Hot-electrons are injected with a rate ν through the base into the polymer as illustrated by black arrows. The charge transport in the polymer is modeled as hopping transport between localized states (sticks between balls), while electron transfer from Au (Al) into the polymer and back is possible via the Au (Al) Fermi level. The model is based on the Poisson equation and transport Master equation, which are simultaneously solved.

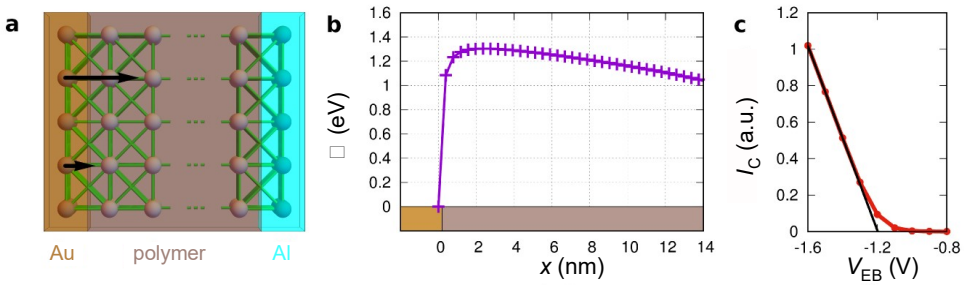

Figure 3.6| Theoretical model for the experimental data. a, Structural model of the Au/N2200/Al heterostructure. The polymer is represented electronically by hopping sites (indicated by balls in the central region), which are connected by hopping rates (sticks). **b**, Energy levels as a function of distance *x* to the Au surface, calculated from the electrostatic potential (for V_{EB} = -1.2 V). **c**, Simulated hot-electron current-voltage characteristics (red) and extrapolation of threshold voltage to -1.2 V (black).

Hot carrier operation is assumed by setting V_{CB} = 0V (Φ = 0 eV is the metal Fermi level). When no hot electrons are provided at the base (ν = 0), the electron affinity of the polymer interface states is expected, which is increased by an image charge of 0.3 eV, to be at 3.8 eV (i.e. Φ=0.9 eV). This choice for the energy level of the lowest polymer states at 0.1 eV above the pinning onset of 3.9 eV is due to interfacial energetic disorder and finite temperature which leads to the onset of charging of the lowest polymer states (pinning) at such offset. When hot electrons are provided with a finite rate ν and V_{EB}=-1.2 V, the solution of the equations yields the potential distribution shown in Figure 3.6b. The resulting potential is dominated by the built-in potential and the image-charge potential close to the Au/N2200 interface. In addition, a small space-charge contribution close to the interface occurs at the chosen injection conditions.

Figure 3.6c summarizes the calculated $I_{C\text{-}hot}$ for varying V_{EB}. At small hot-electron energy ($|V_{EB}| \leq 1.1$ V) the electrons can hardly reach the transport levels of the bulk polymer although the lowest polymer states close to the interface may be populated, i.e. electrons cannot escape the barrier from the image-charge and $I_{C\text{-}hot}$ is suppressed. This barrier can be overcome by further increasing $|V_{EB}|$, which provides more electrons with higher energies. Note that the hot-electrons arrive with energies continuously distributed between zero and $|V_{EB}|$. From linear fitting of the calculated $I_{C\text{-}hot}$, the onset corresponding to the Au/N2200 interface energy barrier is extracted to be at V_{EB}=-1.2 eV. These results are in good agreement with the ones obtained by in-device hot electron spectroscopy in section 3.2.

3.6 Conclusions

We have shown that i-MOS is a reliable and straightforward method for the determination of metal/polymeric semiconductor energy barriers, making their use convenient for the engineering of commercial ex-situ fabricated organic electronic devices. Having proven well performing i-MOS devices with solution-processed polymers makes the method a handy tool for the general organic electronics. Moreover, our results are confirmed by a well-established technique such as UPS. This shows to be a reliable but non-direct method for the determination of interfacial transport energy barriers, thus highlighting the importance of our technique.

We have also determined that the contamination layer coming from the air exposure of the devices in the fabrication process does not play a significant role. Our experimental work has been complemented by a theoretical model developed for transport in hot-electron devices. This model has given a further understanding on the role of the interfaces in hot-electron devices as well as highlighting the existing differences between the two techniques employed.

This work gives a new approach to the study of metal/polymeric semiconductor interfaces as well as probing a new designing tool for organic electronics.

References

1. Holliday, S. *et al.* High-efficiency and air-stable P3HT-based polymer solar cells with a new non-fullerene acceptor. *Nat. Commun.* **7,** 11585–1196 (2016).
2. Lee, J. *et al.* Deep blue phosphorescent organic light-emitting diodes with very high brightness and efficiency. *Nat. Mater.* **15,** 92–98 (2015).
3. Muccini, M. A bright future for organic field-effect transistors. *Nat. Mater.* **5,** 605–613 (2006).
4. Forrest, S. R. Electronic Appliances on Plastic. *Nature* **428,** 911–918 (2004).
5. Friend, R. H. *et al.* Electroluminescence in conjugated polymers. *Nature* **397,** 121–128 (1999).
6. Lo, M. F. *et al.* Limits of open circuit voltage in organic photovoltaic devices Limits of open circuit voltage in organic photovoltaic devices. *Appl. Phys. Lett.* **96,** 113303 (2012).
7. Sirringhaus, H. Device Physics of Solution-Processed Organic Field-Effect Transistors. *Adv. Mater.* **17,** 2411–2425 (2005).
8. Hwang, J., Wan, A. & Kahn, A. Energetics of metal – organic interfaces : New experiments and assessment of the field. *Mater. Sci. Eng. R* **64,** 1–31 (2009).
9. Braun, B. S., Salaneck, W. R. & Fahlman, M. Energy-Level Alignment at Organic / Metal and Organic / Organic Interfaces. *Adv. Mater.* **21,** 1450–1472 (2009).
10. Parui, S. *et al.* Reliable determination of the Cu/n-Si Schottky barrier height by using in-device hot- electron spectroscopy. *Appl. Phys. Lett.* **107,** 183502–5 (2015).
11. Ohno, T. R., Chen, Y., Harvey, S. E., Kroll, G. . & Weaver, J. H. C60 bonding and energy-level alignment on metal and semiconductor surfaces. *Phys. Rev. B* **44,** 13747–13755 (1991).
12. Gobbi, M. *et al.* Determination of energy level alignment at metal/molecule interfaces by in-device electrical spectroscopy. *Nat. Commun.* **5,** 4161–4168 (2014).
13. Jiang, J. S., Pearson, J. E. & Bader, S. D. Direct Determination of Energy Level Alignment and Charge Transport at Metal - Alq 3 Interfaces via Ballistic-Electron-Emission Spectroscopy. *Phys. Rev. Lett.* **106,** 156807–4 (2011).

14. Djurovich, P. I., Mayo, E. I., Forrest, S. R. & Thompson, M. E. Measurement of the lowest unoccupied molecular orbital energies of molecular organic semiconductors. *Org. Electron.* **10,** 515–520 (2009).

15. Yan, H. *et al.* A high-mobility electron-transporting polymer for printed transistors. *Nature* **457,** 679 (2009).

16. Mu, C. *et al.* High-Effi ciency All-Polymer Solar Cells Based on a Pair of Crystalline Low-Bandgap Polymers. *Adv. Mater.* **26,** 7224–7230 (2014).

17. Caironi, M. *et al.* Very Low Degree of Energetic Disorder as the Origin of High Mobility in an n -channel Polymer Semiconductor. *Adv. Funct. Mater.* **21,** 3371–3381 (2011).

18. Parui, S. *et al.* Hot electron transmission in metals using epitaxial NiSi 2 / n-Si (111) interfaces. *Appl. Phys. Lett.* **99,** 032104-3 (2011).

19. Sun, X. *et al.* Room temperature air-stable spin transport in bathocuproine-based spin valves. *Nat. Commun.* **4,** 2794–7 (2013).

20. Baldo, M. A. & Forrest, S. R. Interface-limited injection in amorphous organic semiconductors. *Phys. Rev. B* **64,** 085201-17 (2001).

21. Bell, L. D. & Kaiser, W. J. Observation of Interface Band Structure by Ballistic-Electron-Emission Microscopy. *Phys. Rev. Lett.* **61,** 2368–2371 (1988).

22. Kaiser, W. J. & Bell, L. D. Direct investigation of subsurface interface electronic structure by ballistic-electron-emission microscopy. *Phys. Rev. Lett.* **60,** 1406–1410 (1988).

23. Ishii, B. H., Sugiyama, K., Ito, E. & Seki, K. Energy Level Alignment and Interfacial Electronic Structures at Organic / Metal and Organic / Organic Interfaces. *Adv. Mater.* **11,** 605–625 (1999).

24. Lange, I. *et al.* Band Bending in Conjugated Polymer Layers. *Phys. Rev. Lett.* **106,** 216402–4 (2011).

25. Braun, S., Jong, M. P. De, Osikowicz, W. & Salaneck, W. R. Influence of the electrode work function on the energy level alignment at organic-organic interfaces Influence of the electrode work function on the energy level alignment at organic-organic interfaces. *Appl. Phys. Lett.* **91,** 202108–3 (2007).

26. Bao, Q. *et al.* Energy Level Bending in Ultrathin Polymer Layers Obtained through Langmuir – Shäfer Deposition. *Adv. Funct. Mater.* **26,** 1077–1084 (2016).

27. Zhao, L.-H. *et al.* Semiconductor films Polarization effects on energy-level alignment at the interfaces of polymer organic semiconductor films. *Appl. Phys. Lett.* **101,** 053304-4 (2012).

28. Lindell, L., Vahlberg, C., Uvdal, K., Fahlman, M. & Braun, S. Self-assembled monolayer engineered interfaces : Energy level alignment tuning through chain length and end-group polarity. *J. Electron Spectros. Relat. Phenomena* **204,** 140–144 (2015).

29. Zhu, X.-Y. Charge Transport at Metal - Molecule Interfaces : A Spectroscopic View. *J. Phys. Chem. B* **108,** 8778–8793 (2004).

30. Germs, W. C., van der Holst, J. J. M., van Mensfoort, S. L. M., Bobbert, P. A. & Coehoorn, R. Modeling of the transient mobility in disordered organic semiconductors with a Gaussian density of states. *Phys. Rev. B* **84,** 165210–7 (2011).

31. Cottaar, J., Koster, L. J. A., Coehoorn, R. & Bobbert, P. A. Scaling Theory for Percolative Charge Transport in Disordered Molecular Semiconductors. *Phys. Rev. Lett.* **107,** 136601–4 (2011).

Chapter 4

Multilevel molecular spectroscopy and Marcus Inverted Region

The engineering of molecular semiconductor-based technologies requires a precise knowledge of key parameters, such as the relative energetic position of the molecular levels devoted to charge transport and the energy value of the bulk transport energy gap [1–6]. However, in the case of the last parameter, the lack of a reliable and straightforward technique often results in the adoption of other energy gaps, such as the molecular fundamental, first principles, optical or interface ones [7]. The molecular fundamental gap is the energy gap of a single-molecule obtained by scanning tunnelling microscopy (STM) [8,9]. The energy gap of single molecules is typically higher than the bulk one due to the strong polarization coming from the π-conjugated molecules [7,10]. The use of Kohn-Sham gap from density functional theory on the other hand has no formal justification and is thus dependent on the cancelation of intrinsic errors and inadequacies present in this method [7]. Moreover, the optical gap, commonly measured by ultraviolet-visible spectroscopy (UV-VIS), is different from the transport gap due to the strong exciton binding energy of molecules [7,11–14]. In the case of some organic semiconductors such as C_{60} fullerenes, the optical transition associated to the transport states may be symmetry forbidden and thus, higher onsets might be measured with UV-VIS. Finally, the combination of different

surface-sensitive techniques, such as ultraviolet photoemission spectroscopy (UPS) and inverse photoemission spectroscopy (IPES) [15–17], enables the determination of the surface energy gap. It differs from transport energy gap due to the low resolution of IPES, the uncertain probing depth at the organic-vacuum interface and other surface dependent parameters such as roughness and image charge potentials [18].

In the first part of this chapter, we based on in-device molecular spectroscopy (i-MOS) technique to directly determine the relative energetic positions of various molecular orbitals, such as the highest occupied molecular orbital (HOMO) and the lowest unoccupied molecular orbital (LUMO) with respect to the Fermi energy of the base metal, as well as the transport energy gap of bulk films of C_{60} and C_{70} fullerenes. This milestone has been achieved by a single vertical three-terminal solid-state device and without any prior knowledge of the material parameters. In the second part of the chapter, we study charge transport at metal/organic semiconductor interfaces in the case of direct electronic processes at i-MOS devices.

4.1 Device fabrication

All the devices described in this chapter were fabricated *in-situ* in ultra-high vacuum (UHV) and with a shadow mask system. The emitter is a 12 nm-thick aluminium contact (99.95% purity, Lesker), which was thermally evaporated in an effusion cell with a rate of 0.6 Å s^{-1}. Then, the Al_2O_3 tunnel junction was made by plasma oxidizing the aluminium contact first, for two minutes at low power (1200V and 10 mA at 0.1 mbar) and then, for three minutes at high power (1200V and 50 mA at 0.1 mbar). A 10 nm-thick gold base (99.95% purity, Lesker) was e-beam evaporated at 1.0 Å s^{-1} as base contact. Gold was chosen because it is a weakly interacting metal with organic materials. 200 nm of n-type C_{60}, triple-sublimed quality (99.9%, Sigma Aldrich), was thermally evaporated with a rate of 0.1 Å s^{-1}. Same procedure has been followed for devices with n-type C_{70} (98% purity, Sigma Aldrich) fullerene, which has been used as a substitute of C_{60}. In the case of C_{70} based devices 100nm-thick semiconductor film has been evaporated due to the lower conductivity of this molecule compared to C_{60} [19,20]. Finally, a 12 nm-thick aluminium top electrode was again thermally evaporated. This metal is chosen as top electrode due to the good energetic matching of its

Fermi level with the LUMO of C_{60} and C_{70} films. Table 4.1 summarizes the device fabrication steps. In order to optimize the deposition of the top aluminium on the organic films, the roughness of 200 nm thick C_{60} (Figure 4.1a) and 100 nm thick C_{70} (Figure 4.1b) have been extracted by mapping the surface topography by atomic force microscopy (AFM). In the case of C_{60} the root mean square roughness is 1.6 ± 0.1 nm, while in the case of C_{70} is 1.5 ± 0.1 nm. Moreover, the two organic films seem to be amorphous. Considering the roughness of the films, a two-step deposition has been followed: first, 2 nm aluminium at 0.1 Å s^{-1} in order to cover the surface roughness and avoid the penetration of energetic metallic atoms. Then, 0.6 Å s^{-1} rate evaporation until total film thickness of 12 nm to avoid burning the organic surface due to prolonged evaporation time.

Table 4.1|Device fabrication recipe. The table summarizes the steps followed in the fabrication of the devices described in this chapter.

Layer	Material	Thickness	Evaporation rate
Emitter	Al	12 nm	0.6 Å s^{-1}
	O_2	2' (1200 V, 10 mA) + 3' (1200 V, 50 mA)	
Base	Au	10 nm	1.0 Å s^{-1}
Collector	C_{60}	200 nm	0.1 Å s^{-1}
	C_{70}	100 nm	
Top Contact	Al	2 nm + 10 nm	0.1 Å s^{-1}+0.6 Å s^{-1}

In addition, X-ray diffraction (XRD) measurements with grazing incidence have been performed to further understand the morphology of the organic fims. Figure 4.1 is the diffraction pattern of $Si/Si_2O_3/Al_2O_3/Au/C_{60}$. Three peaks are observed in this diffraction pattern but they correspond to Au (100), Au(200) and Au (220). No peak corresponds to C_{60}, which confirms that the semiconductor film is amorphous. Figure 4.1d is the difraction pattern of 100 nm-thick C_{70} film on Si/Si_2O_3. The absence of difraction peaks corroborates that this semiconductor layer is amorphous. This is an additional information for the understanding of the device structure.

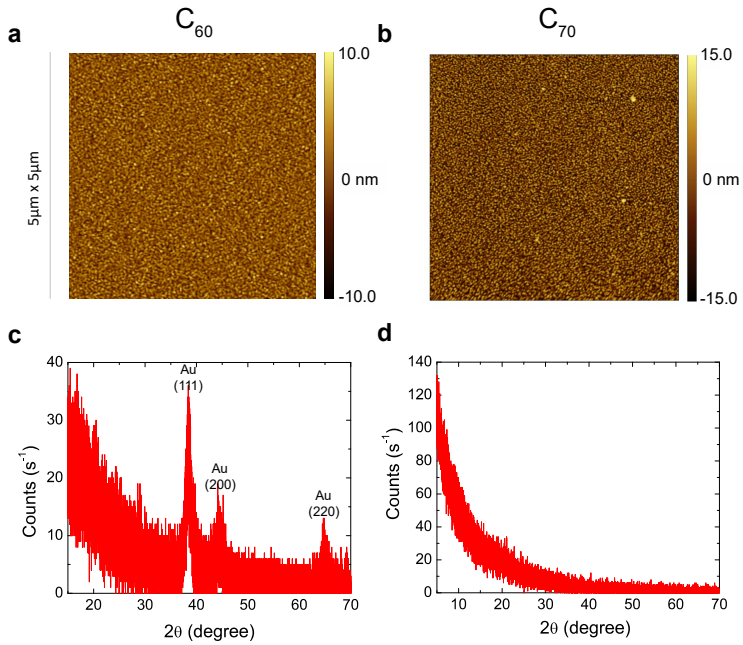

Figure 4.1| Characterization of C_{60} and C_{70} films. a, Surface topography of 200 nm thick C_{60} film on 10 nm-thick gold film extracted by atomic force microscopy (AFM). **b**, AFM image of 100 nm-thick C_{70} film on SiO_2 surface topography. **c**, Grazing incidence X-ray diffraction (XRD) measurement of thermally evaporated 200 nm thick C_{60} film on 10 nm-thick gold film. Three peaks are observed in the diffraction patterned, which corresponds to Au (111), (200) and (220) [21,22]. No peak has been observed for C_{60}, which suggests that the semiconductor film is amorphous. **d**, Grazing incidence XRD pattern of 100 nm-thick C_{70} film on SiO_2 chip. The absence of peaks in the diffraction pattern indicates the amorphous morphology of the film.

4.2 Device characterization

In this section we electrically characterize i-MOS devices. First, we separately check by two terminal measurements the reliability of tunnel barrier and the molecular junction. Second, we perform three-terminal measurements of the device for spectroscopy studies of the molecular levels. We follow these steps for both C_{60} and C_{70} based samples.

4.2.1 C_{60} based i-MOS

The current-voltage (*I-V*) characteristics of C_{60} based i-MOS devices are shown in this section. Prior to the three terminal i-MOS measurements, the different counterparts of the device have been individually characterized. Figure 4.2a shows the emitter-base current, I_E, flowing through the tunnel junction when the bias V_{EB} is swept between the emitter and the base for temperatures from 300 K to 120 K. Non-linear *I-V* traces, typical of tunnel junctions, are recorded. The resistance of the junction slightly increases when lowering the temperature, as expected for continuous tunnel junctions [23,24].

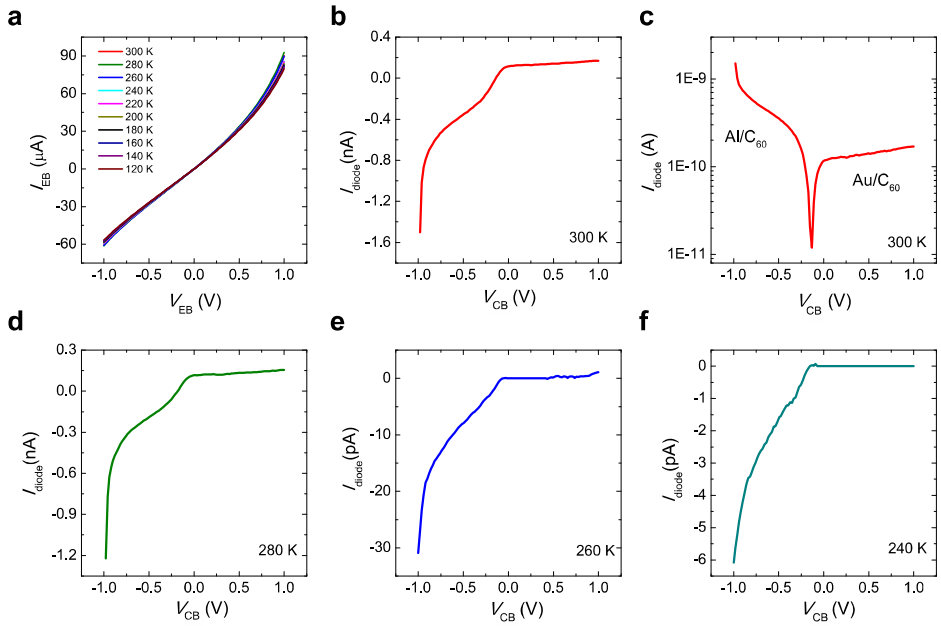

Figure 4.2| Electrical characterization of device counterparts. a, Current I_E measured at two terminals in the $Al/Al_2O_3/Au$ tunnel junction as function of the applied bias between emitter and base, V_{EB}, for 300 K-120 K temperature range. **b**, I_{diode} current measured at two terminals in the $Au/C_{60}/Al$ stack as function of the applied bias between the base and the collector V_{CB} at 300 K. **c**, I_{diode} current in logarithmic scale as function of V_{BC} at 300 K. **d**, I_{diode} – V_{CB} trace at 280 K. **e**, I_{diode} – V_{CB} measured at 260 K. **f**, V_{CB} dependence of I_{diode} at 240 K.

In Figure 4.2b we show the current I_{diode} flowing across the C_{60} when the

voltage V_{CB} is applied directly between the base and the top aluminium contact. The 200 nm thick C_{60} layer is highly resistive and the *I-V* curve is again highly non-linear. This asymmetry is more pronounced in logarithmic scale in Figure 4.2c, which means that more electrons are injected from the top aluminium contact to the molecular semiconductor than from gold base contact. This fact suggests that the barrier for electron injection is lower for aluminium than for gold. The matching of the Fermi level of aluminium with the LUMO of C_{60} is well known [25]. Nevertheless, one needs to have in mind that conventional two terminal diode measurements comprise the contribution of the contact and the bulk resistance. The temperature evolution of I_{diode}-V_{CB} shows an increase in the resistivity when the sample is cooled down (Figure 4.2b-f).

Figure 4.3 shows the working principles of i-MOS together with the measured current in the collector I_C for various voltage biases between the emitter and the base, V_{EB}. When a negative bias V_{EB} is applied, a current I_E is injected from the emitter into the base by tunneling through the Al_2O_3 barrier. These electrons are "hot" in the base as their energy is well above the Fermi level of the metal, and a small fraction of them crosses the thin metallic base ballistically without any significant energy attenuation [18, 26, 27]. For the case in which the applied bias is $V_{EB} \geq \Delta$ (Δ = metal-semiconductor energy barrier), some of the injected hot electrons enter into the LUMO level of C_{60} while the remaining flow back into the base. At higher energies, electrons can enter the excited conductive states of C_{60}, such as LUMO+1. Since C_{60} is a n-type semiconductor and it is sandwiched between two metallic contacts with different work functions, the built-in potential enables the detection of I_C without any applied V_{CB} (Figure 4.3a) [28, 29]. This process is shown in Figure 4.3e where I_C versus V_{EB} for V_{CB} = 0V is plotted, with two onsets associated with the relative position of molecular orbitals devoted to electron transport (LUMO and LUMO+1). Under a negative applied V_{CB} (Figure 4.3b), the electric field in the collector-base junction repulses hot electrons and leads to the injection of holes into the HOMO level of the n-type semiconductor, thus enabling the determination of the relative energy of that molecular level with respect to the E_F of the base metal (Figure 4.3f). These holes are created by the inelastic scattering of the incident hot electrons in the gold metal base with cold electrons (below the

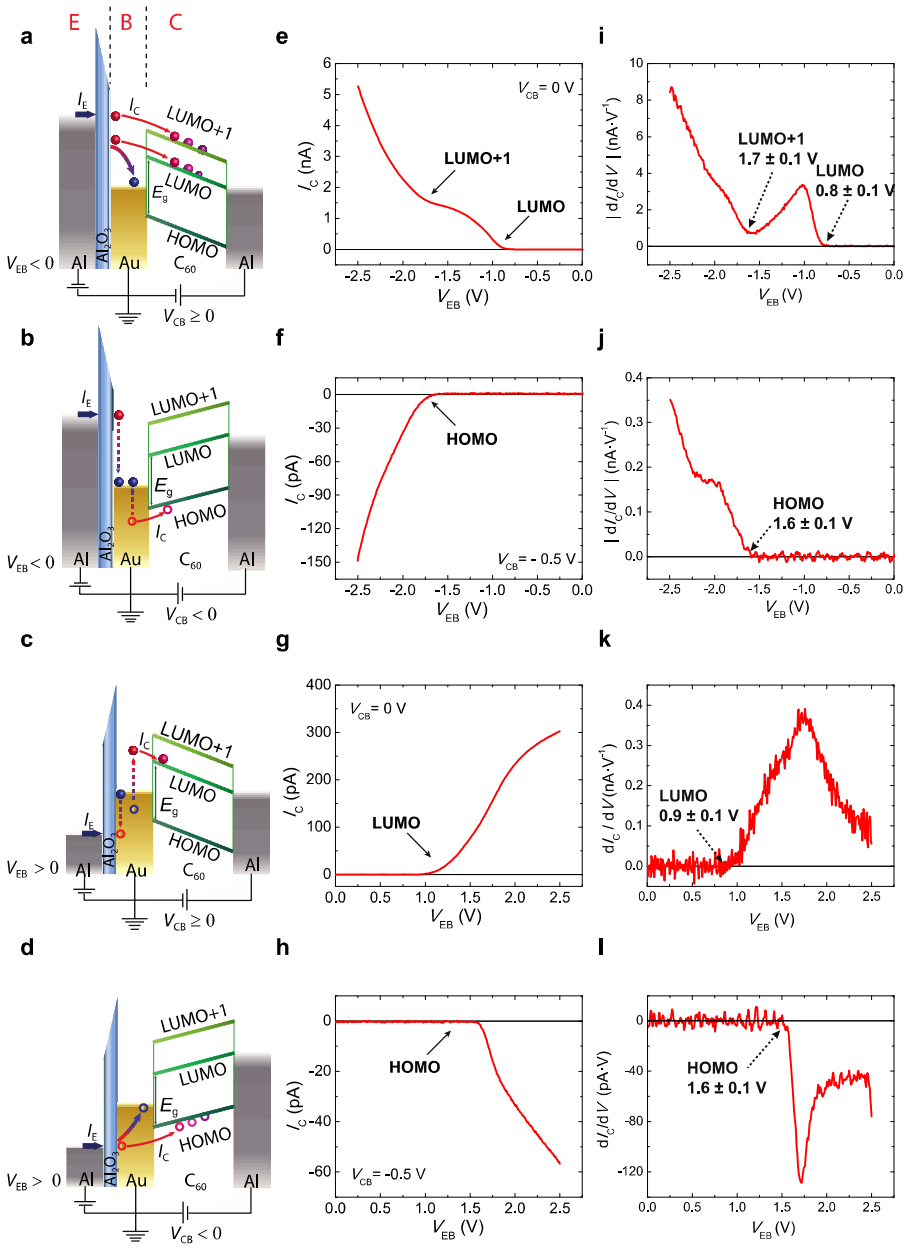

Figure 4.3| In-device molecular spectroscopy (i-MOS) operation under different emitter-base bias V_{EB} polarities at room temperature. a, Schematic representation of the direct process in which electrons are injected by applying a negative emitter-base bias, $V_{EB} < 0$ V, and detected in the molecular semiconductor. The measurements can be performed either without any externally applied

collector-base bias, V_{CB}, or by $V_{CB} \geq 0V$. **b**, Schematic representation of the secondary process at i-MOS when electrons are injected, $V_{EB} < 0$ V, into the device but holes are detected. $V_{CB} < 0V$ is required in order to counteract the built-in potential and help hole injection into and transport through the organic semiconductor. **c**, Schematic representation of the secondary process at i-MOS when holes are injected into the device, $V_{EB} > 0$ V, but hot electrons coming from a similar effect to Auger scattering are detected with $V_{CB} \geq 0V$. **d**, Schematic representation of the direct process at i-MOS when holes are injected, $V_{EB} > 0$ V, and detected with $V_{CB} < 0V$. **e**, Collector current I_C for $V_{EB} < 0$ V at room temperature. Energetic electrons are injected with $V_{CB} = 0V$ both into the lowest molecular orbital (LUMO) and into the first excited conductive molecular level (LUMO+1) states of C_{60}. Notice that in the current configuration, positive I_C indicates electron current detection whereas negative I_C corresponds to hole current detection in C_{60}. **f**, Detected I_C for $V_{EB} < 0$ V and $V_{CB} = -0.5$ V. Injection of a hole current into C_{60} leads to the detection of its highest occupied molecular orbital (HOMO) states. **g**, Electron current, I_C, and LUMO states detected with $V_{EB} > 0$ V and $V_{CB} = 0$ V. **h**, I_C for $V_{EB} > 0$ V and $V_{CB} = -0.5$ V. Injection of energetic holes permits the detection of the HOMO states of C_{60} in a direct process. **i**, Derivative of the I_C respect to V_{EB} when $V_{EB} < 0$ V and $V_{CB} = 0$ V for the extraction of the energy of LUMO and LUMO+1 of C_{60} at 0.8 ± 0.1 eV and 1.7 ± 0.1 eV, respectively. **j**, Derivative of the I_C respect to V_{EB} when for $V_{EB} < 0$ V at $V_{CB} = -0.5$ V. An energy value of 1.6 ± 0.1 eV is extracted for the relative position of HOMO of C_{60}. **k**, Relative energy of LUMO of C_{60} at 0.9 ± 0.1 eV after the derivative of the I_C respect to V_{EB} when for $V_{EB} > 0$ V and $V_{CB} = 0$ V. **l**, Derivative of the I_C respect to V_{EB} when for $V_{EB} > 0$ V and $V_{CB} = -0.5$ V. 1.6 ± 0.1 eV is extracted as the relative position of HOMO of C_{60}.

Fermi level) [30]. A similar mechanism operates for positive V_{EB}, but in this case holes are injected to the base instead of electrons. Figure 4.3c represents an Auger-like scattering process in which incident energetic holes excite secondary electron-hole pairs in the gold metal base and thus hot electrons are created [31–33]. Figure 4.3d shows the direct process of hole-injection and hole-detection, respectively. Figure 4.3g and Figure 4.3h show the secondary electron current with a LUMO level onset indicated as well as the hole direct current with an onset corresponding to HOMO, respectively.

Although the correlation between the current onsets and the different molecular levels is visually clear, the derivative of the I_C current with respect to voltage V permits obtaining more quantitative values. In case that

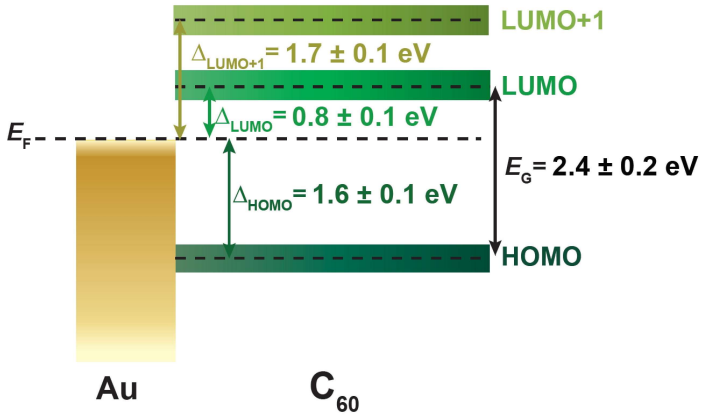

Figure 4.4| Au/C_{60} interface energy diagram. E_F is the Fermi energy and Φ_{Au} the work function of gold. LUMO corresponds to the lowest unoccupied molecular orbital, LUMO+1 to the first excited conductive molecular orbitals and HOMO to the highest occupied molecular orbital. E_G is the energy gap between HOMO and LUMO of C_{60}. Δ corresponds to the energy barrier between the Fermi energy of gold and the molecular level devoted to charge transport. The sub label of each Δ is referred to the corresponding molecular orbital.

the strategy of the linear fitting used in chapter 3 wants to be followed, one has to bear in mind that while in the case of a direct process the collector current behaves as $I_C \propto (e|V_{EB}| - \Delta)$ [31, 32], in the case of secondary processes the dependence is cubic $I_C \propto (e|V_{EB}| - \Delta)^3$ [31, 32, 34, 35]. According to the approach that is followed in inorganic semiconductors, secondary charges have an anisotropic distribution which comes reflected as an extra power two in dependence of the I_C with Δ [31, 32, 34, 35]. This strategy is valid for low disorder organic semiconductors such as C_{60}, but in the case of higher disorder molecules, i.e. C_{70}, the onset of the I_C might be delocalized and thus, this approach might be non-accurate. Moreover, and even if the organic semiconductor has a low disorder, the determination of the energy of excited molecular levels, such as LUMO+1, might be difficult by linear extrapolation. Excited states have typically lower energy separation among them and the tale of the density of states, DOS, of a molecular level might be mixed with the DOS of the other. Thus, in order to avoid the cited problems

in this chapter, the relative energies of the molecular levels are obtained from the onsets of the dI_C/dV curves.

In this way, from electron direct process (see Figure 4.3i) we determine a relative energy of 0.8 ± 0.1 V and 1.7 ± 0.1 V for LUMO and LUMO+1, respectively. The direct hole process in Figure 4.3l shows a HOMO level at 1.6 ± 0.1 V. From the secondary hole current in Figure 4.3j, an energy value of 1.6 ± 0.1 V is extracted for HOMO. In Figure 4.3k, which represents the secondary electron current, an onset corresponding to LUMO is detected at 0.9 ± 0.1 V. All these values are consistent irrespectively of the electronic process, which highlights the robustness of the experimental data. At this point we should stress again that this method determines the energy levels of the molecular orbitals relative to the E_F of the base metal. These relative energy levels are determined in transport in device operative conditions and thus, any interface dipole or interaction at the metal/molecular interface is implicitly taken into account. The transport gap of C_{60} in real device operative conditions can be simply calculated taking into account the energetic difference between HOMO and LUMO, which leads to a value of 2.4 ± 0.2 V (see Figure 4.4). This value is obtained without any assumption regarding the nature of the molecular material, and hence the method presented is easily transferred to other systems. In Table 4.2 we compare the value of the energy gap of C_{60} on gold obtained by i-MOS with the values extracted by other spectroscopic methods. We see that the value that we present here is specially in agreement with the one obtained by UV-VIS. The differences in energy values observed by the different techniques come from the physical and technical differences related to each method and that were explained in the introductory paragraph of the chapter.

Figure 4.5 to Figure 4.8 show the bias dependence of the spectroscopy measurements at 200 K. These measurements were performed at this temperature instead of at 300 K, in order to get further stability of the junction and do not break tunnel junctions when passing high voltages and high current through it. Figure 4.5 shows the collector current I_C for negative emitter-base bias $V_{EB} < 0$. Energetic direct electrons are injected with $V_{CB} \geq 0$V into the lowest molecular orbital (LUMO) and first excited conductive molecular level (LUMO+1) of C_{60}. When $V_{CB} = 0$ V a plateau is observed between the LUMO and LUMO +1 (Figure 4.5 a). This gradually vanishes when higher positive V_{CB} is applied to the system (Figure 4.5b-o).

The maximum collector current can be modulated three orders of magnitudes (250 pA to 350 nA) by applying a positive collector voltage up to 3 V. It is important to highlight that the onset of LUMO and LUMO+1 remain constant, which gives strength to the value of the energy barriers extracted with this method. Moreover, the current below the first onset is always zero and leakage free. Applying V_{CB} = - 0.1 V (Figure 4.6b) energetic primary electrons are injected into the lowest molecular orbital (LUMO) and first excited conductive molecular level (LUMO+1). However, when V_{CB} = - 0.2 V, a small direct electron I_C is injected into the LUMO and secondary hole into the HOMO (Figure 4.6c). These holes are created by the inelastic scattering of the incident hot electrons in the gold metal base with cold electrons, the ones below the Fermi level [30]. For lower V_{CB} only secondary holes are injected into HOMO of C_{60} (Figure 4.6d-o). Applying positive emitter-base bias V_{EB} > 0 V holes are injected directly into the device.

Table 4.2| Relative energy of the LUMO, LUMO+1 and HOMO, and transport gap, E_G, of C_{60} extracted by different Au/C_{60} based i-MOS devices.

C_{60} (on Au)	E_G	Reference
PES/IPES	2.1 eV	A. J. Maxwell, *et al.* Phys. Rev. B 49, 10717 (1994) D. Purdie, *et al.* Surf. Sci. 364, 279 (1996)
STM/STS	2.7± 0.4 eV 2.8± 0.1 eV	X. Lu, *et al.* Phys. Rev. B 70, 115418 (2004) I. F. Torrente *et al.* J. Phys. Condens. Matter 20, 184001 (2008)
UV-VIS	2.4–2.6 eV	D. Faiman, *et al. Thin Solid Films* 295, 283 (1997)
DFT	1.7 eV 2.15 eV	X. Lu, *et al.* Phys. Rev. B 70, 115418 (2004) E. L. Shirley, *et al.* Phys. Rev. Lett. 71, 133 (1993)

When instead of electrons holes are emitted into the device by applying positive V_{EB} but also a $V_{CB} \geq 0$ is applied between collector and base (Figure 4.7) energetic secondary electrons are injected into the lowest molecular orbital (LUMO). The secondary energetic electron I_C comes from a similar effect to Auger scattering in which incident energetic holes excite secondary electron-hole pairs in the gold metal base and thus hot electrons are created

[31–33]. With such V_{CB}, the built-in potential of the organic semiconductor, hinders the injection of primary holes into the semiconductor but instead, enables the injection of secondary holes. Nevertheless, a contribution from hole I_C is observed for V_{CB} = 0 and 0.1 V (Figure 4.7a, b). The hole current totally vanishes when contributing to electron transport by enhancing the built-in potential with $V_{CB} \geq 0.2$ V (Figure 4.7 c-p). Applying a negative V_{CB} between the collector and base, the built-in potential of the C_{60} is cancelled and leads to the tilting of the molecular levels which makes favorable hole transport through it. As it can be observed in Figure 4.8, the effect of V_{CB} is progressive. When V_{CB} = - 0.1 V, secondary electrons still enter in the system reveling the energetic position of LUMO of C_{60} but at V_{EB} = 1.5 V, the signal of I_C inverses due to the major detection of primary holes. At V_{EB} = 1.8 V a kink is observed in the I_C. Even if the origin of this kink is unclear, a possible explanation might come from the competition of direct hole current/secondary electron current detection (Figure 4.8a). When the absolute value of V_{CB} is higher, electron current is no longer preferential compared to the hole current and thus, the onset corresponding to LUMO is no longer detected. The kink in the hole current at V_{EB} = 1.8 V is also gradually vanished until is no longer visible. This reinforces the idea about the origin of the kink that has been discussed above (Figure 4.8b-p).

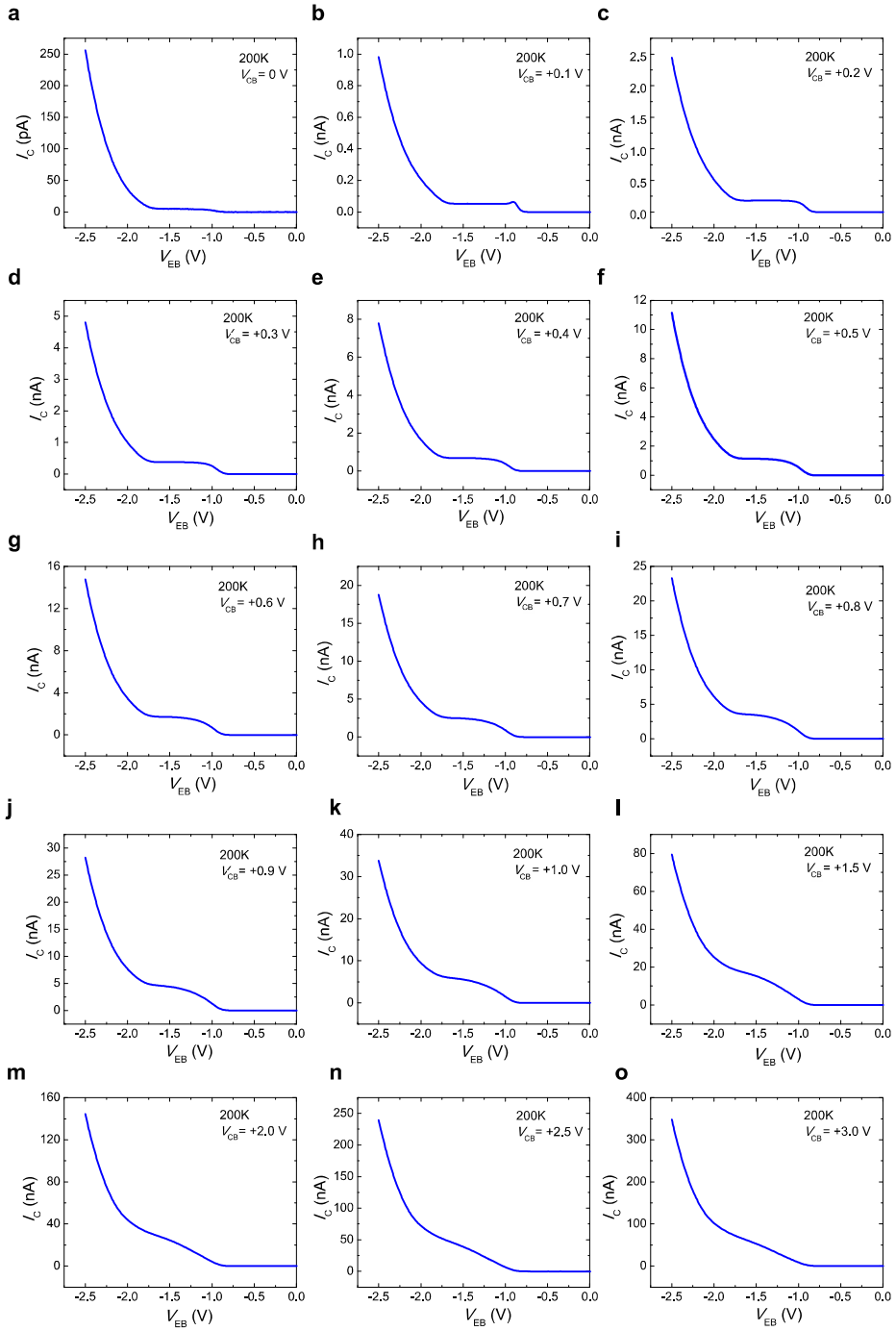

Figure 4.5| Collector current I_C for negative emitter-base bias $V_{EB} < 0$ V at 200 K in a Au/C_{60} based i-MOS. Energetic direct electrons are injected with $V_{CB} \geq 0$V

into the lowest molecular orbital (LUMO) and first excited conductive molecular level (LUMO+1) of C_{60}. The lowering of the current observed between LUMO and LUMO+1 when no external V_{BC} bias is applied (**a**), gradually vanishes when higher positive V_{CB} is applied to the system (**b**-**p**).

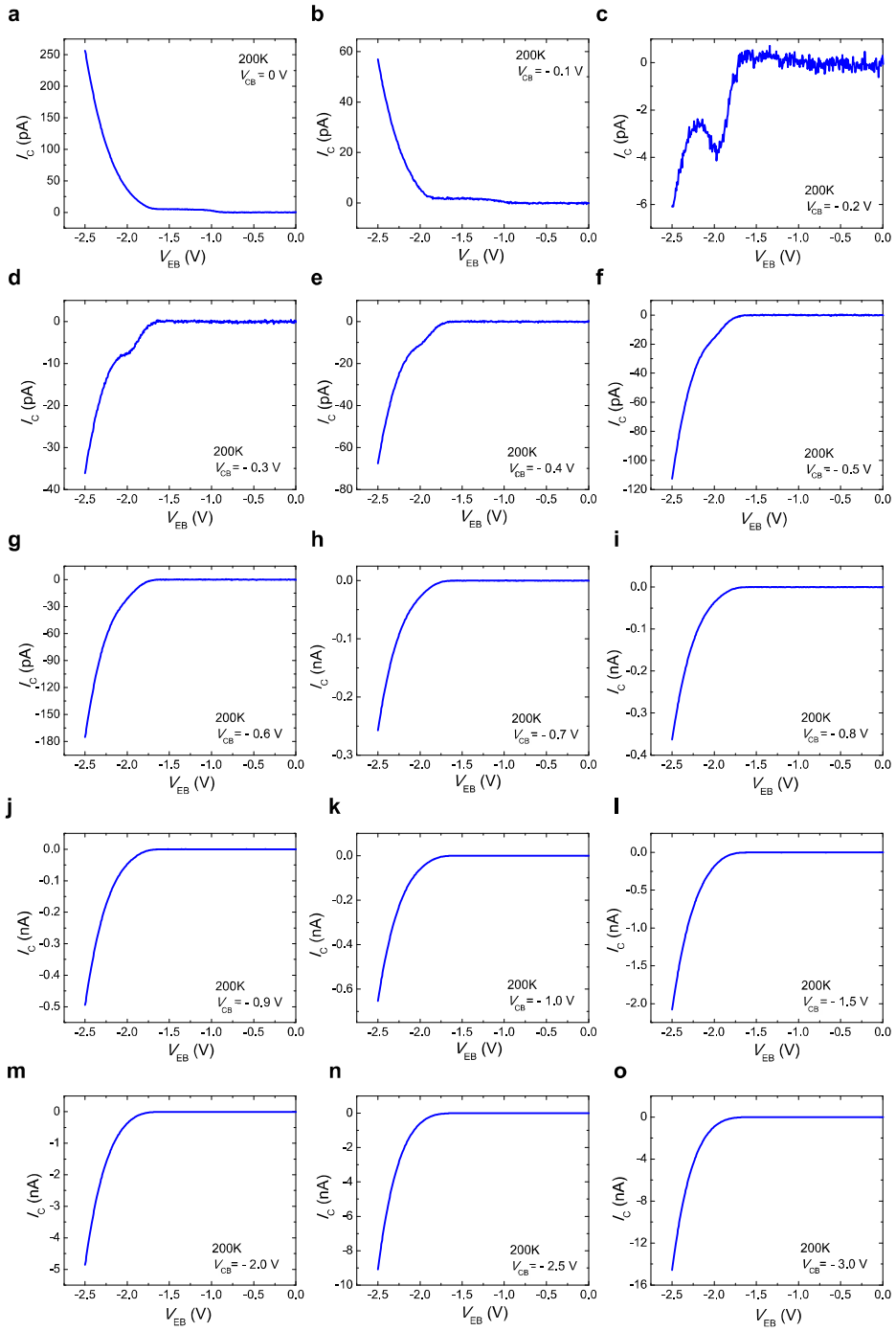

Figure 4.6| Collector current I_C for negative emitter-base bias V_{EB} < 0 V at 200 K in a Au/C_{60} based i-MOS device. Energetic primary electrons are injected when

V_{CB} = 0 V and V_{CB} = - 0.1 V into the lowest molecular orbital (LUMO) and first excited conductive molecular level (LUMO+1) (**a**, **b**). When V_{CB} = - 0.2 V, a small direct electron I_C is injected into the LUMO and secondary hole into the HOMO (**c**). These holes come from the inelastic scattering of the incident hot electrons in the gold metal base with cold electrons (below the Fermi level) [30]. For lower V_{CB} only secondary holes are injected into HOMO of C_{60} (**d**-**p**).

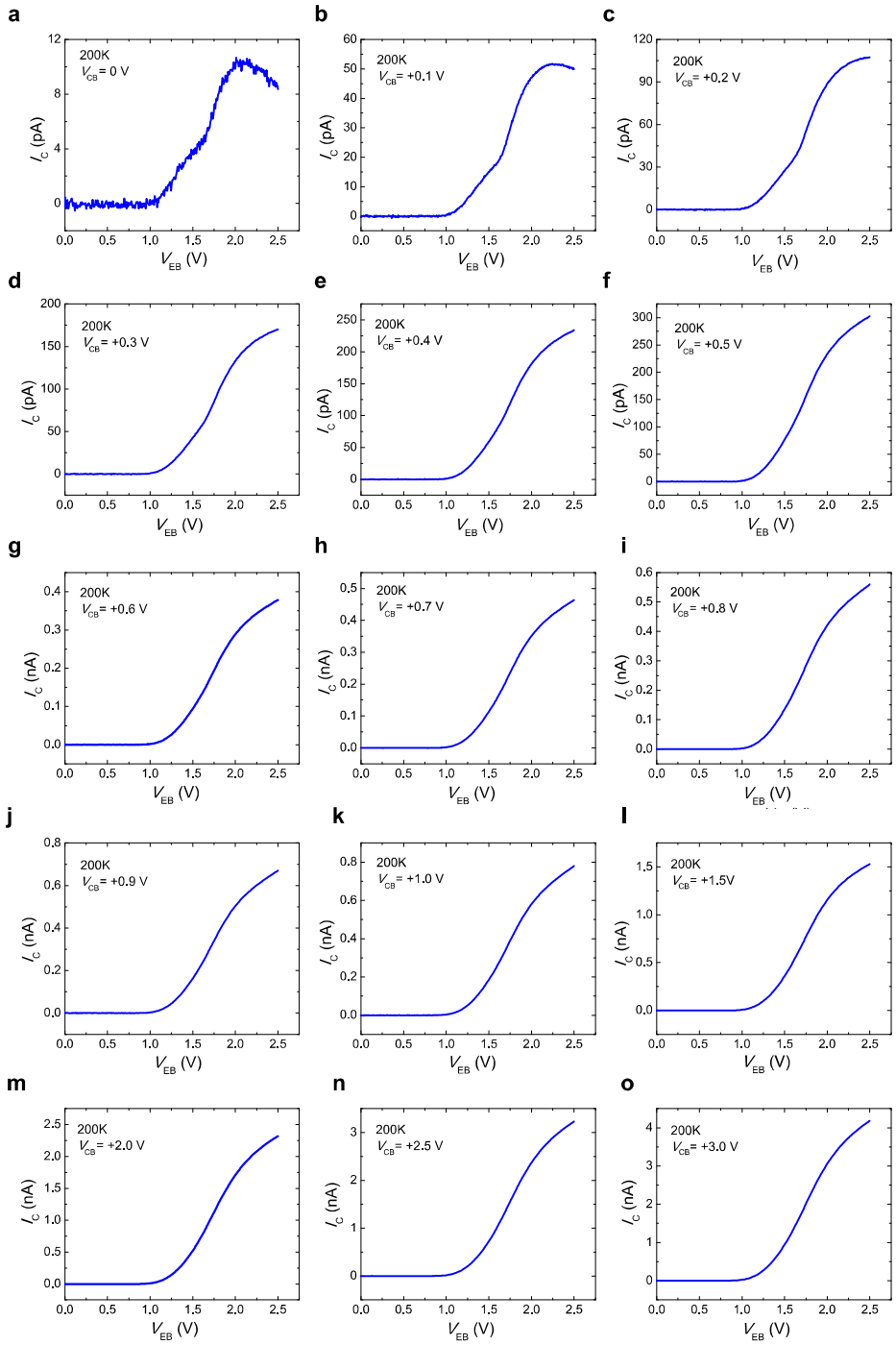

Figure 4.7| Collector current I_C for positive emitter-base bias V_{EB} > 0 V at 200 K in a Au/C_{60} based i-MOS device. Energetic secondary electrons are injected into

the lowest molecular orbital (LUMO) when $V_{CB} \geq 0$ V (**a**-**p**). The secondary energetic electron I_C comes from a similar effect to Auger scattering in which incident energetic holes excite secondary electron-hole pairs in the gold metal base and thus hot electrons are created [31–33]. A contribution from hole I_C is observed for the lowest V_{CB}.

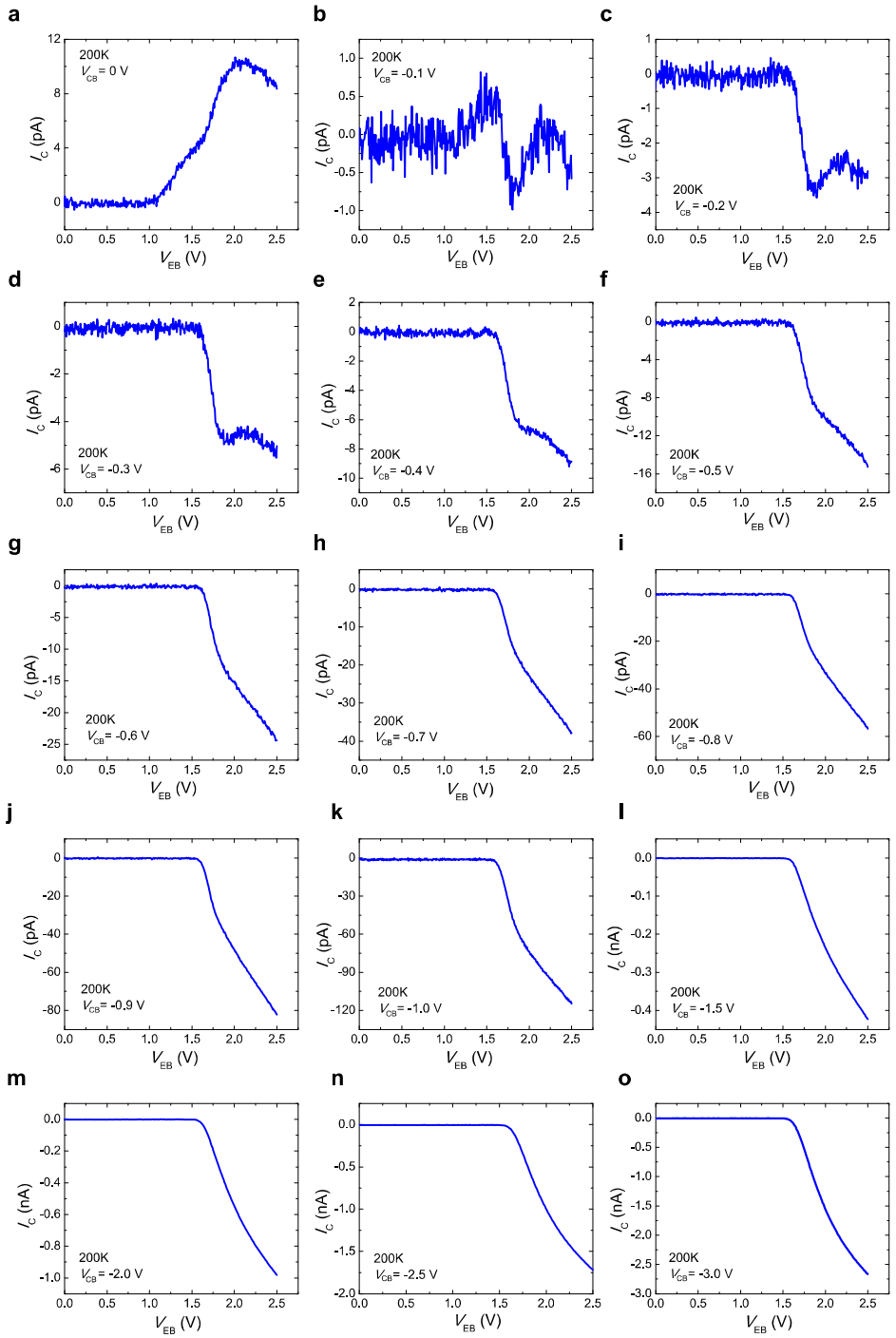

Figure 4.8| Collector current I_C for positive emitter-base bias $V_{EB} > 0$ V at 200 K

in a Au/C60 based i-MOS. When no V_{CB} is applied secondary electron current coming from an effect similar to Auger scattering is observed (**a**). However, when V_{CB} < 0V energetic direct holes are injected leading to the observation of HOMO (**b-p**).

Summarizing, in this section we have been able to perform a complete study of the energies of the molecular levels of C_{60} relative to the Fermi level of the gold by i-MOS. We determine that LUMO level is at 0.8 ± 0.1 V, LUMO +1 level at 1.7 ± 0.1 V and HOMO level at 1.6 ± 0.1 V with respect to the E_F of gold. We also determine that the transport energy gap of C_{60} is 2.4 ± 0.2 V. All this work is complemented with a detailed study of the effect of the V_{CB} in the charge injection and diffusion through the molecular layer.

4.2.2 C_{70} based i-MOS

In this section we determine the relative energy of the molecular levels of C_{70} with respect to the E_F of gold, as well as the associated transport gap of the semiconductor. Following the same strategy as with C_{60}, we first discuss the current-voltage (*I-V*) characteristics of C_{70} based i-MOS device counterparts and then we perform the spectroscopic measurements.

Figure 4.9a shows the emitter-base current I_E flowing through the tunnel junction when the voltage V_{EB} is swept between the emitter and the base from 300 K to 6 K. Non-linear *I-V* trace, with slight increase in resistance when lowering the temperature, confirms the behaviour of a continuous tunnel junction [23,24].

Figure 4.9b shows the current I_{diode} at 300 K of the Au/C_{70}/Al stack when the voltage V_{CB} is swept. A highly non-linear *I-V* curve is observed, with close to zero current at negative V_{CB} and up to 200 nA at positive V_{CB}. This asymmetry is also visible in logarithmic scale in Figure 4.9c. The very low current at negative V_{CB} suggests the formation of an energy barrier for electrons at Al/C_{70} interface, which should be higher than the one at Au/C_{70} interface. This is a surprising result considering the similar molecular level energies of C_{60} and C_{70} and the a priori ohmic contact between E_F of aluminium and LUMO of the molecule. A possible reason for having an energy barrier at Al/C_{70} interface might come from the hybridization of the molecular layer with aluminium. Aluminium is a quite reactive material and C_{70} is known to be more reactive than C_{60}. Besides this, a higher charge

transmission coefficient of Au/C_{70} interface than the one of Au/C_{60} and the higher density of the bigger fullerene might be the causes behind the higher current injection from the base electrode that is observed in this case compared to the C_{60} sample measurements (Figure 4.2b). Nevertheless, the decreasing of the temperature breaks the asymmetry of the curve and similar I_{diode}-V_{EB} curves are measured from both current-injecting sides. Figure 4.9d shows I_{diode} at 260 K in logarithmic scale. Comparing Figure 4.9c and Figure 4.9d, a considerable decrease in the total I_{diode} current is observed.

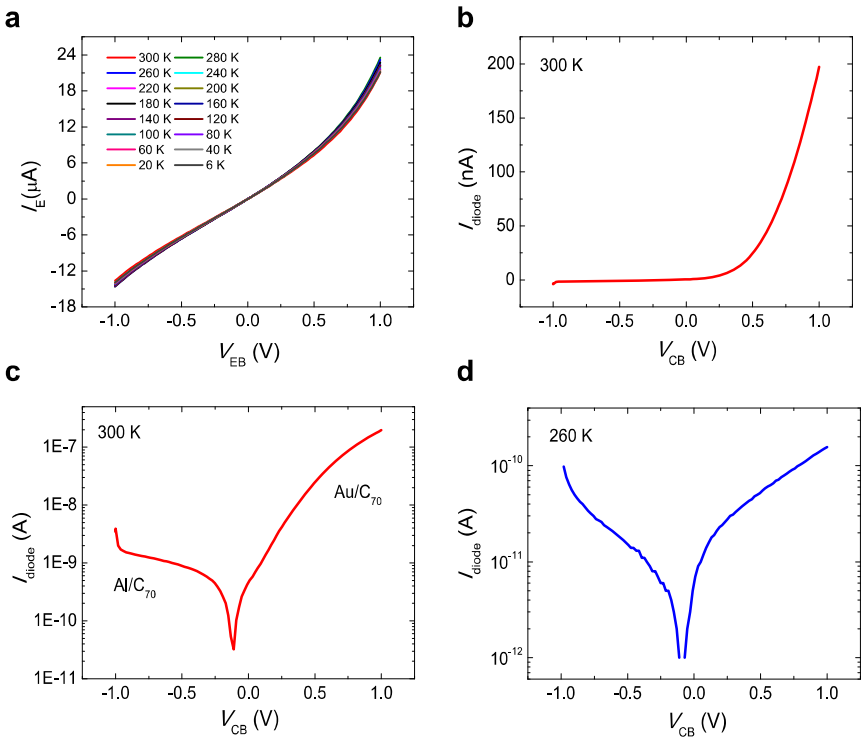

Figure 4.9| Electrical characterization of tunnel junction and diode. a, Current I_E measured at two terminals in the Al/Al_2O_3/Au tunnel junction as function of the applied bias between emitter and base, V_{EB}, for 300 K- 6 K temperature range. **b**, Current I_{diode} measured at two terminals in the Au/C_{70}/Al stack as function of the applied bias between the base and the collector V_{CB} at 300 K. **c**, Current I_{diode} in logarithmic scale as function of V_{CB} at 300 K. **d**, I_{diode} – V_{CB} at 260 K.

Once having tested separately the tunnel junction and the diode of the device, we prove the spectroscopic functionality of the C_{70} device. Figure 4.10 shows the working principles of i-MOS together with the measured current in the collector I_C for different emitter-base voltage biases, V_{EB}. The working principle is the same as explained for the C_{60} based i-MOS (Figure 4.10 a-d). Figure 1.10e shows the I_C versus negative V_{EB} with V_{CB} = 0.5 V for direct electron processes. Two onsets corresponding to LUMO and LUMO+1 are detected. All the measurements in Figure 4.10 are performed at 200 K to get more stability and take lower risk of breaking the device. However, as we will show later the device operates at room temperature and thus, it is possible to perform these measurements at 300 K. Under a negative applied electric field through the organic semiconductor, V_{CB} = 0.5 V, secondary holes coming from inelastic scattering of hot electrons with cold electrons enter into the HOMO level of C_{70} (see Figure 4.10f) Analogously, for positive V_{EB} instead of electrons, holes are injected from emitter to the base. Direct holes enter into the HOMO of the semiconductor when a negative V_{CB} is applied (Figure 4.10g). Under positive V_{CB}, secondary holes coming from an Auger-like scattering access to the LUMO level (see Figure 4.10h).

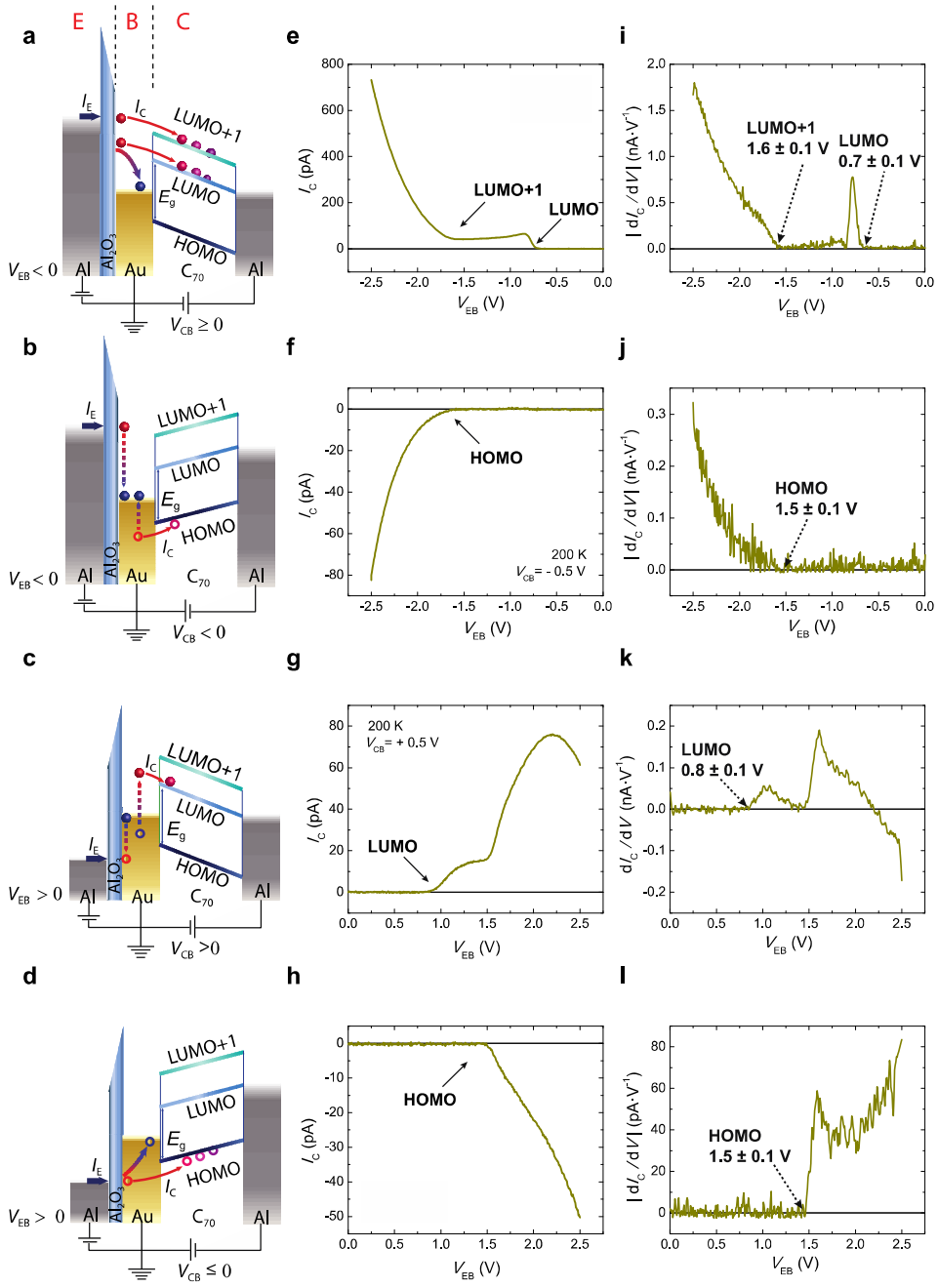

Figure 4.10| In-device molecular spectroscopy (i-MOS) operation under different emitter-base bias V_{EB} polarities at room temperature. a, Schematic representation of the direct process in which electrons are injected by applying a

negative emitter-base bias, $V_{EB} < 0$ V, and detected in the molecular semiconductor. The measurements can be performed either without any externally applied collector-base bias, V_{CB}, or by $V_{CB} \geq 0$ V. **b**, Schematic representation of the secondary process at i-MOS when electrons are injected, $V_{EB} < 0$ V, into the device but holes are detected. $V_{CB} < 0$V is required in order to cancel the built-in potential and help hole injection into and transport through the organic semiconductor. **c**, Schematic representation of the secondary process at i-MOS when holes are injected into the device, $V_{EB} > 0$ V, but hot electrons coming from a similar effect to Auger scattering are detected with $V_{CB} > 0$V. **d**, Schematic representation of the direct process at i-MOS when holes are injected, $V_{EB} > 0$ V, and detected with $V_{CB} \leq 0$V. **e**, Collector current I_C for $V_{EB} < 0$ V at 200 K. Energetic electrons are injected with $V_{CB} = 0.5$ V both into the lowest molecular orbital (LUMO) and into the first excited conductive molecular level (LUMO+1) states of C_{70}. Notice that in the current configuration, positive I_C indicates electron current detection whereas negative I_C corresponds to hole current detection in C_{70}. **f**, Detected I_C for $V_{EB} < 0$ V and $V_{CB} = -0.5$ V at 200 K. Injection of a hole current into C_{70} leads to the detection of its highest occupied molecular orbital (HOMO) states. **g**, Electron current, I_C, and LUMO states detected with $V_{EB} > 0$ V and $V_{CB} = 0.5$ V at 200 K. **h**, I_C versus V_{EB} when $V_{EB} > 0$ V and $V_{CB} = -0.5$ V. Injection of energetic holes permits the detection of the HOMO states of C_{70} in a direct process. **i,** Derivative of the I_C respect to V_{EB} for $V_{EB} < 0$ V at $V_{CB} = 0.5$ V for the extraction of the energy of LUMO and LUMO+1 of C_{70} at 0.7 ± 0.1 eV and 1.6 ± 0.1 eV, respectively. **j**, Derivative of the I_C respect to V_{EB} when $V_{EB} < 0$ V at $V_{CB} = -0.5$ V. An energy value of 1.5 ± 0.1 eV is extracted for the relative position of HOMO of C_{70}. **k**, Relative energy of LUMO of C_{70} at 0.8 ± 0.1 eV by doing the derivative of the I_C respect to V_{EB} when $V_{EB} > 0$ V at $V_{CB} = 0.5$ V V. **l,** Derivative of the I_C respect to V_{EB} when for $V_{EB} > 0$ V and $V_{CB} = -0.5$ V. 1.5 ± 0.1 eV is extracted as the relative position of HOMO of C_{70}.

If we plot the derivative of I_C with respect to V for all processes, we can determine the energy of the molecular levels of C_{70} relative to the E_F of gold base. Figure 4.10i shows dI_C/dV versus V_{EB} for direct electron processes and from here, 0.7 ± 0.1 V and 1.6 ± 0.1 V are determined as LUMO and LUMO+1 of C_{70}, respectively. The direct hole current in Figure 4.10l shows the HOMO level at 1.5 ± 0.1 V. From the secondary hole current in Figure 4.10j, an energy value of 1.5 ± 0.1 V is extracted for HOMO. In Figure 4.10k, which represents the secondary electron current, an onset corresponding to LUMO is detected at 0.8 ± 0.1 V. All these energy values are summarized in Figure 4.11, where the transport gap of C_{70} is also highlighted. We remind that the

transport gap of the molecular semiconductor is the energy difference of HOMO and LUMO extracted at device operative condition by i-MOS. This leads to C_{70} a transport gap of 2.2 ± 0.2 eV.

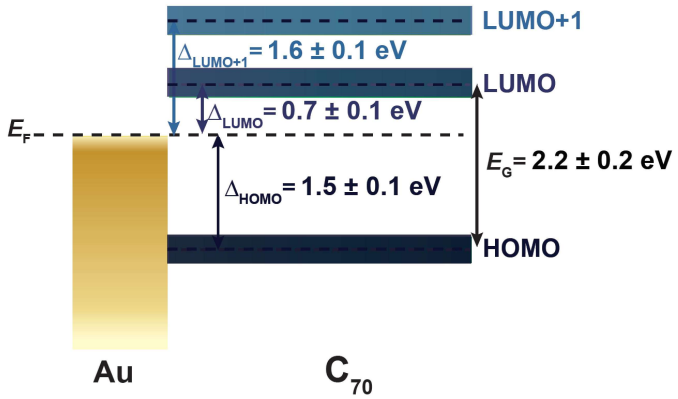

Figure 4.11| Energy diagram of Au/C_{70} interface. E_F is the Fermi energy and Φ_{Au} the work function of gold. LUMO corresponds to the lowest unoccupied molecular orbital, LUMO+1 to the first excited conductive molecular orbitals respectively, and HOMO to the highest occupied molecular orbital. E_G is the energy gap between HOMO and LUMO of C_{70}. Δ corresponds to the energy barrier between the Fermi energy of gold and the molecular level devoted to charge transport. The sub label of each Δ is referred to the corresponding molecular orbital.

From Figure 4.12 to Figure 4.15 the bias dependence of the four quadrants spectroscopy measurements at 200 K are shown. Figure 4.12 shows the collector current I_C for negative emitter-base bias $V_{EB} < 0$. Energetic direct electrons are injected with $V_{CB} \geq 0$V into the lowest molecular orbital (LUMO) and first excited conductive molecular level (LUMO+1) of C_{60}. When $V_{CB} = 0$ V a decrease in I_C is observed between the LUMO and LUMO +1 (Figure 4.12a). We will further discus the origin of these peak in the following section. When higher positive V_{CB} is applied to the system, the peak gradually vanishes until it becomes a plateau (Figure 4.12b-f). For even higher V_{CB}, the plateau disappears (Figure 4.12f-i). The maximum collector current can be modulated five orders of magnitudes (8 pA to 150 nA) by applying a positive collector voltage up to 3 V. We highlight that the onset of LUMO and LUMO+1 remain constant, which indicates that the energy values extracted by i-MOS are robust. Moreover, the current below

the first onset is always zero and leakage free. In the moment that a small negative V_{CB} bias is applied secondary holes enter into HOMO level of C_{70} (Figure 4.13b-i). These holes are created by the inelastic scattering of the incident hot electrons in the gold metal base with cold electrons [30]. The hole current increases with the nominal value of V_{CB}.

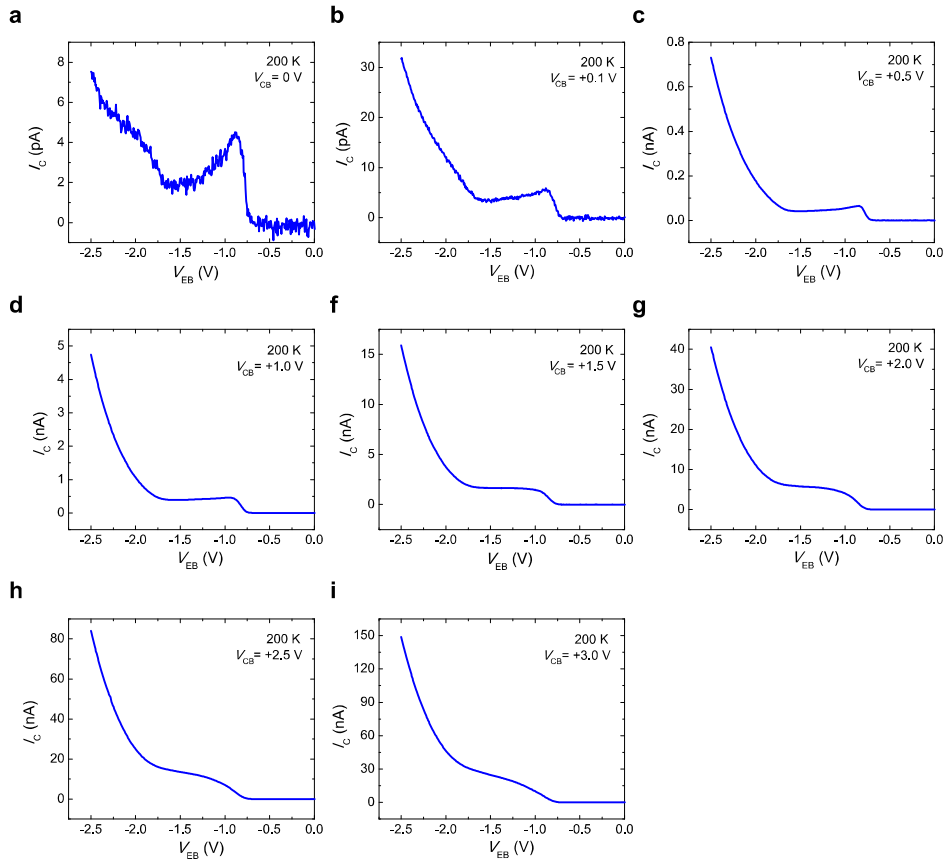

Figure 4.12| Collector current I_C for negative emitter-base bias VEB < 0 V and VCB > 0 V at 200 K in a Au/C70 based i-MOS. Energetic direct electrons are injected with VCB ≥ 0V into the lowest molecular orbital (LUMO) and first excited conductive molecular level (LUMO+1) of C70. The lowering of the current observed between LUMO and LUMO+1 when no external VCB bias is applied (**a**), gradually vanishes when higher positive VCB is applied to the system (**b**-**i**). Interestingly the onset of LUMO and LUMO+1 remain consistent. Moreover, the current below the first onset is always zero and leakage free.

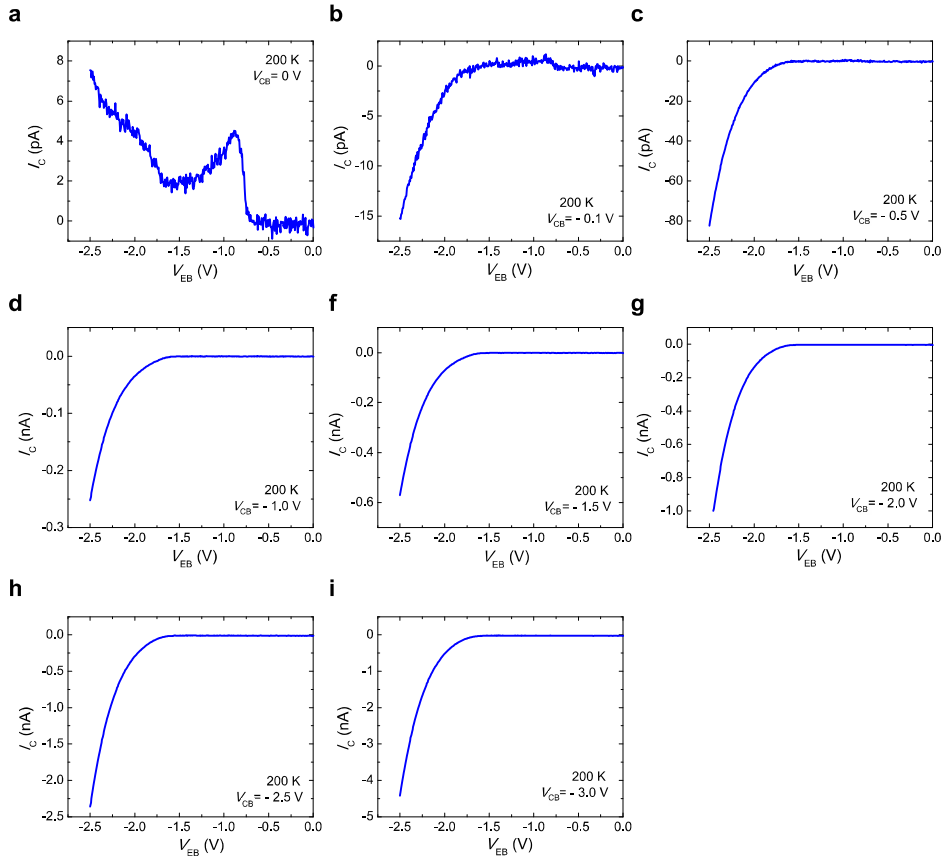

Figure 4.13| Collector current I_C for negative emitter-base bias VEB < 0 V and VCB < 0 V at 200 K in a Au/C70 based i-MOS device. Energetic primary electrons are injected when VCB = 0 V into the lowest molecular orbital (LUMO) and first excited conductive molecular level (LUMO+1) (**a**). When VCB > 0 V (**b**-**i**), a secondary hole current is injected into the HOMO (**c**). These holes are created by the inelastic scattering of the incident hot electrons in the gold metal base with cold electrons (below the Fermi level).

Figure 4.14 and Figure 4.15 show I_C current for positive emitter-base bias. When $V_{CB} \leq 0$ (Figure 4.15) energetic primary holes are injected into the HOMO of C_{70}. Direct holes are still collected when positive V_{CB} ranges from $0 \leq V_{CB} \leq 0.2$ V (Figure 4.14a-c). Nevertheless, the hole current is lowered when increasing the V_{CB}, while secondary electron current that enters in the LUMO level of C_{70} starts to be more pronounced in the $I_C - V_{EB}$ curves. These secondary energetic electron I_C comes from a similar effect to Auger

scattering in which incident energetic holes excite secondary electron-hole pairs in the gold metal base and thus, hot electrons are created [31–33]. When $0.3\ \text{V} \leq V_{\text{CB}} \leq 0.5\ \text{V}$, even if no direct hole current is measured, a contribution coming from this is observed at $V_{\text{EB}} > 2.0$ V (Figure 4.14d-f). For $V_{\text{CB}} > 0.5$ V no more contribution from hole current is detected (Figure 4.14g-k).

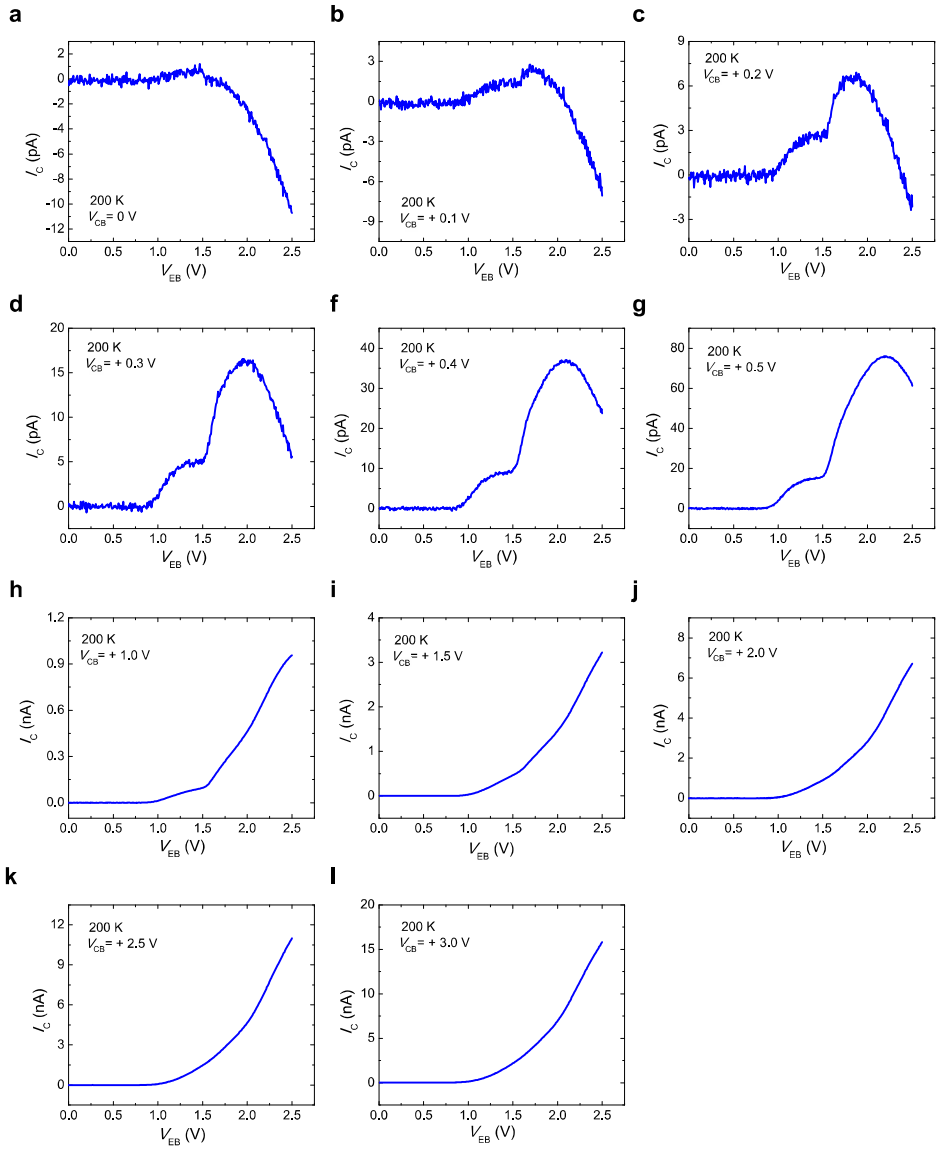

Figure 4.14| Collector current I_C for positive emitter-base bias $V_{EB} > 0$ V and

***V_{CB}* > 0 V at 200 K in a Au/C_{70} based i-MOS device.** Energetic hole current is injected when $0 \leq V_{CB} \leq 0.2$ V into the highest molecular orbital (HOMO) (**a**-**c**). When $V_{CB} \geq 0.3$ V secondary energetic electron I_C is injected leading to the detection of LUMO (**d**-**l**). These secondary electrons come from a similar effect to Auger scattering in which incident energetic holes excite secondary electron-hole pairs in the gold and thus hot electrons are created. A contribution from hole I_C might be observed in figures **d**-**g**.

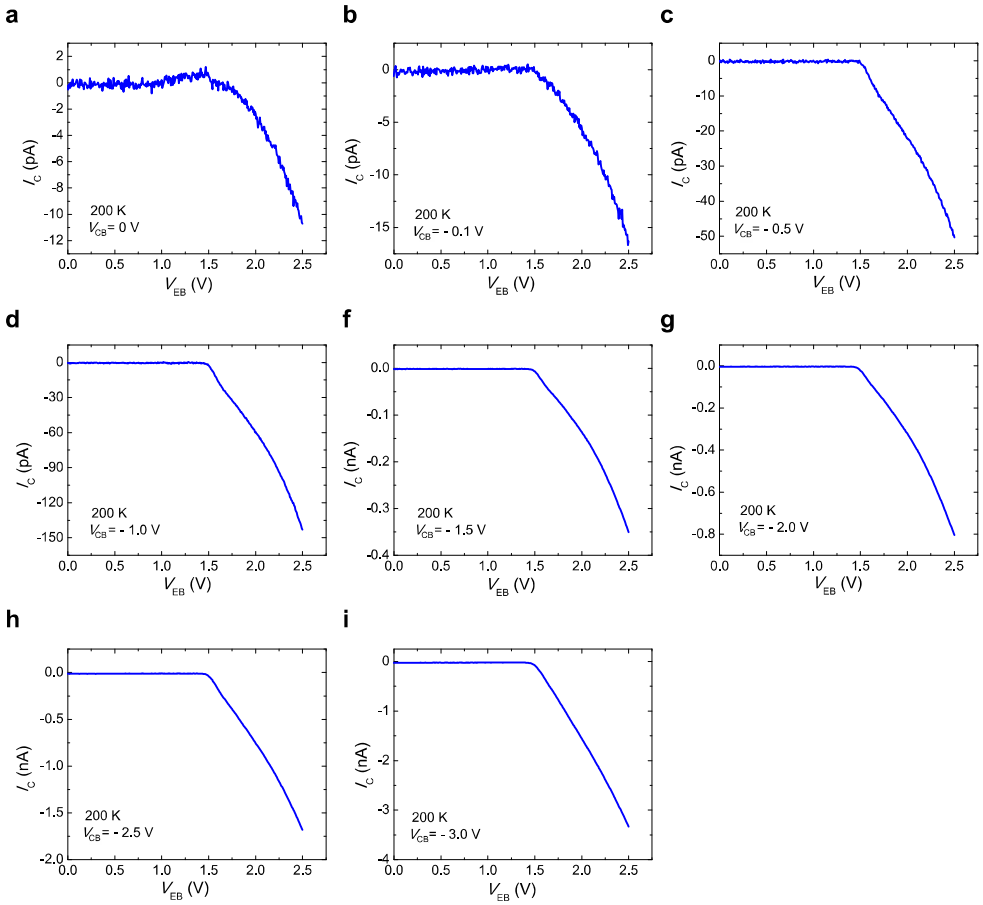

Figure 4.15| Collector current *I_C* for positive emitter-base bias *V_{EB}* > 0 V and *V*CB < 0 V at 200 K in a Au/C_{70} based i-MOS. When $V_{CB} \leq 0$V energetic direct holes are injected into the semiconductor leading to the observation of HOMO (**b**-**o**).

In this section of the chapter we were able to access the LUMO, LUMO+1 and HOMO levels of C_{70} and determine that the levels are at 0.7± 0.1 V, 1.6 ± 0.1

V and 1.5 ± 0.1 V, respectively, from the E_F of gold base contact. We also resolve the transport energy gap of C_{70}, which is 2.2 ± 0.2 V. This study of the C_{70} proves that i-MOS has sufficient resolution to detect energy differences between different molecules.

4.3 Marcus Inversion Region

In this section we focus on the direct electron processes and we perform temperature dependence measurements to study charge transport effects at the Au/C_{60} and Au/C_{70} interfaces.

4.3.1 C_{60} based device

The temperature dependence of i-MOS allows the exploration of the charge transport at metal/molecular interfaces. Figure 4.16 shows the temperature dependence of I_C with V_{EB} < 0 V at V_{CB} = 0 V for the electron-injection/electron-detection process from 300 K to 120 K. In the range of 300 K to 260 K (Figure 4.16a-c), a continuous increase of I_C is observed between the LUMO and LUMO+1 levels of C_{60}. However, at 240 K a plateau appears between LUMO and LUMO+1 (Figure 4.16d). At temperatures below 180 K, an effective negative differential resistance (NDR) is observed between LUMO and LUMO+1 (Figure 4.16d-j). NDR is the property of some devices in which the increase of the voltage results in the decrease of the electric current that flows through it [36]. This effect was first discovered in 1958 by L. Esaki in a heavily doped semiconducting germanium p-n junction[36]. He understood that the negative differential resistance was coming from the tunnelling of electrons and this was the first experimental evidence of quantum mechanical tunnelling transport. Here, we specify effective because we perform the measurements with three terminals while NDR is typically measured with two in a diode-like device structures [37–40]. This is a truly unconventional behaviour: in a simple picture the current should always increase with the voltage since we are collecting all the hot electrons injected into the molecular material.

In Figure 4.16k we plot the maximum change in the I_C with temperature where effective negative differential resistance NDR is observed. Curves were normalized, and the derivative calculated yielding the minimum point

of the effective NDR. This minimum is represented for temperature from 300 K to 120 K with V_{CB}= 0 V. We observe in this figure that the NDR starts appearing at 260 K, before what one can observe by eye, and that the effect is dramatically enhanced with the lowering of the temperature. In Figure 4.17a, all the I_C curves with V_{EB} < 0 V at V_{CB} = 0 V from 300 K to 120 K are plotted together in logarithmic scale.

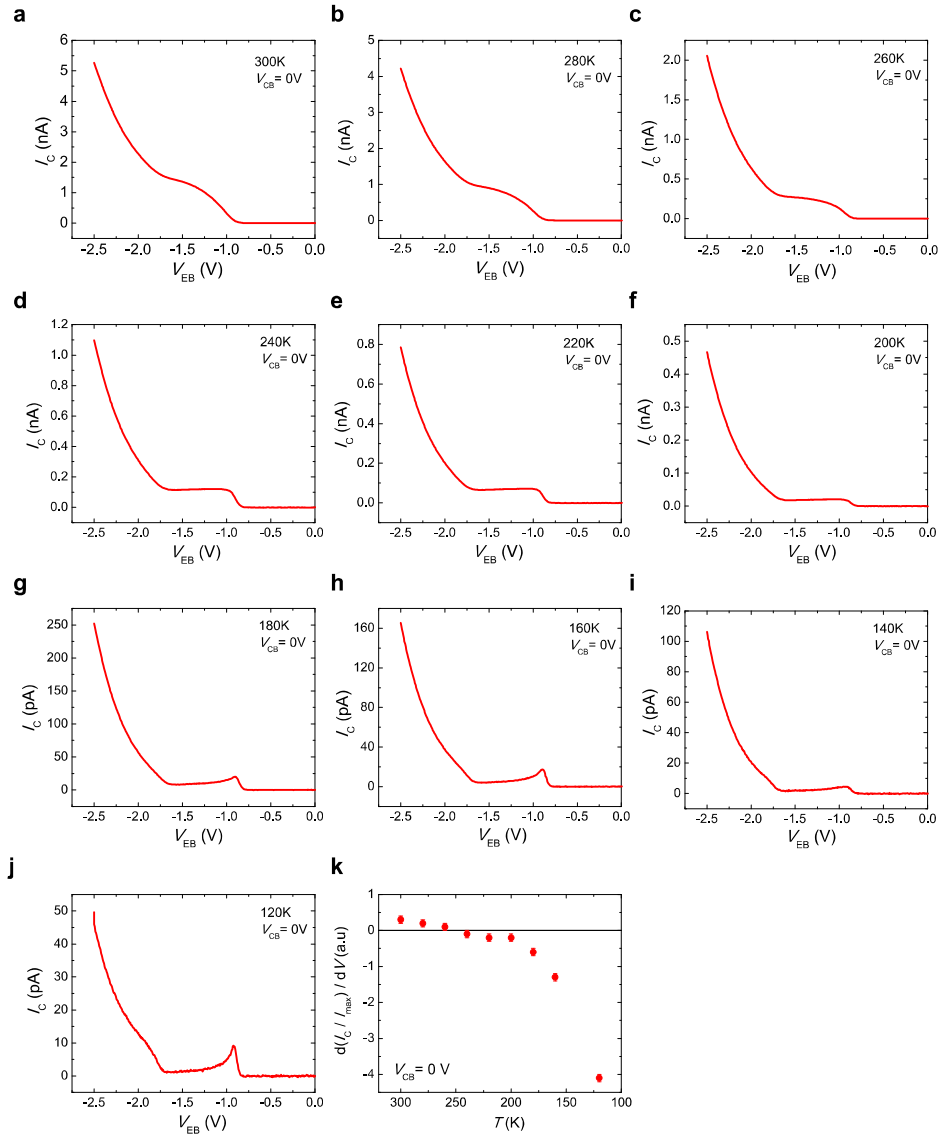

Figure 4.16| Temperature dependence of collector current I_C for negative emitter-base bias V_{EB}< 0 V in a Au/C_{60} i-MOS. Collector current I_C for negative

emitter-base bias V_{EB} < 0 V at temperatures from 300 K to 120 K for in-device molecular spectroscopy (i-MOS) with Au/C_{60} interface. Energetic electrons are injected and detected with V_{CB} = 0V into the lowest molecular orbital (LUMO) and first excited conductive molecular level (LUMO+1) of C_{60}. The increase of I_C between LUMO and LUMO+1 at high temperatures (**a**-**c**) converges into a plateau at 240 K (**d**-**f**). At lower temperatures, below 200 K, a decrease in the I_C is observed between LUMO and LUMO+1 (**g**-**j**). Figure **k** corresponds to the maximum change in the I_C with temperature where effective negative differential resistance NDR is observed. Curves were normalized, and the derivative calculated yielding the minimum point of the effective NDR. This minimum is represented for temperature from 300 K to 120 K with V_{CB}= 0 V.

In order to rationalize this intriguing regime, a comprehensive simulation framework developed by the group of F. Ortmann from TU Dresden allows us to obtain the simulated currents (Figure 4.17b) for the same conditions under which the experiments were performed. Charge-transfer is modelled with a Fermi's golden rule expression for the transfer rate, which is known as Marcus hopping rate [41]. At this point, we must emphasize that, in order to achieve any agreement with the experimental results, such an approach is unambiguously required. See Figure 4.17c, where the simulated I_C with and without Marcus rate is plotted. Its role in the conduction at the metal/molecular interfaces can be observed in Figure 4.17d. The electronic energy of a neutral C_{60} (to whom the hot electrons have not yet reached) is shown on the left as black parabolas, which are vertically offset by different V_{EB} (which correspond to the initial electron energy). The parabolic shape indicates the dependence of the energy on the deformation along a molecular conformation coordinate, q. The analogous dependence for the negatively charged $\mathbf{C_{60}^-}$ (in its final configuration, having received an electron) is shown in red. The crossing points between the parabolas define the transition energy for the charge transfer, which in i-MOS it can be controlled by the emitter-base voltage. This knob allows an increase of the driving force for electron transfer by tuning V_{EB} around the LUMO position. As an example, two cases are indicated with transition states E_T and E_T' which are activated from initial states E_I and E_I', respectively. The activation energy is defined in general as the difference between the transition and the initial energies such as E_A=|E_T-E_I|. At low voltages ($-\boldsymbol{V_{EB}} < \boldsymbol{V_0}$), exemplified in the transition from E_I to E_T, an increase of the voltage results in a lower

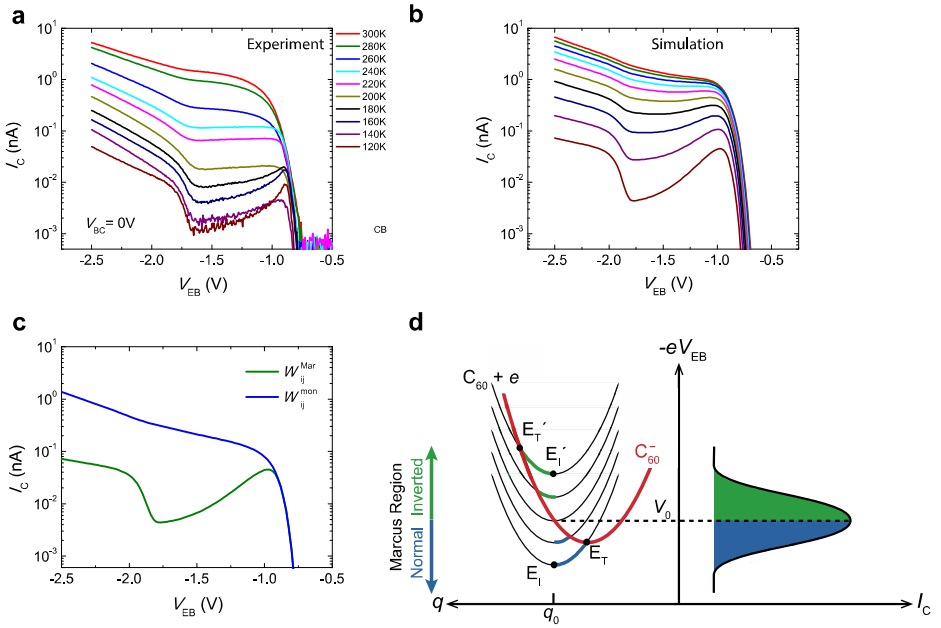

Figure 4.17| Temperature dependence of the hot-electron current for the direct electron process and appearance of a negative differential resistance regime. a, Temperature dependence of the direct hot-electron current I_C for negative emitter-base bias V_{EB}<0, and without any applied collector-base bias, V_{CB}=0 V. **b**, Simulated I_C under the same conditions as in panel a. **c**, Comparison of simulations with Marcus rate, $\boldsymbol{W_{ij}^{Mar}}$, (green solid line) and no Marcus rate, $\boldsymbol{W_{ij}^{mon}}$, (blue solid line) regarding the direct hot-electron current $\boldsymbol{I_C}$ for vanishing base-collector bias V_{CB} = 0 and low temperature T = 120 K as a function of negative emitter-base bias V_{EB}. The Marcus Inverted Regime observed in the experiment can only be modelled using the Marcus rate. **d**, Illustration of the charge transfer in both the Marcus Normal and Inverted Regions. Black parabolas correspond to the electronic energy of a neutral C_{60}. The parabolic shape indicates the dependence of the energy on the deformation along a molecular conformation coordinate, q. The analogous dependence for the negatively charged $\boldsymbol{C_{60}^-}$ is shown in red. The crossing points between the parabolas define the transition energy for the charge transfer. The blue shaded area corresponds to Marcus Normal Region, while the green shaded area represents the Marcus Inverted Region.

activation energy (left), which leads to an increase of the current (blue shaded area on the right). This behaviour is known as the Marcus Normal

Region. However, the non-monotonous dependence of the activation energy on V_{EB} establishes another regime, which is the so-called Marcus Inverted Region (MIR) (green shaded area). This regime is characterized by the reduction of the current due to the increment of the barrier despite of a continuous hike of the driving force (larger E_I). At the voltage $-V_{EB}=V_0$ (at which $E_I=E_T$), the activation energy vanishes and a crossover between the normal and inverted Marcus regions occurs. For an even larger driving force, exemplified now in the transition from E_I' to E_T', the current decreases (green shaded area on the right) due to the increased barrier. The two regimes can be observed both in the experimental data and in the corresponding simulations shown in Figure 4.17. The simulations can also explain the reduction of the NDR regime in the hot-electron current measurements at high temperatures (Figure 4.17a) taking into account the increase of the inelastic scattering in the base with temperature (see Figure 4.17b).

The observation of this energy crossover by analysing reactions in solution chemistry marked the breakthrough of Marcus theory [42]. In the present case, we are able to directly access and manipulate this eluding transport regime in a molecular solid-state device. Our observation of the Marcus Inverted Region was possible for several underlying physical reasons. In the first place, we must recall that we inject electrons with high energies, which allow us to explore a transport regime beyond the one mapped with devices operating close to the Fermi level, such as conventional organic field effect transistors. In the second place, LUMO and LUMO+1 conductive levels are sufficiently separated and the electron-vibration coupling, which may lead to significant level broadening, is not too large. Moreover, our model system Au/C_{60} represents a weakly interacting interface with relatively low interfacial disorder, which leads to the appropriate energy resolution required to observe the effective NDR. Nevertheless, we have been able to reproduce the NDR in Cu/C_{60} based i-MOS device. In Figure 4.18 we show I_C current for negative emitter-base bias $V_{EB} < 0$ V of Cu/C_{60} based i-MOS from 300 K to 120 K. Energetic electrons are injected and detected with $V_{CB} = 0$V into the lowest molecular orbital (LUMO) and first excited conductive molecular level (LUMO+1) of C_{60}. In a similar manner to the Au/C_{60} based i-MOS system, we observe that the increase of I_C between LUMO and LUMO+1 at high temperatures (Figure

4.18a) converges into a plateau at 200 K (Figure 4.18b). At lower temperatures, below 180 K, a decrease in the I_C and thus, effective NDR is observed between LUMO and LUMO+1 (Figure 4.18c-d). Thus, we demonstrate that the effective NDR does not come from the metal contact but from the organic semiconductor. This gives strength to our statement about the observation of the Marcus Inverted Regime.

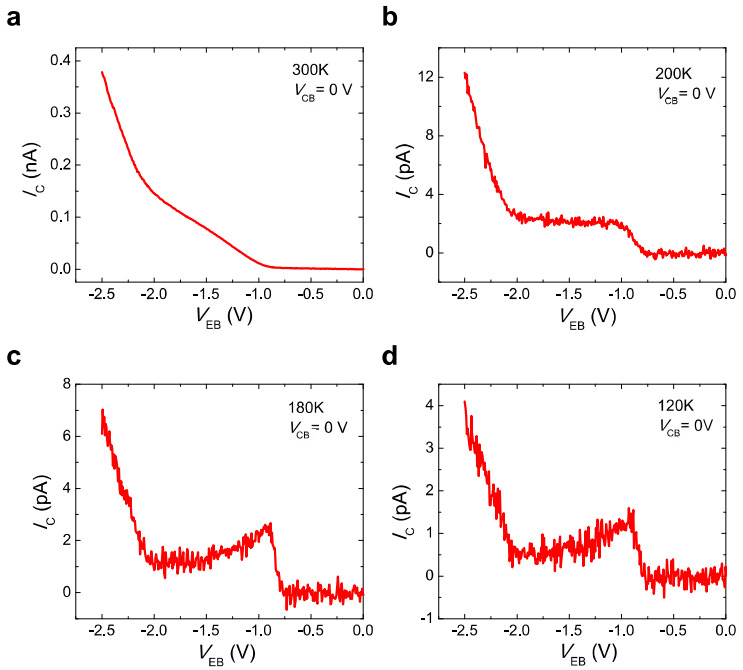

Figure 4.18| Temperature dependence of collector current I_C for negative emitter-base bias V_{EB} < 0 V of Cu/C_{60} based i-MOS. Energetic electrons are injected and detected with V_{CB} = 0V into the lowest molecular orbital (LUMO) and first excited conductive molecular level (LUMO+1) of C_{60}. The increase of I_C between LUMO and LUMO+1 at high temperatures (**a**) is observed to converge into a plateau at 200 K (**b**). At lower temperatures, below 180 K, a decrease in the I_C is observed between LUMO and LUMO+1 (**c**-**d**).

The effective NDR arising from the Marcus Inverted Region can be further manipulated by other external stimuli such as a collector-base voltage bias and light irradiation (see Figure 4.19). In the first case, a positive voltage bias V_{CB} > 0V can enhance the built-in potential inside the C_{60}, which in turn

facilitates electron transport through the semiconductor. This extra potential leads to a larger current density, which progressively drives the system out of the Marcus Inverted Region. The effect of collector-base voltage bias is demonstrated in Figure 4.19a, where we plot in logarithmic scale I_C-V_{EB} curves at 180 K for $\mathbf{0 \leq V_{CB} \leq 3\ V}$. The same curves but in linear scale are shown in Figure 4.20. From these figures, we can see that as explained before the V_{CB} takes progressively the system out of MIR. In Figure 4.20i, where the minimum point of the effective NDR is plotted, we can see that at 180 K the change of regime happens at V_{CB} = + 3.0 V. Comparing this with the measurements at 120 K (Figure 4.21), the latter one does not show a change of regime in the $\mathbf{0 \leq V_{CB} \leq 3\ V}$ range. Figure 4.21i suggests that the Normal Marcus Regime should be reached at higher $\boldsymbol{V_{CB}}$. This possibly comes from the enhanced inversion occurring at lower temperatures. Finally, in order to give more strength to our statement that the effect comes from the organic semiconductor rather that from the metallic contact, we measure the V_{CB} dependence in Cu/C_{60} based i-MOS at 120 K. Figure 4.22 shows the evolution of MIR from $\mathbf{0 \leq V_{CB} \leq 3\ V}$.

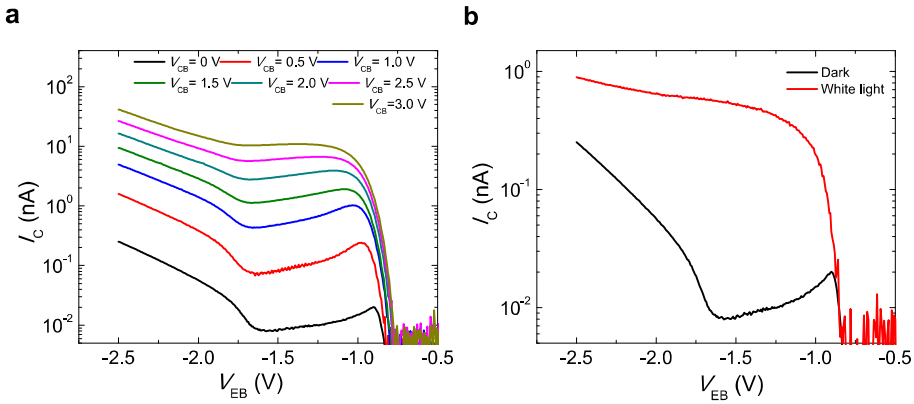

Figure 4.19| Manipulation of the negative differential resistance. a, Dependence of the direct hot-electron current, I_C, on V_{EB} for different collector-base bias, V_{CB}, at 180K. **b**, Hot-electron current I_C for V_{CB} = 0 V in dark (solid black line) and under white-light irradiation (7.5 mW cm^{-2} illuminating an area of 1 cm^2) (red solid line).

In the second case, the additional energy coming from the incident white light spectrum (with power density of 7.5 mW cm^{-2}) provides access to

several high-energy transport levels such as LUMO+1. This generated photocurrent in the C_{60} serves as an alternative parallel channel that as it can be seen in Figure 4.19b overrides the effective NDR. In Figure 4.23 is shown that he manipulation of NRD with light is possible at different temperatures.

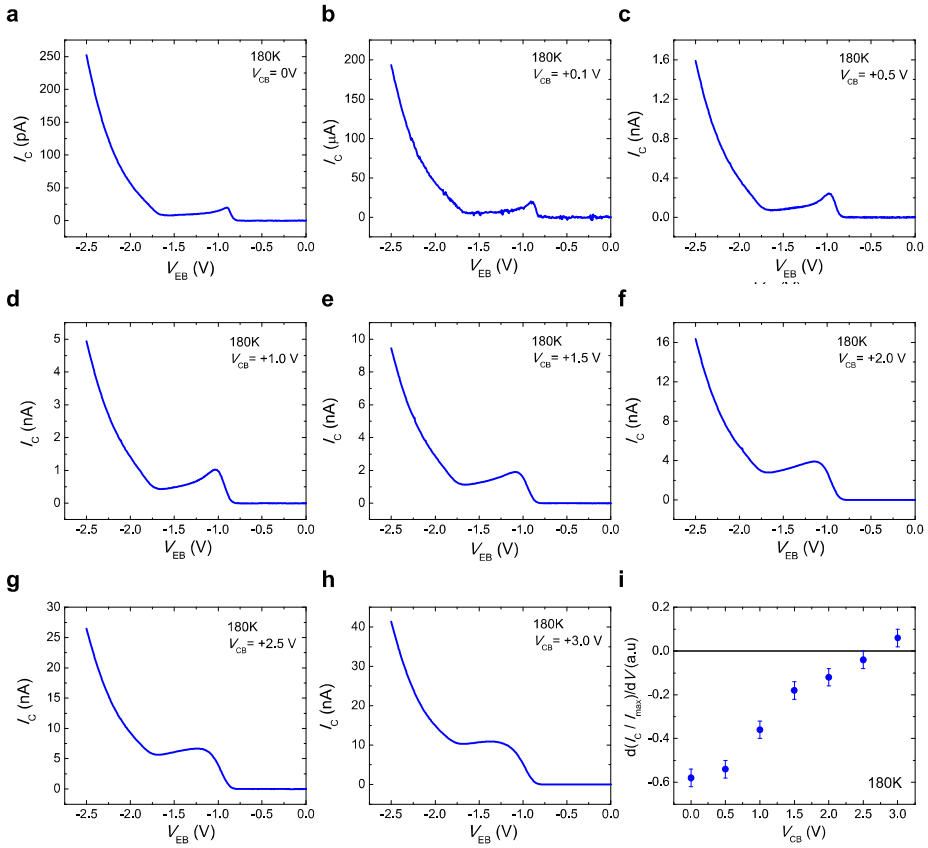

Figure 4.20| Collector current I_C for negative emitter-base bias $V_{EB} < 0$ V at 180 K of a Au/C_{60} based i-MOS. Energetic primary electrons are injected with $V_{CB} \geq 0$V into the lowest molecular orbital (LUMO) and first excited conductive molecular level (LUMO+1) of C_{60}. The lowering of the current observed between LUMO and LUMO+1 when no external V_{CB} bias is applied (**a**), gradually vanishes when higher positive V_{CB} is applied to the system (**b**-**i**). Figure **j** corresponds to the maximum change in the I_C at V_{EB} where effective negative differential resistance NDR is observed. The curves were normalized and the derivative respect to V_{EB} calculated yielding the minimum point of the effective NDR. This minimum is represented for positive V_{CB} at 180 K.

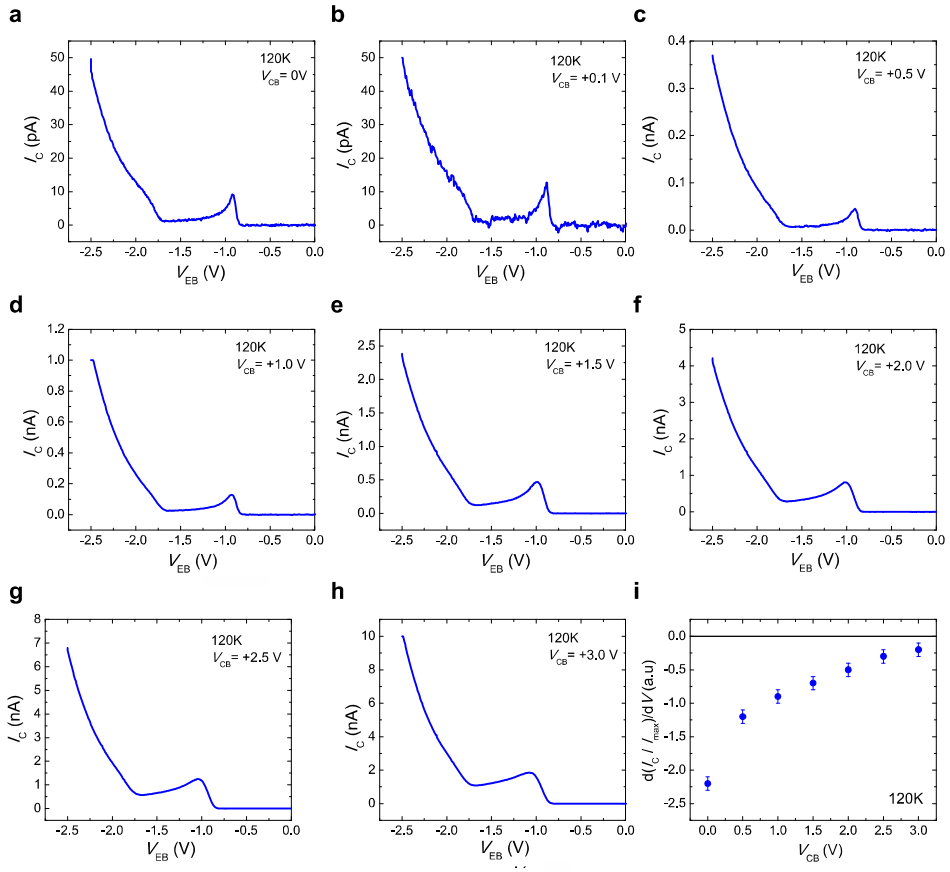

Figure 4.21| Collector current I_C for negative emitter-base bias V_{EB} < 0 V at 120 K in a Au/C60 based i-MOS. Energetic direct electrons are injected with $V_{BC} \geq 0$V into the lowest molecular orbital (LUMO) and first excited conductive molecular levels (LUMO+1) of C_{60}. The lowering of the current observed between LUMO and LUMO+1 when no external V_{BC} bias is applied (**a**), gradually becomes weaker when higher positive V_{BC} is applied to the system (**b**-**i**). Figure **j** corresponds to the maximum change in the I_C at V_{EB} where negative differential resistance NDR is observed. The curves were normalized and the derivative with respect to V_{EB} calculated yielding the minimum point of the NDR. This minimum is represented for positive V_{CB} at 120 K.

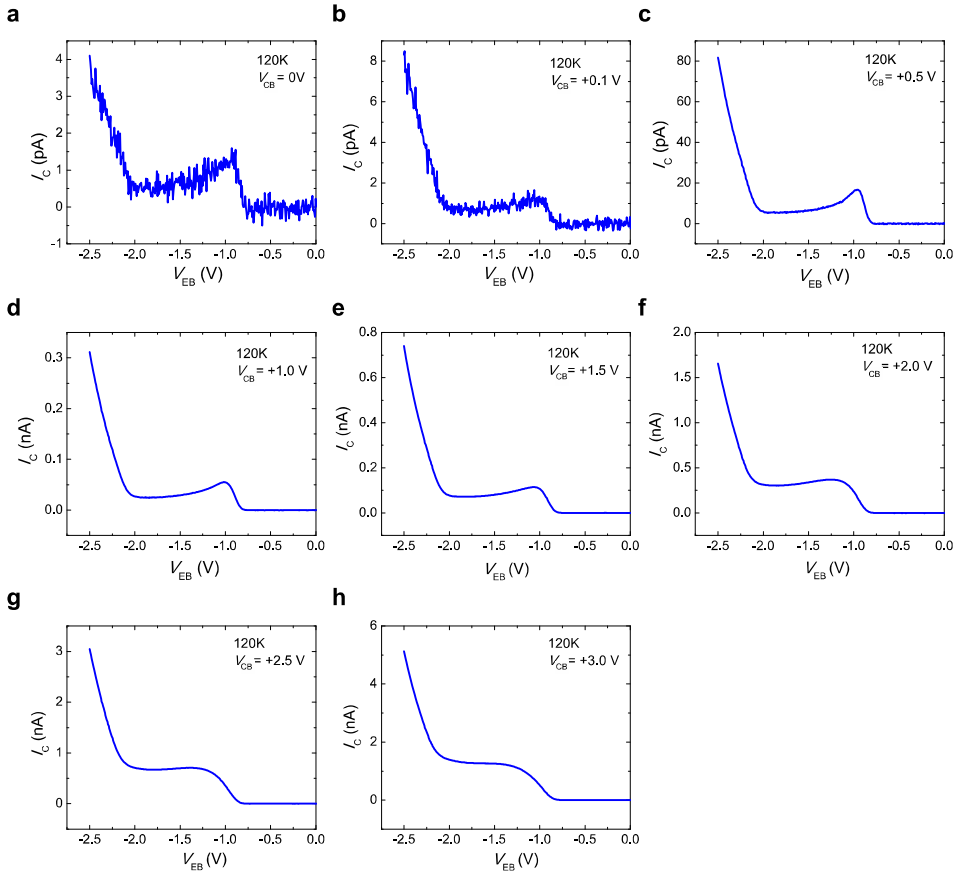

Figure 4.22| Collector current I_C for negative emitter-base bias V_{EB} < 0 V at 120 K in a Cu/C_{60} based i-MOS. Energetic direct electrons are injected with $V_{CB} \geq 0$ V into the lowest molecular orbital (LUMO) and first excited conductive molecular level (LUMO+1) of C_{60}. The lowering of the current observed between LUMO and LUMO+1 when no external V_{CB} bias is applied (**a**), gradually vanishes when higher positive V_{CB} is applied to the system (**b**-**i**).

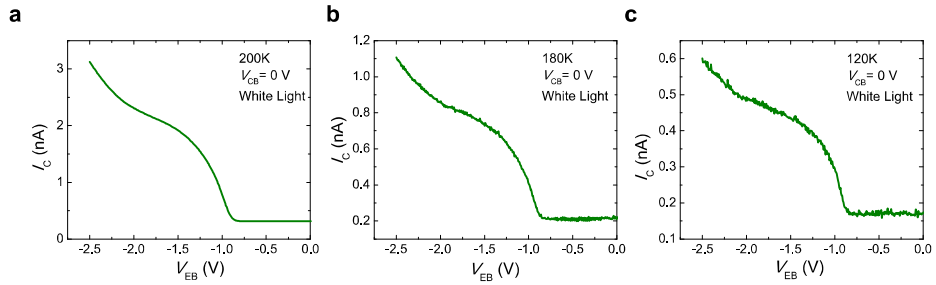

Figure 4.23| Collector current I_C for negative emitter-base bias V_{EB} < 0 V at 200 K, 180 K and 120 K and under white light irradiation. Energetic electrons are injected with V_{CB} = 0 V into the lowest molecular orbital (LUMO) and first excited conductive molecular level (LUMO+1) of C_{60}.

4.3.2 Control experiments

Some control experiments were performed to rule out any other possible effect rather than Marcus Inversion Regime as origin of the NDR that we have measured in the C_{60} based i-MOS devices. Hence, we have based on the original work of R. Marcus [41–44] to translate together with our theoretician colleagues from TU Dresden, the material parameters that might bring to the charges to access to the Marcus Inverted Region. Both the disorder and reorganization energy are two parameters to bear in mind [41–44]. In other words, molecules with relatively low disorder and reorganization energy (Λ) should show MIR while others with higher disorder and reorganization energy should not. In Marcus theory, Λ refers to the energy belonging to the transfer of a unit charge i.e. the energy of a state where the polarization would correspond to the transfer of a unit amount of charge, but the real charge distribution is that before the transfer. Based on these parameters, in Table 4.3 we gather up the disorder and reorganization energy values of C_{70} and PTCDI-C8. If we take the values of C_{60} as reference, we observe that both new molecules present higher disorder and reorganization energy. If now we compare C_{70} and PTCDI-C8, the last one has again both higher reorganization and particularly disorder energies. According to the simulations carried out by our collaborators from TU Dresden, this relatively large disorder energy of the PTCDI-C8 should prevent us from observing MIR in this system. In principle, C_{70} based i-MOS should show MIR feature.

Table 4.3| Disorder and reorganization energy of organic molecules

Molecule	Disorder (eV)	Λ (meV)
C_{60}	0	85
C_{70}	0.061	274
PTCDI-C8	0.235	384

We have performed three terminal i-MOS measurements with C_{70} and PTCDI-C8.

4.3.2.1 Marcus Inversion in C_{70}

Figure 4.24 shows the temperature dependence of I_C in logarithmic scale for negative $V_{EB} < 0$ V and $V_{CB} = 0$ V. In Figure 4.24a it is again observed that the continuous increase of I_C between LUMO and LUMO+1 at high temperatures (300 K – 240 K) converges into a reduction of I_C at 220 K. In other words, an effective NDR is observed between LUMO and LUMO+1 of C_{70}. This result follows the theoretical prediction and thus reinforces our statement of the direct observation of Marcus Inverted Regime in a solid-state device. Figure 4.24b shows I_C - V_{EB} measurements from 180 K to 20 K. While at the highest temperatures (Figure 4.24a) electrons are injected into the device and detected in the semiconductor, in this case not only an electron current is collected but also a hole current. In other words, at temperatures lower than 180 K and $V_{EB} < -1.8$ V the positive I_C turns negative, indicating that even if electrons are injected into the device, a secondary hole current is dominating at these $V_{EB.}$ This might come from the energy mismatch of the Au/C_{70}/Al stack (Figure 4.9), and the consecutive non-adequate built-in potential for the injection of electrons. At high temperatures, an electron current enters into LUMO and LUMO+1. However, at lower temperatures the charge mobility is lower and hence, the polarization of the built-in potential is more crucial for the charge transport through the organic semiconductor. Consequently, even if the LUMO level can be detected, secondary hole current is prominent. As HOMO and LUMO+1 are at similar energies with respect to the E_F of gold and the hole current is higher than electrons one, the onset corresponding to the HOMO level of C_{70} is measured

instead of the LUMO+1 level. Figure 4.25 shows in more detail the evolution of I_C with temperature in linear scale and with individual graphs.

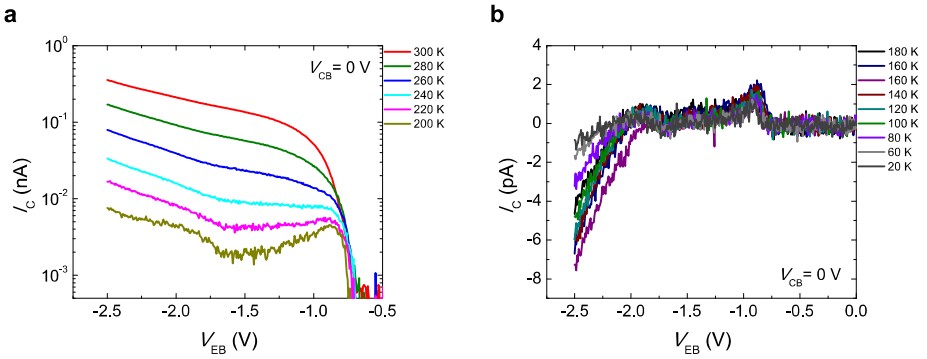

Figure 4.24| Temperature dependence of Au/C_{70} based i-MOS when V_{EB} < 0 and V_{CB} = 0 V. a, Temperature dependence of I_C in logarithmic scale from 300 K to 200 K. **b,** Temperature dependence of I_C from 180 K to 20 K.

In the case of C_{70}, the manipulation of NDR with the bias potential V_{CB} and the light is also possible. In Figure 4.26a we plot I_c in logarithmic scale versus V_{EB} at 200 K to show that a more positive V_{CB} enhances the built-in potential favourable for electron transport through the organic semiconductor. This drives the system progressively out of the MIR region. In more detail, at V_{CB} ≥1.5 V the system does not show NDR, which means that at this bias the system turns from inverted to normal Marcus regime. Figure 4.12 shows the individual plots in linear scale. Regarding light, we demonstrate again that the energy coming from a source of white light turns out C_{70} from the Inverted to the Normal Marcus regime. This is shown in Figure 4.26b, where direct electron current I_C without any external bias V_{CB} in dark (black solid line) and under white light (7.5 mW cm^{-2} illuminating an area of 1 cm^2) (red solid line) are plotted. As it was explained before, the energy coming from the white light source provides access to high-energy transport levels such as LUMO+1, which in turn serves as an alternative parallel channel to override the effective NDR.

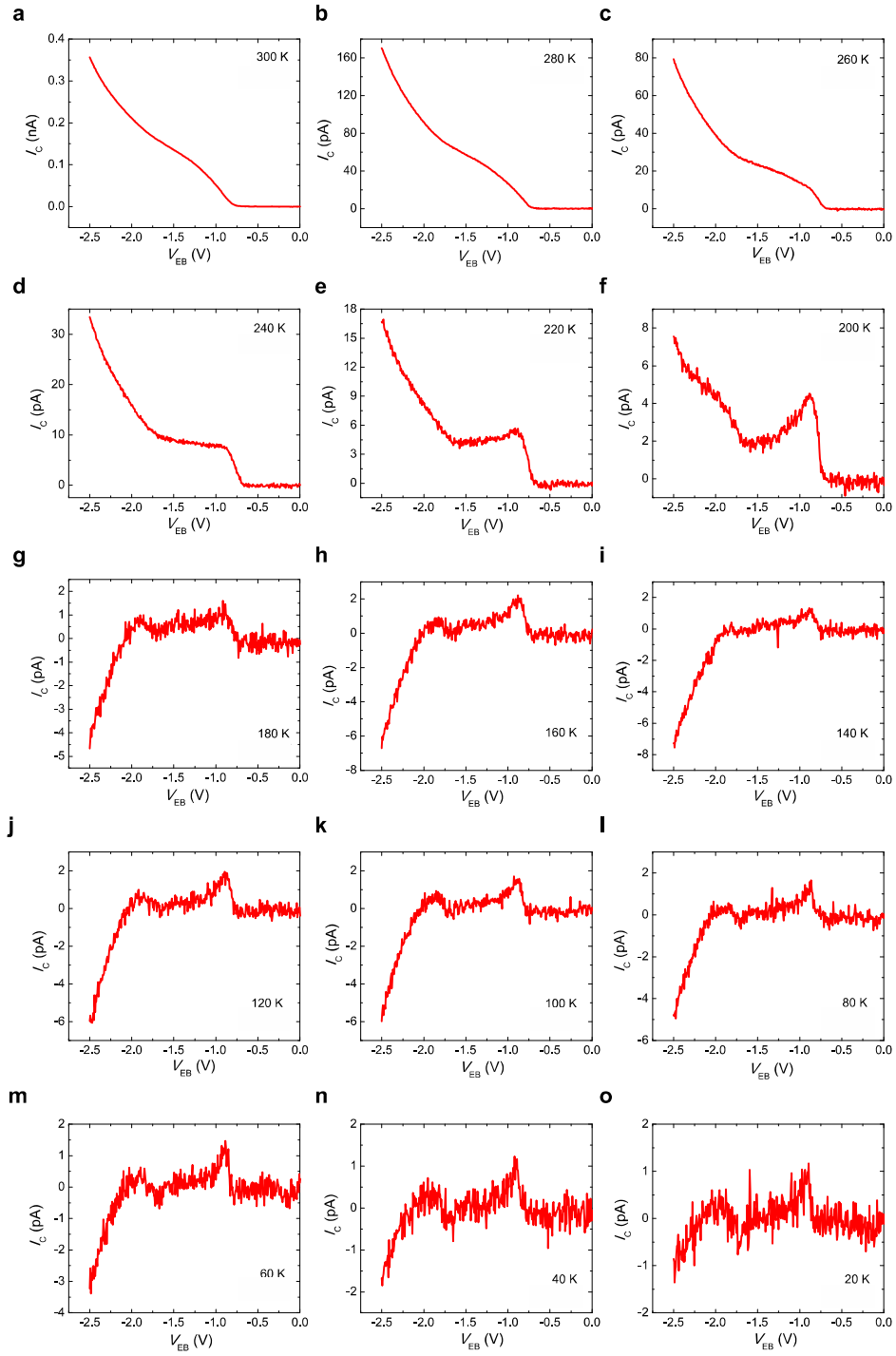

Figure 4.25|Collector current I_C for negative emitter-base bias VEB < 0 V at

temperatures from 300 K to 20 K for in-device molecular spectroscopy (i-MOS) with Au/C70 interface. In the range of 300 K to 200 K (**a**-**g**) energetic electrons are injected and detected with *V*CB = 0 V into the lowest molecular orbital (LUMO) and first excited conductive molecular level (LUMO+1) of C70. The increase of IC between LUMO and LUMO+1 at high temperatures (**a**-**d**) is reverted to show a decrease in the IC between LUMO and LUMO+1 below 220 K (**f** and **g**). Bellow 180 K (**h**-**p**) and around *V*EB= -2 V, IC changes from positive (electron detection) to negative (hole detection). From 180 K to 100 K (**h**-**l**) the amplitude of IC does not significantly change.

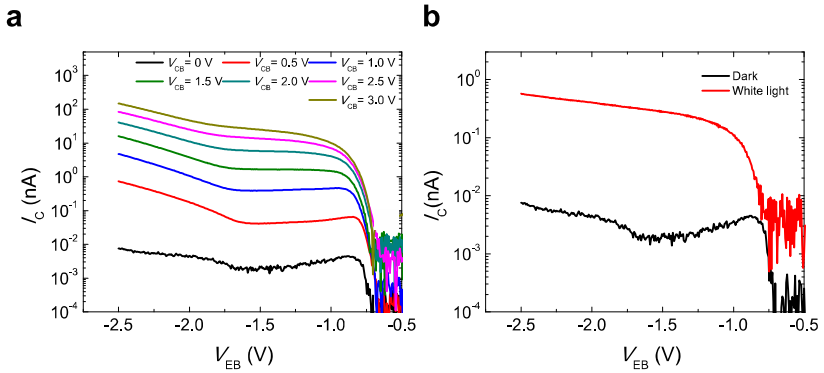

Figure 4.26| Negative differential resistance manipulation at 200 K. a, Positive collector-base bias $V_{CB} > 0$ dependence of I_C for negative $V_{EB} < 0$. The NDR is reduced whit the increase in V_{CB}. **b**, I_C-V_{EB} measurements for $V_{CB} = 0$ V in dark (black solid line) and under white light irradiation (7.5 mW cm^{-2} illuminating an area of 1 cm^2) (red solid line).

4.3.2.2 Control experiment with PTCDI-C8

In the previous sections we have been able to directly access observe and manipulate the negative differential resistance coming from the MIR in C_{60} and C_{70}. These molecules have a low reorganization and disorder energies, which according to theory are the required conditions for the observation of MIR. However, in Table 4.3 we showed that PTCDI-C8 have larger reorganization and disorder energies, which according to the predictions from the group of Dr. Ortmann should in principle not make possible the observation of this intriguing regime, i.e. it has a large reorganization and disorder prevent us from monitoring MIR. Thus, in this subsection we perform three terminal measurements in Au/PTCDI-C8 based i-MOS.

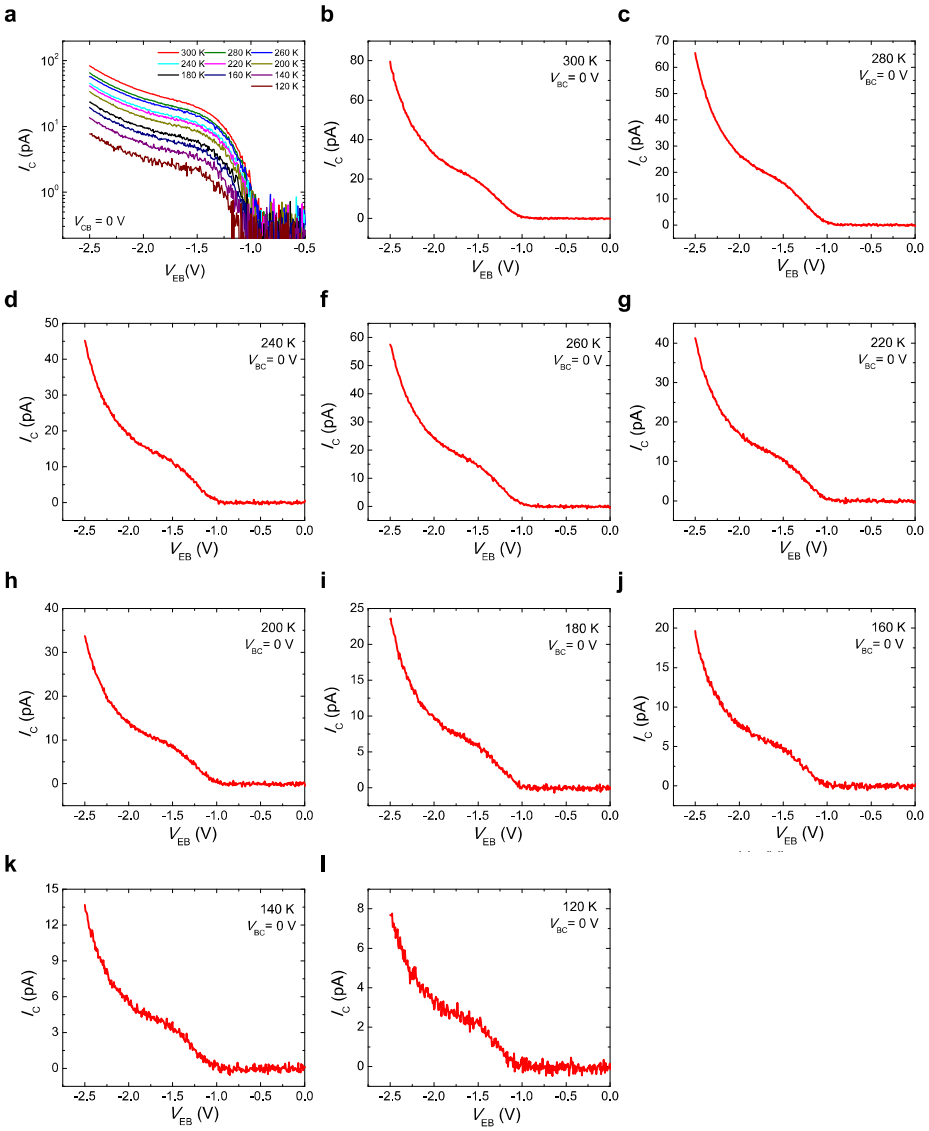

Figure 4.27| Temperature dependence of direct electron current at PTCDI based i-MOS. Collector current I_C for negative emitter-base bias V_{EB} < 0 V from 300 K to120 K for in-device molecular spectroscopy (i-MOS) with Au/PTCDI-C8 interface. Energetic electrons are injected and detected with V_{CB} = 0 V into the lowest molecular orbital (LUMO) and first excited conductive molecular level (LUMO+1) of PTCDI-C8 (**a**-**i**). Figure **a**, shows the all temperature range by plotting log(I_C)-V_{EB} curves , while figures **b**-**k** are individual I_C-V_{EB} in linear scale.

Fabrication and device characterization details are further discussed in Appendix A. We have not included i-MOS based on PTCDI-C8 in this section because the leaky diodes that we got prevented performing a complete characterization.

Figure 4.27a shows direct electron I_C current in logarithmic scale from 300 K to 120 K. A continuous increase in I_C is observed between LUMO (1.0 ± 0.1 eV) and LUMO+1 (1.9 ± 0.1 eV) for all the temperatures. No signal of NDR is detected, and thus, the system is in Normal Marcus Regime. This can be seen in more detail in the one-temperature I_C-V_{EB} curves plotted in Figure 4.27b-k.

Therefore, we have shown that molecules with low reorganization and disorder energy, such as C_{60} and C_{70} can access MIR while molecules such as PTCDI-C8, which have large reorganization and disorder energy, cannot do. Our experiments are in agreement with the theory predictions, which confirm the observation of this captivating energy crossover in a solid-state device.

4.4 Conclusions

In conclusion, we based in the i-MOS technique and we report a full energy characterization of both hole and electron transport levels of C_{60} and C_{70}. We do not only access the ground state but we also detect excited states such as LUMO+1. We do this by direct electron and hole injection-detection as well as by secondary electron and hole detection. These secondary currents come from inelastic scattering and a similar process to Auger scattering that happen at the base contact of the device. Moreover, the determination of HOMO and LUMO levels of a molecular semiconductor in device operative conditions, without any prior material parameter, and using a single vertical device permits the calculation of the transport energy gap of the organic material in a direct and a simple manner. This information cannot be directly obtained by any other experimental technique, while it is paramount for the understanding and development of future molecular-based (opto)-electronic devices. We have compared our results with the energy values calculated from other spectroscopy methods and we have seen that the information extracted by i-MOS is consistent and reliable

The high-energy carrier injection range permits us access the Marcus Inverted Region for the transport of electrons. This regime, previously explored for chemical reactions in solution, opens the possibility to explore the physics of a novel manner of injecting charges into molecular semiconductors as well as integrating the NDR consequence of the MIR in electronic circuiting. Marcus Inverted Regime is directly observable in the three terminal i-MOS measurements, where temperature, electric field across the semiconductor and light permits its manipulation. We have observed this intriguing regime in C_{60} and C_{70}, materials with low reorganization and disorder energies. Control experiments with PTCDI-C8 and the theoretical modelling of our collaborators confirm our statement.

References

1. Schwarze, M. *et al.* Band structure engineering in organic semiconductors. *Science (80-.).* **352,** 1446–1449 (2016).
2. Holliday, S. *et al.* High-efficiency and air-stable P3HT-based polymer solar cells with a new non-fullerene acceptor. *Nat. Commun.* **7,** 11585–1196 (2016).
3. Lee, J. *et al.* Deep blue phosphorescent organic light-emitting diodes with very high brightness and efficiency. *Nat. Mater.* **15,** 92–98 (2015).
4. Muccini, M. A bright future for organic field-effect transistors. *Nat. Mater.* **5,** 605–613 (2006).
5. Forrest, S. R. Electronic Appliances on Plastic. *Nature* **428,** 911–918 (2004).
6. Sun, X. *et al.* A molecular spin-photovoltaic device. *Science (80-.).* **357,** 677–680 (2017).
7. Bredas, J. L. Mind the gap! *Mater. Horiz.* **1,** 17–19 (2014).
8. Nitzan, A. & Ratner, M. A. Electron Transport in Molecular Wire Junctions. *Science (80-.).* **300,** 1384–1389 (2003).
9. Bannani, A., Bobisch, C. & Moller, R. Ballistic Electron Microscopy of Individual Molecules. *Science (80-.).* **315,** 1824–1828 (2007).
10. Jung, M. *et al.* Atomically resolved orientational ordering of C60 molecules on epitaxial graphene on Cu(111). *Nanoscale* **6,** 11835–11840 (2014).
11. Evans, D. A. *et al.* Transport and optical gaps and energy band alignment at organic-inorganic interfaces. *J. Appl. Phys.* **114,** 123701–8 (2013).
12. Gregg, B. A. & Hanna, M. C. Comparing organic to inorganic photovoltaic cells: Theory, experiment, and simulation. *J. Appl. Phys.* **93,** 3605–3614 (2003).
13. Kahn, A. Fermi level, work function and vacuum level. *Mater. Horizons* **3,** 7–10 (2016).
14. Holze, R. Optical and Electrochemical Band Gaps in Mono-, Oligo-, and Polymeric Systems: A Critical Reassessment1. *Organometallics* **33,** 5033–5042 (2014).
15. Braun, S., Salaneck, W. R. & Fahlman, M. Energy-Level Alignment at Organic / Metal and Organic / Organic Interfaces. **21,** 1450–1472

(2009).

16. Shirley, E. L. & Louie, S. G. Electron excitations in solid C60: Energy gap, band dispersions, and effects of orientational disorder. *Phys. Rev. Lett.* **71,** 133–136 (1993).

17. Hwang, J., Wan, A. & Kahn, A. Energetics of metal – organic interfaces : New experiments and assessment of the field. *Mater. Sci. Eng. R* **64,** 1–31 (2009).

18. Atxabal, A. *et al.* Energy Level Alignment at Metal / Solution-Processed Organic Semiconductor Interfaces. *Adv. Mater.* **10,** 1606901–6 (2017).

19. Haddon, R. C. *et al.* C60 thin film transistors. *Appl. Phys. Lett.* **67,** 121–123 (1995).

20. Haddon, R. C. C70 Thin Film Transistors. *J. Am. Ceram. Soc.* **118,** 3041–3042 (1996).

21. Luo, X. *et al.* Remarkably enhanced red–NIR broad spectral absorption via gold nanoparticles: applications for organic photosensitive diodes. *Nanoscale* **7,** 14422–14433 (2015).

22. Tan, Z. *et al.* Facile deposition of gold nanoparticles on C60 microcrystals with unique shapes. *J. Nanoparticle Res.* **15,** 2029–2039 (2013).

23. Gobbi, M. *et al.* Determination of energy level alignment at metal/molecule interfaces by in-device electrical spectroscopy. *Nat. Commun.* **5,** 4161–4168 (2014).

24. Sun, X. *et al.* Room temperature air-stable spin transport in bathocuproine-based spin valves. *Nat. Commun.* **4,** 2794–7 (2013).

25. Ma, L. *et al.* High-speed and high-current density C60 diodes. *Appl. Phys. Lett.* **84,** 4786–4788 (2013).

26. Gobbi, M. *et al.* Determination of energy level alignment at metal/molecule interfaces by in-device electrical spectroscopy. *Nat. Commun.* **5,** 4161–4168 (2014).

27. Balkan, N. in *Hot electrons in semiconductors* 385–427 (Clarendon Press, 1998).

28. Kaiser, W. J. & Bell, L. D. Direct investigation of subsurface interface electronic structure by ballistic-electron-emission microscopy. *Phys. Rev. Lett.* **60,** 1406–1410 (1988).

29. Bell, L. D. & Kaiser, W. J. Observation of Interface Band Structure by

Ballistic-Electron-Emission Microscopy. *Phys. Rev. Lett.* **61,** 2368–2371 (1988).

30. Bauer, M., Marienfeld, A. & Aeschlimann, M. Hot electron lifetimes in metals probed by time-resolved two-photon photoemission. *Prog. Surf. Sci.* **90,** 319–376 (2015).

31. Yi, W., Narayanamurti, V., Lu, H., Scarpulla, M. A. & Gossard, A. C. Probing semiconductor band structures and heterojunction interface properties with ballistic carrier emission: GaAs/ Alx Ga 1-x As as a model system. *Phys. Rev. B* **81,** 235325–13 (2010).

32. Yi, W. *et al.* Bandgap and band offsets determination of semiconductor heterostructures using three-terminal ballistic carrier spectroscopy. *Appl. Phys. Lett.* **95,** 112102–3 (2009).

33. Bell, L. D. New electron and hole spectroscopies based on ballistic electron emission microscopy. *J. Vac. Sci. Technol. B Microelectron. Nanom. Struct.* **9,** 594–600 (1991).

34. Ludeke, R. & Prietsch, M. Ballistic electron emission spectroscopy of metals on GaP(110). *J. Vac. Sci. Technol. A* **9,** 885–890 (1991).

35. Bell, L. D., Hecht, M. H., Kaiser, W. J. & Davis, L. C. Direct spectroscopy of electron and hole scattering. *Phys. Rev. Lett.* **64,** 2679–2682 (1990).

36. Esaki, L. New Phenomenon in Narrow Germanium p-n Junctions. *Phys. Rev.* **109,** 603–604 (1957).

37. Yan, R. *et al.* Esaki Diodes in van der Waals Heterojunctions with Broken-Gap Energy Band Alignment. *Nano Lett.* **15,** 5791–5798 (2015).

38. Rashidi, M. *et al.* Time-Resolved Imaging of Negative Differential Resistance on the Atomic Scale. *Phys. Rev. Lett.* **117,** 276805–5 (2016).

39. Perrin, M. L. *et al.* Large negative differential conductance in single-molecule break junctions. *Nat. Nanotechnol.* **9,** 830–834 (2014).

40. Choi, W. S., Lee, S. A., You, J. H., Lee, S. & Lee, H. N. Resonant tunnelling in a quantum oxide superlattice. *Nat. Commun.* **6,** 7424–7430 (2015).

41. Marcus, R. A. Electron transfer reactions in chemistry. Theory and experiment. *Rev. Mod. Phys.* **65,** 599–610 (1993).

42. Marcus, R. A. Theory, Experiment, and Reaction Rates. A Personal View. *J. Phys. Chem.* **90,** 3460–3465 (1986).

43. Marcus, R. A. On the Theory of Oxidation-Reduction Reactions

Involving Electron Transfer. I. *J. Chem. Phys.* **24,** 966–978 (1956).

44. Marcus, R. A. Chemical and electochemical electron-transfer theory. *Annu. Rev. Phys. Chem.* **15,** 155–196 (1964)

Chapter 5

Flexible in-device molecular spectroscopy

The lure of flexible, wearable, and transparent electronics has drawn the attention of researchers and entrepreneurs in the last years [1–4]. However, there are still challenges, such as the instability and the lower efficiency of the devices compared to rigid ones, that still need be overcame. As already mentioned along this thesis, the energy barriers at the metal/organic semiconductor interfaces are one of the main parameters responsible of the efficiency of (opto-)electronic devices., and that is also the case with flexible devices. Concretely, it is imperative to understand how the energy barriers at metal/semiconductor interface change under mechanical strain [5,6]. Two years ago Y. Wu *et al*. [7] reported that the work function of a rubrene crystal slightly changes with strain. The measurements were performed by Kelvin prove and the strain was induced by thermally expanding or contracting the organic single crystal. This approach is far from real device operative conditions [7] so it is still inconclusive how this apparent changes would affect to the charge transport.

In this chapter, we study the strain dependence of the interface energy barrier between the Fermi level of gold and the lowest unoccupied molecular orbital (LUMO) state of two n-type molecular semiconductors by i-MOS. The devices are fabricated on flexible Kapton tape which permits inducing mechanical strain in the device just by bending it. The measurements are performed in-device operative conditions while the samples are bent.

5.1 Device fabrication

All the devices described in this chapter are fabricated on a 280 μm-thick Kapton tape substrate. Kapton is a flexible and highly resistive plastic material which maintains its mechanical properties from 4 K to 673 K. Moreover, it has been already proved in previous works as a low–cost flexible substrate [8–11]. During the sample fabrication process we faced problems with the adhesion of non-ferromagnetic materials on Kapton. The problem was solved by integrating the following steps in the fabrication process: i) overnight degassing of bare Kapton substrates in high vacuum (10^{-6}-10^{-7} mbar, load-lock of the evaporator); ii) deposition of an adhesion layer of Co_2O_3. For this last procedure 0.5 nm-thick Co layer was evaporated by e-beam at ~ 1 Å s^{-1} all over the chip. This step is done only to modify the surface of Kapton by bombarding energetic atoms on it. Co could be replaced in principle by any other ferromagnetic material available in the lab. The reason behind using a ferromagnetic material is the good adhesion they have demonstrated in previous works [9,11]. In order to prevent non-desired conducting paths through the adhesion layer, Co film is submitted to a double step oxidation process consisting of 2 minutes of low power (1200 V, 10 mA) and 3 minutes of high power (1200 V, 50 mA) oxygen plasma. Before starting the optimization of the adhesion of the materials, we tested polyethylene terephthalate (PET) substrates, widely used for flexible electronics. However, we again had similar problems with the bad adhesion of non-ferromagnetic metals.

As in all the i-MOS devices described in this thesis, aluminium is used as the emitter contact. In this case the emitter was 20 nm-thick film thermally evaporated with a rate of $\sim \mathbf{0.7}$ Å $\mathbf{s^{-1}}$. It thicker than for rigid substrates to ensure the continuity of the film. Aluminium was exposed to plasma oxygen for 2 min at 1200 V - 10 mA and 3 min 1200 V - 50 mA. A 15 nm-thick gold layer was deposited by e-beam as the base contact with a rate of $\sim \mathbf{1.0}$ Å $\mathbf{s^{-1}}$. The collector is 200-nm thick molecular layer deposited at $\sim \mathbf{0.1}$ Å $\mathbf{s^{-1}}$ rate. In this work we based on C_{60} (Sigma Aldrich, sublimed 99.9%), a spherical molecule, and *N*,*N*′-Dioctyl-3,4,9,10-perylenedicarboximide (PTCDI-C8) (Sigma Aldrich, 98% purity), a planar molecule. Finally, 20 nm-thick aluminium film is deposited as the top contact. This electrode is evaporated in two steps in order to avoid harming the molecular layer. First, 2nm or 4 nm of aluminium are evaporated at

$\sim \mathbf{0.1}$ Å $\mathbf{s^{-1}}$ for C_{60} and PTCDI-C8 respectively. In this way a thin film of aluminium covers the molecular surface protecting it from damages that energetic aluminium atoms could cause. Then, aluminium is evaporated with a rate of $\sim \mathbf{0.6}$ Å $\mathbf{s^{-1}}$ until a total layer thickness of 20 nm. This last step prevents burning the molecular interface due to a prolonged exposure of the sample to the evaporation source. Table 5.1 lists the fabrication steps described above.

Table 5.1| Fabrication recipe. The table shows the sample fabrication steps followed in this work.

Layer	Material	Thickness	Evaporation rate
Adhesion layer	Co	0.5 nm	1.0 Å s^{-1}
	O_2	2' (1200 V, 10 mA) + 3' (1200 V, 50 mA)	
Emitter	Al	20 nm	1.0 Å s^{-1}
	O_2	2' (1200 V, 10 mA) + 3' (1200 V, 50 mA)	
Base	Au	15 nm	1.0 Å s^{-1}
Collector	C_{60}	200 nm	0.1 Å s^{-1}
	PTCDI-C8		
Top Contact	Al	2 nm + 18 nm	0.1 Å s^{-1}+0.6 Å s^{-1}
		4 nm + 16 nm	

5.2 Sample characterization

The electrical measurements of the devices are performed with the three-terminal i-MOS sensing scheme. All the experiments were repeated with the samples flat and bent for five different bending radiuses $r = 40, 25, 15, 12.5, 5$ mm. The samples were placed on cylindrical sample holders (see Figure 5.1), which permitted performing the measurements while the strain was applied to the devices. The applied mechanical strain on the sample increases when decreasing the bending radius of the holder following the relation

$$\varepsilon = \frac{d}{2r} \qquad \text{(Eq. 5.1)}$$

where *d* is the thickness of the sample [12,13]. Following (Eq. 5.1) the induced strain with the bending radiuses of the sample holders that we have used is shown in Table 5.2.

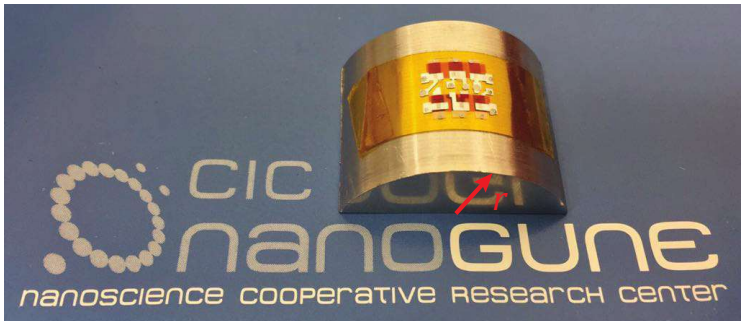

Figure 5.1| A sample holder. The photography shows a bent flexible chip on Kapton with six i-MOS devices. The sample is pasted on a half cylinder that works as sample holder and that permits performing measurements under applied strain.

Table 5.2| Bending radius and induced strain. The table shows the different bending radiuses used and the calculated strain that they induce on the sample.

***r* (mm)**	**ε (%)**
Flat	0
40	0.35
25	0.56
15	0.93
12.5	1.12
5	2.8

5.2.1 Topographical measurements

We have performed atomic force microscopy (AFM) measurements on C_{60} and PTCDI-C8 molecular films to study the effects of bending and strain on their topography. Following the recipe of flexible i-MOS devices, 200 nm-thick of C_{60} and PTCDI-C8 were grown on 10 nm-thick gold film.

Figure 5.2a and Figure 5.2b are 5 μm x 5 μm and 10 μm x 10 μm area AFM images of C_{60} on gold taken before bending. The measurements were performed with the sample flat. Figure 5.2e and Figure 5.2f correspond to the same samples of Au/C_{60} but in this case the sample was bent several times before measuring it flat again. Comparing the pictures before and

after bending, we do not observe any noticeable change in the morphology of the molecular layer. Same conclusion is taken after comparing the morphology of PTCDI-C8 layer on gold before (Figure 5.2c, d) and after bending it (Figure 5.2 g, h). No noticeable damage is observed on the molecular surface after it was repeatedly bent.

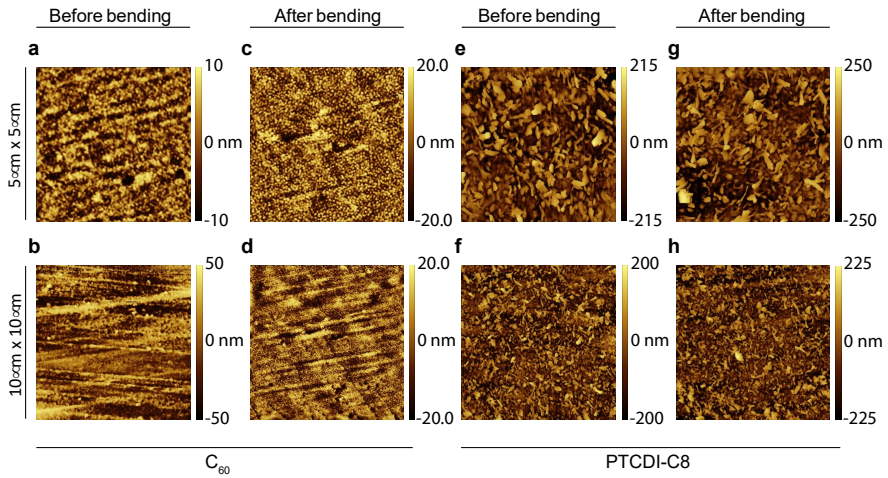

Figure 5.2| Atomic force microscopy (AFM) images of C_{60} and PTCDI-C8 molecular layers. a, 5 µm x 5 µm AFM image area of 200 nm of C_{60} on gold with Kapton substrate. The image has been taken flat and without having bent it. **b,** 10 µm x 10 µm AFM image of 200 nm of C_{60} on gold and on Kapton substrate. **c**, 5 µm x 5 µm AFM image area of 200 nm of PTCDI-C8 on gold with Kapton as substrate. The image has been taken flat and without prior bending. **d**, Non-bent 10 µm x 10 µm AFM image area of 200 nm of PTCDI_C8 on gold with Kapton substrate. **e**, 5 µm x 5 µm AFM image area of 200 nm of C_{60} on gold with Kapton substrate. The image has been taken flat after having bent it. **f**, 10 µm x 10 µm AFM image area of 200 nm of C_{60} on gold and with Kapton substrate. The sample has been bent before measurement. **g**, 5 µm x 5 µm AFM image area of 200 nm of PTCDI-C8 on gold with Kapton substrate. The image has been taken flat after having bent it. **h**, 10 µm x 10 µm AFM image area of 200 nm of C_{60} on gold with Kapton substrate. The sample has been bent before measurement.

In the AFM images shown in Figure5.2 visible and repetitive groves are observed. These marks are not related to the damage induced by the strain coming from bending of the sample. In order to rule out their origin, we performed AFM measurements on bare Kapton substrates. Figure 5.3 shows a 10 µm x 10 µm AFM image of this substrate, where the groves are visible.

This suggests that the marks are from the tape, probably coming from the irregularities created in the fabrication of the substrates.

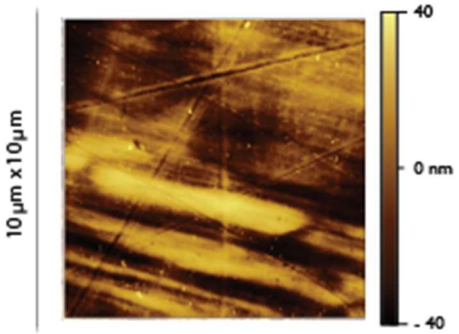

Figure 5.3| 10 µm x 10 µm atomic force microscopy (AFM) scan of a Kapton substrate.

5.2.2 Tunnel Junction

The tunnel junction of our devices is a **~3 nm** thick Al_2O_3 layer sandwiched between aluminium and gold: $Al/Al_2O_3/Au$. Following the sensing scheme described in Chapter 1, when a bias V_{EB} is not applied between the emitter and the base, the device remains in equilibrium and there is not charge transfer between both contacts (Figure 5.4). However, when V_{EB} is applied charges are accelerated from the metallic contact towards the tunnel junction. Depending on whether the applied V_{EB} is positive or negative, electrons are accelerated from base to emitter or from emitter to base, respectively. Charges need a minimum bias to tunnel through the Al_2O_3 thin film, and thus, the energy of the injected charges will depend on the applied V_{EB}.

Figure 5.4a and b show the characteristic I_E - V_{EB} curve of the non-leaky tunnel junctions[14] of a C_{60} and PTCDI-C8 based i-MOS fabricated on Kapton substrate. Aluminium and gold grow grainier on Kapton tape than on SiO_2, which results on more resistive metallic contacts. Thus, the current through the flexible tunnel junction is an order of magnitude lower than the tunnelling current measured on rigid substrates, which were shown in previous chapters. Besides, the differences in the shape and the resistance

of the I_E - V_{EB} curves between the C_{60} and the PTCDI-C8 based devices might be related to possible variations in the fabrication process of the samples.

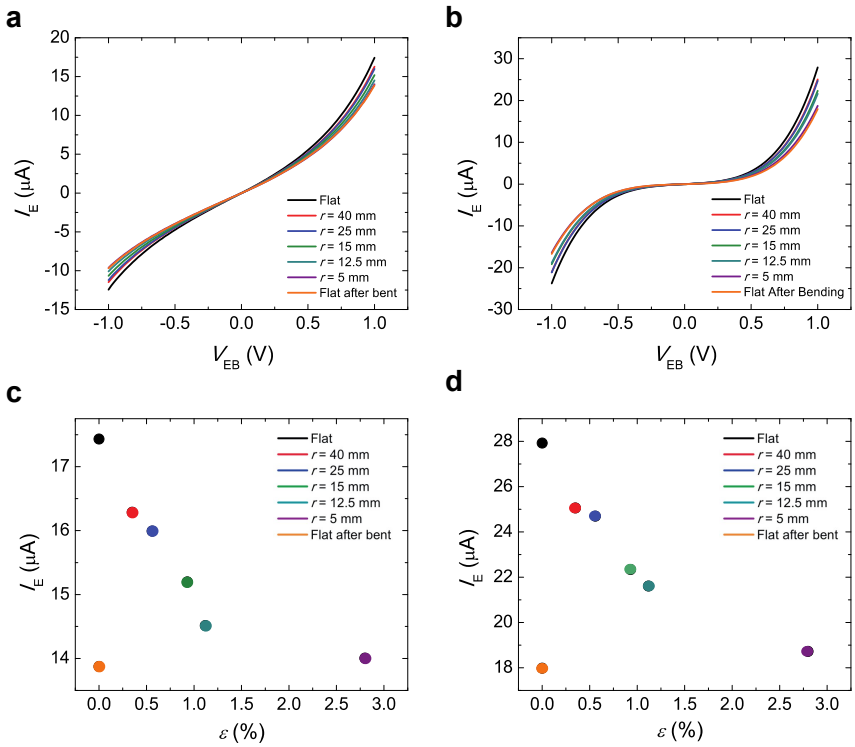

Figure 5.4| Tunnel junctions with and without strain. a, Emitter current I_E measured in the $Al/Al_2O_3/Au$ junction of the C_{60} based device when a bias is applied between the emitter and the base V_{EB}. The junction has been measured under different strain conditions by bending the sample onto semi cylindrical holders with different radius. **b**, I_E - V_{EB} curves measured through the $Al/Al_2O_3/Au$ junction of the PTCD-C8 based device. The junction has been measured under different strain conditions by bending the sample onto semi- cylindrical holders with diverse radius. **c**, Strain dependence of I_E at V_{EB} = 1 V of the C_{60} based device. **d**, Strain dependence of I_E at V_{EB} = 1 V in the case of the PTCDI-C8 based device.

Regarding the differences in the I_E current between flat and bent conditions (see Figure 5.4a, b), no significant change is detected. The current slightly decreases with the bending radius getting at the maximum a 20% (C_{60} based device) and 33% (PTCDI-C8 based device) reduction of I_E between no-strain (flat) and maximum-strain ($\boldsymbol{r = 5\ mm}$) cases (Figure 5.4c, d). We believe

that when thin films are bent, the separation between its metallic grains is enlarged compared to the case when the sample is flat and thus, the charge transport is hinder. Additionally, it has been observed that the devices do not recover the initial performance once they have been bent.

5.2.3 Base-collector diode

In this section we focus on the two-terminal Au/molecule (C_{60}/PTCDI)/Al junctions. Applying a bias between the collector and the base V_{CB} charge carriers are injected from the metallic electrodes to the organic semiconductor. When a negative bias $V_{CB} < 0$ is applied electrons are injected from the collector (Al) to the base (Au), while when the bias is positive $V_{CB} > 0$ the electrons go from the base to the collector. Changing the radius of the sample holders, we are able to manipulate the applied strain on the junction.

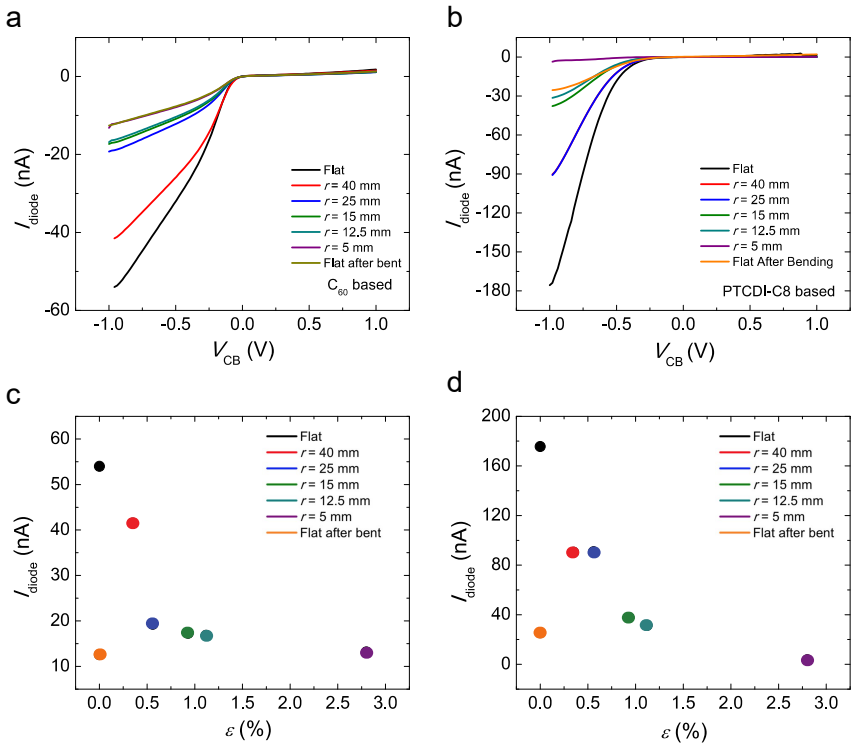

Figure 5.5| Au/C_{60}/Al and Au/PTCDI-C8/Al diodes with different bending radius. a, Current through Au/C_{60}/Al stack, I_{diode}, for applied collector base bias,

V_{CB}, when it is measured in flat and bended to r = 40, 25, 15, 12.5 and 5 mm. **b**, Characteristic I_{diode}- V_{CB} curves of Au/PTCDI-C8/Al diode lying flat and bent to r = 40, 25, 15, 12.5 and 5 mm. **c**, Strain dependence of I_{diode} at V_{CB} = -1 V in the case of the C_{60} based device. **d**, Strain dependence of I_{diode} at V_{CB} = -1 V in the case of the PTCDI-C8 based device.

Figure 5.5a shows the characteristic I_{diode}- V_{CB} curve of Au/C_{60}/Al junction, where a rectifying diode like shape is observed. In other words, the current is more likely to be injected from the top aluminium contact rather than from the gold base due to the higher energy barrier that is between the Fermi level of this last metal and the LUMO level of C_{60}. A similar behaviour is observed for the Au/PTCDI-C8/Al junction (see Figure 5.5b). Moreover, this rectifying behaviour is observed not only when the sample is flat but also when is bent. This demonstrates that the metal/molecule interface does not become leaky when strain is applied to the sample.

In both cases, the amplitude of the I_{diode} decreases when increasing the applied strain on it (see Figure 5.5c, d). The bending enlarges the distance between grains, and consequently the resistivity of the metallic contacts and the molecular layer is enlarged. Notice that the charges are injected directly from the Fermi of the metallic electrodes to the LUMO of the molecule. Hence, the resistivity of the electrodes has a large contribution to the resistivity of the junction resulting in a lower current through the junction.

Finally, comparing the measurements done with the sample flat before and after the bending, both Au/C_{60}/Al and Au/PTCDI-C8/Al stacks give a 76.7% and 85.5% lower final current than the initial one, respectively. This shows that these metal/molecule/metal junctions are non-reversible to bending.

5.2.4 Three-terminal measurements

The spectroscopic characterization of the energy barriers at the metal/molecule interfaces is carried by the three-terminal measurement configuration described in Chapter 1. Applying a voltage V_{EB} between the emitter and the base, electrons tunnel into the device. We monitor the I_C current that arrives to the collector. All the measurements were performed at 300 K and the bias between collector and base (V_{CB}) was set to zero.

Figure 6a and Figure 6b show the I_C - V_{EB} curve of C_{60} and PTCDI-C8 based i-MOS devices, respectively, measured with the sample was flat

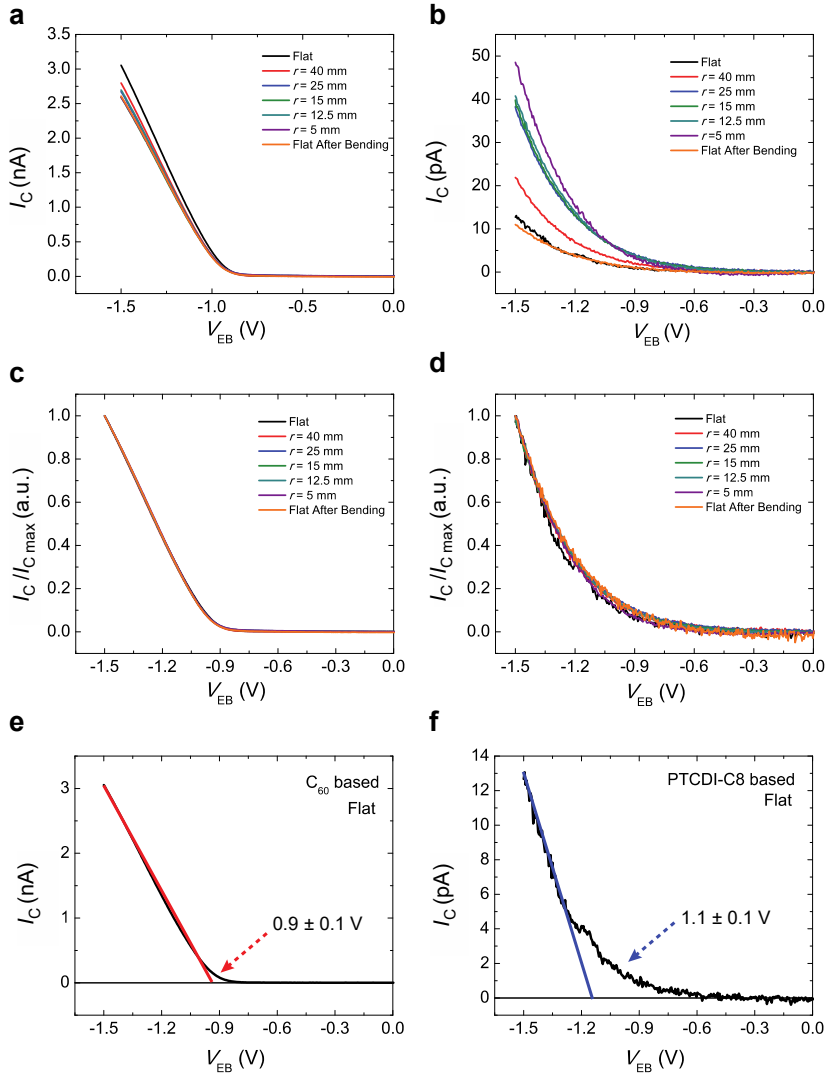

Figure 5.6| Strain dependence of hot electron current. a, Hot electron current I_C of the C_{60} based device vs. emitter-base bias V_{EB} for different bending radius. **b**, I_C - V_{EB} of the PTCDI-C8 based device for different bending conditions. **c**, Normalized $I_C/I_{C\,max}$ - V_{EB} curves of C_{60} based device for different bending radius. **d**, Normalized $I_C/I_{C\,max}$ - V_{EB} curves of PTCDI-C8 based device for different bending radius. **e**, Strain dependence of I_C at V_{CB} = -1.5 V in the case of the C_{60} based device. **f**, Strain dependence of I_C at V_{CB} = -1 V for the PTCDI-C8 based device.

without any strain and under strain by varying the bending radius of the sample holder from 5 mm to 40 mm. Figure 6c (C_{60}) and Figure 6d (PTCDI-C8) represent I_C normalized with the maximum collector current $I_{C\ max}$, and they better show that the energy barrier at Au/C_{60} and Au/PTCDI-C8 interfaces do not vary with strain. In both cases the *I-V* curves visibly overlap showing no difference in their shape. This is an interesting result which shows that the bending or the strain does not affect to the transport energy barrier alignment Δ at the metal/organic interfaces. Interpolating the linear fit of the growth of I_C to I_C=0, Au/C_{60} interface energy barrier is determined to be $\Delta = \mathbf{0.9 \pm 0.1\ V}$. This value is in agreement with results reported in ref.[15] where the Au/C_{60} interface energy barrier has been measured by i-MOS device grown on rigid Si_2O_3 substrate. Following the described fitting method, in Figure 6d we determine that the interface energy barrier between Au/PTCDI-C8 is $\Delta = \mathbf{1.1 \pm 0.1\ V}$.

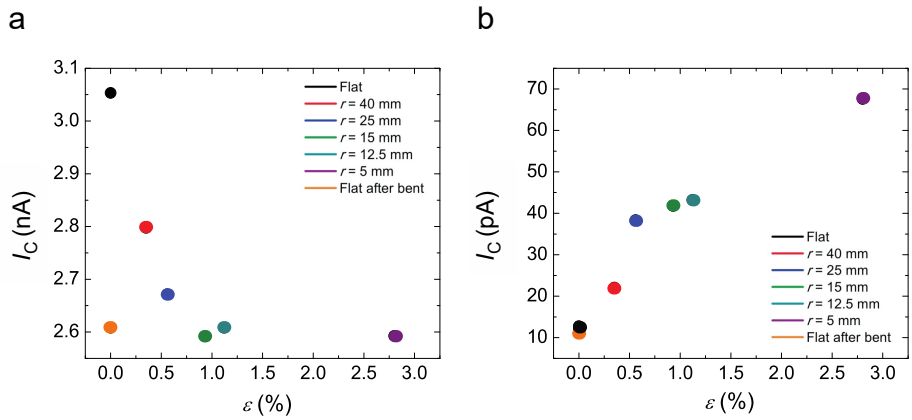

Figure 5.7| Energy barrier extraction. a, Hot electron current, I_C, as a function of the applied bias between the emitter and the base V_{EB} at 300 K and the linear fit to I_C = 0 to obtain the energy barrier height Δ of the Au/C_{60} interface. **b**, I_C as a function of V_{EB} at 300 K and the linear fit to I_C = 0 for the extraction of the Au/PTCDI-C8 interface energy barrier.

The differences between devices with C_{60} and PTCDI-C8 come with the trend of the I_C current. The current shows an order of magnitude difference from C_{60} to PTCDI-C8 based device, being the first the one of the highest I_C current value. It is a counterintuitive result considering that both devices are built onto similar device architecture and that I_E and I_{diode} of both

devices measured in the previous sections are of the same order of magnitude. In other words, the current reaching the Au/molecular interface is of the same order for both devices. Moreover, the samples have the same collector thickness and both C_{60} and PTCDI-C8 molecules have equivalent charge carrier mobility [16,17].

Additionally, in the case of the C_{60} device (Figure5.6a), I_C slightly decreases with the bending, showing a maximum change of 15% between measuring it flat or with r = 5mm. However, the second device, the PTCDI-C8 based i-MOS, does not show that decreasing trend. Indeed, in the last case I_C increases with the applied strain showing a 430% higher I_C when the device is bent with r = 5mm than when it is flat. Figure 5.5 shows the described trend of the measured I_C with the bending radius for both, C_{60} (Figure 5.7a) and PTCDI-C8 (Figure 5.7b) based i-MOS devices. This is not the case for two-terminal diode measurements, where in the two cases the current decreases with increasing strain.

5.3 Simulations

We have collaborated with the group of Prof. Michel Flatté (Iowa University) who have performed some simulations to give an answer to our experimental observations. The simulations are still not fully conclusive, but the preliminary results seem to indicate that in the case of planar molecules, such as PTCDI-C8, the cores are composed of conjugated ring-like segments with spatial orientation defined by an axis parallel to the un-hybridized orbitals while in the case of spherical molecules, such as C_{60}, the spatial orientation of LUMO is not well defined. In the first case where the spatial orientation is defined, the tensile strain will change the molecular orientation, which in turns affects the transport properties of the material. For a deformed material the molecular unit cell is strained and as a result the volume is, in general, augmented modifying the volumetric density of states.

Current thought the organic layer exhibits hopping conduction along a path of sites with each hop occurring at a rate that depends on the relative position and orientation of the initial and final site. These rates are analogous to resistors in series. Since the bulk resistance is determined by summing the individual resistances along the path and thus, the hopes

between sites with relative orientation near perpendicular will dominate the total value. These bottlenecks that exist in the relaxed organic will be broken as the device is bent and the sites shift their relative position and orientation. Consequently, bending causes a drop of the resistivity of the molecular layer and we observe as an augmentation of the I_C current in the PTCDI-C8 device.

5.4 Conclusions

In this work we have been able to successfully fabricate hot-electron devices on flexible Kapton substrates based on Au/PTCDI-C8/Al and Au/C_{60}/Al structures. The performance of the devices has been proved when the samples were flat (no strain) and bent (under strain). Subsequently, we have demonstrated that the metal/molecular interface energy barrier, Δ, is strain independent, i.e. $\Delta = 0.9 \pm 0.1$ eV of Au/C_{60} and $\Delta = 1.1 \pm 0.1$ eV of Au/PTCDI-C8 do not vary when the samples are bent.

However, we have noticed differences in the trend of the amplitude of the I_C current between devices with different molecular species. In other words, we observed that the I_C current increases with the bending in the case of PTCDI-C8 devices while hardly changes in the case of C_{60} based i-MOS. The simulations run by our collaborators from Iowa University indicate that the differences are geometry related. In the case of PTCDI-C8 the molecular orbitals are spatially oriented, and the tensile strain changes the molecular orientation. In turn, the hopping of the charges is speed up and consequently, an increase of the I_C current is detected. In the case of C_{60}, the spatial orientation of LUMO level is not well defined and thus, bending does not affect to transport properties.

References

1. Rogers, J. A., Someya, T. & Huang, Y. Materials and mechanics for stretchable electronics. *Science (80-.).* **327,** 1603–1607 (2010).
2. Sekitani, T., Zschieschang, U., Klauk, H. & Someya, T. Flexible organic transistors and circuits with extreme bending stability. *Nat. Mater.* **9,** 1015–1022 (2010).
3. Wang, Y. *et al.* A highly stretchable, transparent, and conductive polymer. *Sci. Adv.* **3,** 1602076–1602086 (2017).
4. Xu, J. *et al.* Highly stretchable polymer semiconductor films through the nanoconfinement effect. **355,** 59–64 (2017).
5. Hwang, J., Wan, A. & Kahn, A. Energetics of metal – organic interfaces : New experiments and assessment of the field. *Mater. Sci. Eng. R* **64,** 1–31 (2009).
6. Braun, S., Salaneck, W. R. & Fahlman, M. Energy-Level Alignment at Organic / Metal and Organic / Organic Interfaces. **21,** 1450–1472 (2009).
7. Wu, Y. *et al.* Strain effects on the work function of an organic semiconductor. *Nat. Commun.* **7,** 10270–10278 (2016).
8. Yang, X. *et al.* Highly Flexible, Electrically Driven, Top-Emitting, Quantum Dot Light- Emitting Stickers. *ACS Nano* **8,** 8224–8231 (2014).
9. Sun, X., Bedoya-Pinto, A., Llopis, R., Casanova, F. & Hueso, L. E. Flexible semi-transparent organic spin valve based on bathocuproine. *Appl. Phys. Lett.* **105,** 083302-4 (2014).
10. Briseno, A. L. *et al.* Patterning organic single-crystal transistor arrays. *Nature* **444,** 913–917 (2006).
11. Bedoya-Pinto, A., Donolato, M., Gobbi, M., Hueso, L. E. & Vavassori, P. Flexible spintronic devices on Kapton. *Appl. Phys. Lett.* **104,** 062412-5 (2014).
12. Suo, Z., Ma, E. Y., Gleskova, H. & Wagner, S. Mechanics of rollable and foldable film-on-foil electronics. *Appl. Phys. Lett.* **74,** 1177–1179 (1999).
13. Sekitani, T. *et al.* Bending experiment on pentacene field-effect transistors on plastic films. *Appl. Phys. Lett.* **86,** 073511–073514 (2005).
14. Sun, X. *et al.* Room temperature air-stable spin transport in bathocuproine-based spin valves. *Nat. Commun.* **4,** 2794–7 (2013).

15. Gobbi, M. *et al.* Determination of energy level alignment at metal/molecule interfaces by in-device electrical spectroscopy. *Nat. Commun.* **5,** 4161–4168 (2014).

16. Kobayashi, S., Takenobu, T., Mori, S., Fujiwara, A. & Iwasa, Y. C60thin-film transistors with high field-effect mobility, fabricated by molecular beam deposition. *Sci. Technol. Adv. Mater.* **4,** 371–375 (2003).

17. Mao, L. K., Gan, J. Y., Hwang, J. C., Chang, T. H. & Chueh, Y. L. The role of water in the device performance of n-type PTCDI-C8 organic field-effect transistors with solution-based gelatin dielectric. *Org. Electron.* **15,** 920–925 (2014).

Chapter 6

Final Conclusions & Outlook

In this thesis we study and further develop in-device molecular spectroscopy for the study of metal/organic interface energy barriers. The technique has been proven with solution processed and evaporated molecules, rigid and flexible substrates with a common objective: determining molecular levels in-device operative conditions and understanding how metal/organic semiconductor interface energy barriers are affected by external factors such as tension. This leads us exploring charge transport effects at these interfaces.

In Chapter 3, we study the energy level alignment at the interface between gold and electron transporting solution processed N2200 polymer. We compare our results with the ones obtained by UPS for the same interfaces to conclude that i-MOS is a reliable and straightforward method for the determination of metal/polymeric semiconductor bulk energy barriers. We highlight that our technique is especially convenient for n-type polymers where UPS requires complex assumptions. Moreover, we have also conclude that the contamination layer coming from the air exposure of the devices in the fabrication process does not play a significant role in the bulk energy barrier.

In Chapter 4, we explore the energy alignment at Au/C_{60} and Au/C_{70} interfaces. We extend the functionality of i-MOS technique to report an unprecedented full energy characterization of both hole and electron transport levels with respect to the metal contacts. Playing with injection

bias and the electric potential through the organic semiconductor, we are able to detect direct electron and hole current as well as secondary charge current coming from inelastic or Auger like scattering mechanisms. This enables us accessing not only LUMO of the semiconductors but also HOMO and LUMO+1. Thus, we can calculate the transport gap of the organic semiconductors in device operative conditions, without any prior material parameter and using a single vertical device. Moreover, the high-energy carrier injection permits accessing by electronic transport the Marcus Inverted Regime. This regime is directly observable as a negative differential resistance in the three terminal i-MOS measurements, where temperature, electric field across the semiconductor and light permits its manipulation. We have performed control experiment with PTCDI-C8, which contrary to C_{60} and C_{70} has high reorganization and disorder energies. In agreement with theory, no NDR arising from Marcus Inverted Regime is observed with PTCDI-C8.

In Chapter 5, we successfully fabricate hot-electron devices on flexible Kapton substrates based on Au/PTCDI-C/Al and Au/C_{60}/Al junctions. The devices have been proven to perform when they are flat (no strain) and bent (under strain). Subsequently, we have demonstrated that the metal/molecular interface energy barrier is strain independent and thus, do not vary whit bending angle. These results imply that the study of the metal/molecular interface energy barrier can be accomplished with rigid i-MOS with no need of adding the complication of fabricating them on flexible substrates. However, we observe that while the amplitude of the current in C_{60} based devices is barely affected by the strain, the current increases with when PTCDI-C8 based i-MOS are bent. In the case of the last material the molecular orbitals are spatially oriented, and the tensile strain changes the molecular orientation. In turn, the hopping of the charges is speed up and consequently, the I_C current increases. In the case of C_{60}, the spatial orientation of LUMO level is not well defined and thus, bending does not affect to transport properties.

The work of this thesis contributes to the understanding of metal/organic interface energy barriers and the charge transport through them by i-MOS. Nevertheless, i-MOS still offers plenty of possibilities to explore:

- i-MOS is an in-device spectroscopic technique that permits determining the energy barrier at metal/semiconductor interfaces and the transport energy gap of the molecular layers in device operative conditions. Nevertheless, in this thesis we have only focused in electron transporting semiconductors. Exploring p-type, ambipolar molecular semiconductors and blends are the next natural steps. Besides, photochromic molecules are interesting molecular species to study with i-MOS. The molecules orbital levels shift in energy when light is shine. The integration of photochromic molecules in i-MOS and performing measurements with and without light, will test the energy resolution of i-MOS.
- The effective NDR arising from the Marcus Inverted Regime can open new possibilities that still need to be exploited both, from fundamental physics point of view but also from applied electronics. Testing more materials will contribute to better understand the parameters that limits the observation of this effect and a solid theory that describes the effect should be build. There can be also other parameters than temperature, light and electric field that could be explore. Following up the work we have done with flexible i-MOS, strain might be a good candidate for manipulating MIR.
- In this thesis we studied the effect of the tensile strain at metal/organic semiconductor interface energy barrier. It would be interesting to investigate the effects of the compressive strain in the energetics of metal/organic semiconductor systems.
- Self-assembled monolayers or thin molecular layers between the base and the bulk semiconductor might reveal how long charges travel ballistically in the organic semiconductor and if i-MOS is an interface sensitive spectroscopic technique.
- Organic semiconductor heterojunctions are present in most organic optoelectronic devices, such as OLEDs and OPEVs. Besides the energy barriers at metal/organic semiconductor interfaces, these devices require the determination of the energy barriers between two semiconductors. i-MOS is a potential spectroscopy technique for the determination of semiconductor/semiconductor interface energy barriers in device operative conditions. Keeping the i-MOS structure, one can put in contact two semiconductors as collector. In this way and

playing with the V_{CB} bias, one should measure onsets that corresponds to the metal/semiconductor and semiconductor/semiconductor interface energy barriers.

Appendix A

PTCDI-C8 based i-MOS characterization

Device fabrication

These i-MOS devices consist of 12nm-thick aluminium (99.95% purity, Lesker) emitter, which was thermally evaporated with a rate of 0.6 Å s^{-1}. Then, Al_2O_3 tunnel junction was made by plasma oxidizing the aluminium contact, first for two minutes at low power (1200V and 10 mA at 0.1 mbar) and then for three minutes at high power (1200V and 50 mA at 0.1 mbar). 10 nm-thick gold (99.95% purity, Lesker) was e-beam evaporated at 1.0 Å s^{-1} as the base contact. 200 nm of n-type PTCDI-C8 (98%, Sigma Aldrich), was thermally evaporated with a rate of 0.1 Å s^{-1}. Finally, 12 nm-thick aluminium, which has a good matching with LUMO of PTCDI-C8, was again thermally evaporated as top electrode. A two-step deposition has been followed in order to minimize the damage to the organic film: first, 4 nm

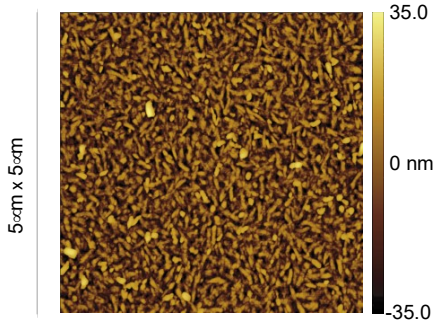

Figure A.1| Characterization of PTCDI-C8 films. 5 µm x 5 µm surface topography of 200 nm thick PTCDI-C8 film extracted by atomic force microscopy (AFM).

thick aluminium at 0.1 Å s^{-1} in order to cover the surface roughness (see the AFM image in Figure A.1) and avoid the penetration of energetic metallic atoms. Then, 0.6 Å s^{-1} rate evaporation until total film thickness of 12 nm to avoid burning the organic surface due to a prolonged evaporation time.

Device characterization

In this section the current-voltage (*I-V*) characteristics of PTCDI-C8 based i-MOS devices are shown. Figure A.1a shows the emitter-base current I_E flowing through the tunnel junction when the voltage V_{EB} is swept between the emitter and the base for temperatures from 300 K to 120 K. This non-linear *I-V* trace is typical of tunnel junctions. The resistance slightly increases when lowering the temperature, as expected for continuous tunnel junctions.

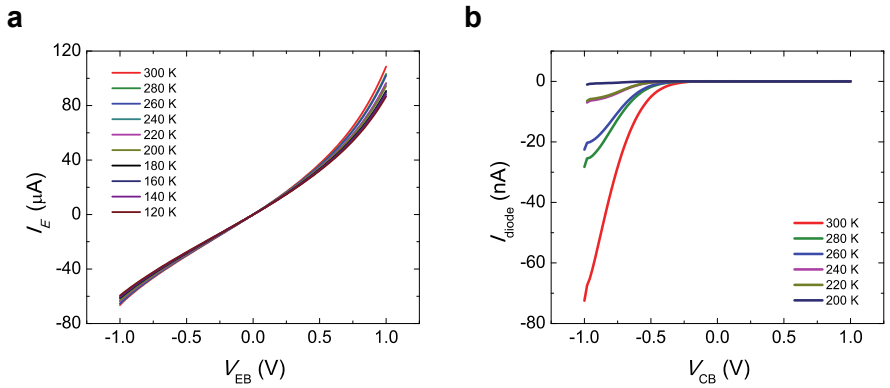

Figure A.2| Electrical characterization of device counterparts. a, Current I_E measured at two terminals in the $Al/Al_2O_3/Au$ tunnel junction as function of the applied bias between emitter and base, V_{EB}, for 300 K-120 K temperature range. **b**, Temperature dependence of I_{diode} current measured at two terminals in the $Au/C_{60}/Al$ stack as function of the applied bias between the base and the collector V_{CB} from 300 K. to 120 K.

In Figure A.2b we show I_{diode}- V_{CB} of Au/PTCDI-C8/Al stack for 300 K - 120 K temperature range. The 200 nm thick PTCDI-C8 layer is highly resistive and the *I-V* curve is again highly non-linear. In other words, the top aluminium contact injects more electrons to the organic layer (negative V_{CB}) than what gold base contact does (positive V_{CB}). This suggests lower barrier for

electron injection to the semiconductor from aluminium than from gold. Lower the temperature higher the resistivity of I_{diode}-V_{CB} curves, typical transport feature of thick layer molecular semiconductors.

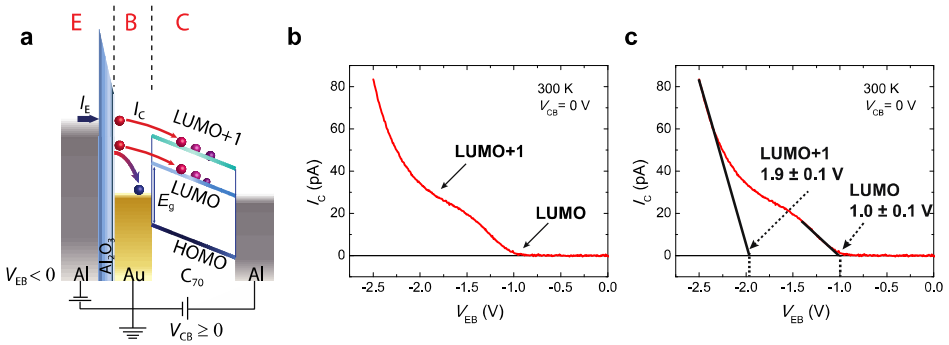

Figure A.3| Hot-electron current of the device. a, Schematic representation of the direct process in which electrons are injected by applying a negative emitter-base bias, $V_{EB} < 0$ V, and detected in the molecular semiconductor. The measurements can be performed either without any externally applied base collector bias, V_{CB}, or by $V_{CB} \geq 0$V. **b**, Collector current I_C for $V_{EB} < 0$ V at room temperature. Energetic electrons are injected with $V_{CB} = 0$V both into the lowest molecular orbital (LUMO) and into the first excited conductive molecular level (LUMO+1) of PTCDI-C8. **c**, Linear fitting of I_C with $V_{EB} < 0$ V at $V_{CB} = 0$ V for the extraction of the energy of LUMO and LUMO+1 of C_{60} at 1.0 ± 0.1 V and 1.9 ± 0.1 V, respectively.

Figure A.3a shows the working principles of i-MOS together with the measured current in the collector I_C for negative voltage biases between the emitter and the base, V_{EB}. This process is shown in Figure A.3b, where I_C versus V_{EB} for $V_{CB} = 0$V is plotted. Two onsets corresponding to the relative position of molecular orbitals devoted to electron transport, LUMO and LUMO+1, are observable. The linear fittings of the increment of I_C enabled extracting the energies of LUMO and LUMO+1 of PTCDI-C8 relative to the Fermi level of gold. This is possible due to linear dependence of I_C with the energy barrier Δ i.e. $I_C \propto (e|V_{EB}| - \Delta)$. Figure A.3c shows the mentioned linear fitting, that leads to the determination of 1.0 ± 0.1 eV and 1.9 ± 0.1 eV for LUMO and LUMO+1 with respect to gold. Figure A.4 shows the temperature dependence of I_C form 300 K to 120 K. A soft decrease of one order of magnitude is observed from the highest to the lowest temperature. In Figure A.5 the positive collector base bias, V_{CB}, dependence of I_C is

presented. I_C is augmented in a factor five with V_{CB} = 2.0 V with respect to V_{CB} = 0 V.

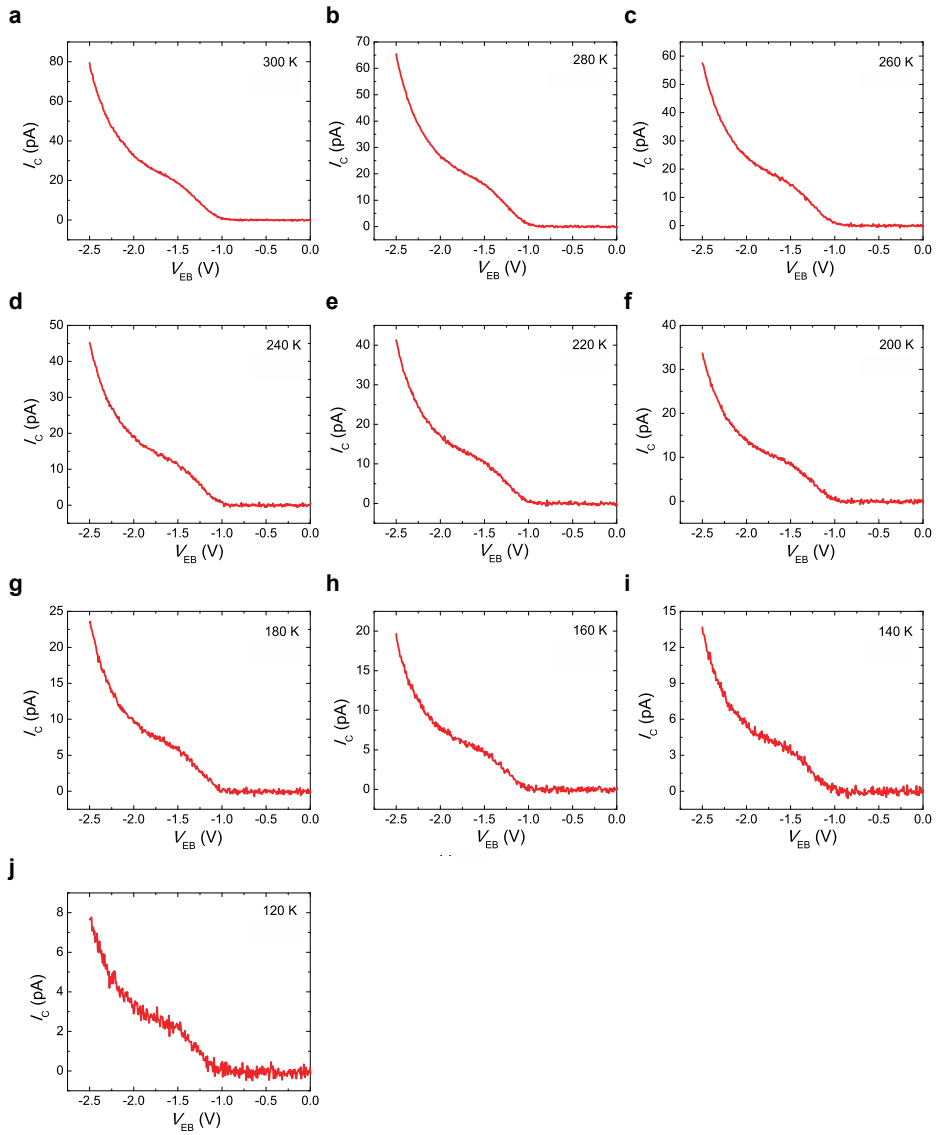

Figure A.4|Collector current IC for negative emitter-base bias VEB < 0 V at temperatures from 300 K to 120 K for in-device molecular spectroscopy (i-MOS) with Au/PTCDI-C8 interface. Energetic electrons are injected and detected with V_{CB} = 0 V into the lowest molecular orbital (LUMO) and first excited conductive molecular level (LUMO+1) of PTCDI-C8 (**a-k**).

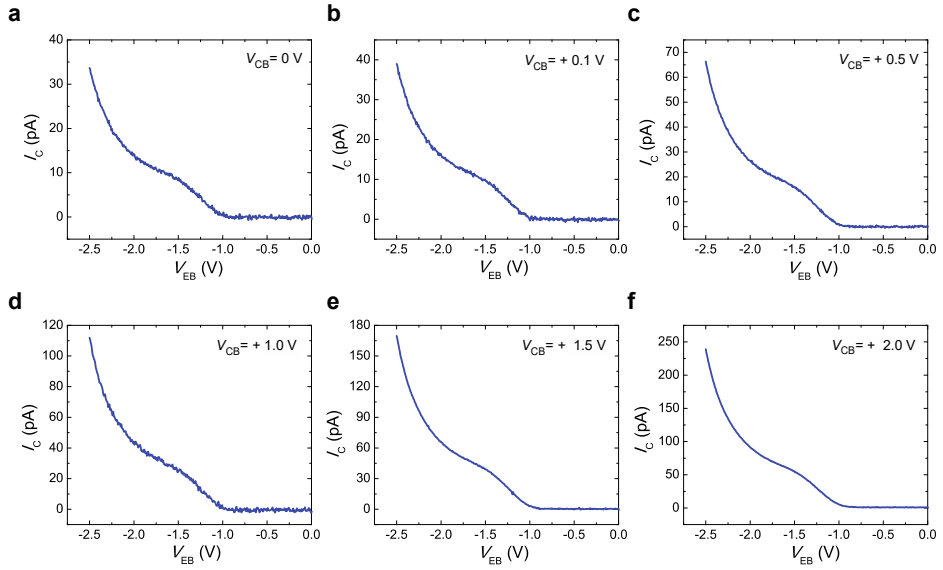

Figure A.5| Collector current IC for positive emitter-base bias V_{EB} > 0 V at 200 K in a Au/PTCDI-C8 based i-MOS device. Applying a positive collector-base bias V_{CB} > 0 V energetic electrons are injected into the lowest molecular orbital (LUMO) and first excited conductive molecular level (LUMO+1) (**a**-**g**).

List of acronyms

UHV	Ultra high vacuum
LUMO	Lowest unoccupied molecular orbital
HOMO	Highest occupied molecular orbital
OLED	Organic light emitting diodes
OPV	Organic photovoltaics
OFET	Organic field effect transistors
E_F	Fermi energy
E_{vac}	Vacuum level
ϕ_M	Metal work function
IE	Ionization energy
EA	Electron affinity
Λ	Interface dipole
E_G	Energy gap
Δ_{LUMO}	Energy of LUMO with respect to E_F of a metallic contact
Δ_{HOMO}	Energy of HOMO with respect to E_F of a metallic contact
IDIS	Induced density of interface states
PES	Photoemission spectroscopy
IPES	Inverse photoemission spectroscopy
BEEM	Ballistic electron-emission spectroscopy
i-MOS	In-device molecular spectroscopy
STM	Scanning tunnelling microscopy
XPS	X-ray photoemission spectroscopy
UPS	Ultraviolet photoemission spectroscopy
E_{cutoff}	Secondary electron cutoff
AFM	Atomic force microscope
E	Electron
eV	Electron volt
T	Temperature

k_B	Boltzmann constant
I_T	Tunnelling current
I_B	Base current
V_T	Tunneling voltage
E	Emitter
B	Base
C	Collector
I_E	Emitter current
I_C	Collector current
V_{EB}	Emitter-base bias
V_{CB}	Collector-base bias
$k_{\parallel}$	Parallel component of the linear momentum
$k_{\perp}$	Perpendicular component of the linear momentum
λ	Attenuation length
λ_i	Inelastic attenuation
λ_e	Elastic attenuation
d	Thickness
UV-VIS	Ultraviolet-visible spectroscopy
XRD	X-ray diffraction
DOS	Density of states
NDR	Negative differentia resistance
MNR	Marcus normal region
MIR	Marcus inverted region
RMS	Root mean square
I_{CT}	Integer charge transfer
DOS	Density of states

Acknowledgements

I would like to finish my thesis mentioning and acknowledging all the people who have been with me during these four years and thus, have made it possible.

First of all, I would like to acknowledge Prof. Txema Pitarke for giving me the opportunity to work in nanoGUNE during my summer internship, master degree and Ph.D. I also acknowledge Basque Government and nanoGUNE for the financial support during these years.

I want to express my sincere gratitude to my supervisor Prof. Luis E. Hueso for his constant support and guidance. Durante estos años me has dado la libertad de pensar y probar ideas nuevas; me has enseñado lo que es la ciencia y cómo ser parte de ella. Te agradezco enormemente la oportunidad que me brindaste de trabajar contigo hace ya casi cinco años. I would also like to thank Prof. Felix Casanova for fruitful discussion and kindness. Os agradezco mucho a los dos la confianza que habéis depositado en mi para llevar a cabo este estupendo proyecto con el que he podido aprendido tanto.

Many thanks to all the members (former and current) of the Nanodevices group for contributing to the excellent working atmosphere that we have had. To our technician, Roger, because you are the most fundamental person in the lab and without your technical support working in the lab would not be possible. ¡Gracias por ayudarme y enseñarme a solucionar problemas en laboratorio, por hacerme unas figuras tan chulas y por ser siempre tan amable! To Marco, because he introduced me to the topic of organic semiconductors and in particular to hot-electron devices in my summer internship. ¡Gracias por ser mi primer mentor! To Subir, for his unconditional support. Thank you for sharing your knowledge with me, all the fruitful discussions we had, not only about science but also about life, and for helping me every time I needed! To Prof. Xiangnan Sun, because he

supported and motivated me when things were not so easy. You taught me how to work and think in science but most importantly you showed me that hard work has its reward! To Mario, for the fascinating experiments we have done together! You were not only a great workmate, but also a friend! To Elisabetta, for her constant support and all the beautiful moments we have shared and will share in the future! questi due anni e mezzo ho potuto incontrare una persona fantástica che mi fa ridere e mi ha sempre supportato! To Maider, thank you for being my table companion these last months! ¡Gracias por nuestras reflexiones sobre la vida, la sociedad y los cotilleos! ¡He descubierto una persona estupenda con muchísimas cosas en común! :) To Kaushik, for being always ready to discuss! Thank you for sharing your ideas and experience! To Francesco, for being such an active person! ¡Te deseo lo mejor como el nuevo hot-electron guy! To Edurne, for her smile and kindness! Lanera etortzea errazagoa da zu bezalako lankide eta lagunekin! To Juanma and Josu, Zipy y Zape, because they are the salt and pepper of this group! ¡Mil gracias a los dos por hacerme reír tanto y en especial a Juanma por escucharme siempre que lo he necesitado! To Inge, for being always so kind! Thank you for suggestions about Barcelona and the Netherlands, and for helping me whenever you could! To Sara, Pep, Tuong, Safeer, Nerea, María, Oihana, Wenjing, Miren, Estitxu, Xabi, Santi and the other members of the group, for making this period of my life worthwile!

Lots of thanks to all the nanopeople! Especially to Eider for the help with the administration and the nice moments we have shared in and out of nanoGUNE! Ez ditut inoiz ahatuzko Madalenetako gaua ezta Lekittora eginiko bisitak!

I would also like to acknowledge the people who I had the opportunity to collaborate with, such as Dr. Frank Ortmann and Dr. Thorten Arnold, for their theoretical support; Prof. Mats Fahlman, for the UPS experiments, Prof. Mirko Cinchetti, for fruitful discussion and Stephen McMillan, for the simulations of the flexible devices. I also want to acknowledge people from Polymat, especially Cristian and Gabriella, because it was always nice to share time with them in the lab!

Finally, my greatest acknowledgements goes to those who have always believed in me. Aita, ama eta Unai eskerrik asko nire bidea eraikitzen lagundu izanagatik, nire bizitzako zutabeak zarete! And of course to Marc, for making my life so beautiful. Vous m'avez apporté un soutien chaque jour

de ce voyage; dans les bons et les mauvais moments, vous avez toujours été avec moi!

Thank you! Eskerrik asko! ¡Gracias! Merci! Grazie! Gràcies! Obrigado! Grazas! Bedankt! Danke! Dank je! Cảm ơn! ধন্যবাদ! धन्यवाद!谢谢！

Ainhoa, 2018ko iraila.

List of publications

This thesis is based in the following publications:

- *Energy Level Alignment at Metal/Solution-Processed Organic Semiconductor Interfaces.*
  A. Atxabal, S. Braun, T. Arnold, X. Sun, S. Parui, X. Liu, C. Gozalvez, R. Llopis, A. Mateo-Alonso, F. Casanova, F. Ortamnn, M. Fahlman & L. E. Hueso, *Adv. Mater.* **29**, 1606901 (2017).
  (Chapter 3)

- *Molecular spectroscopy and observation of the Marcus inversion regime in a solid-state device.*
  A. Atxabal, A. Thorsten, S. Parui, E. Zuccatti, M. Cinchetti, F. Casanova, F. Ortmann & L.E. Hueso, *Submitted.* (2018).
  (Chapter 4)

- *Marcus Inverted Regime in solid state devices.*
  A. Atxabal, A. Thorsten, F. Casanova, F. Ortmann & L.E. Hueso, *in preparation* (2018).
  (Chapter 4)

- *Strain dependence of energy level alignment at metal/molecular semiconductor interfaces.*
  A. Atxabal, S. Parui,. Casanova, F. Ortmann & L.E. Hueso, *in preparation.* (2018).
  (Chapter 5)

Other publications:

- *Gate-tunable graphene-organic interface barrier for vertical transistor and logic inverter*
  S. Parui, M. Ribeiro, A. Atxabal, K. Bairagi, E. Zuccatti, C. K. Safeer, R. Llopis, F. Casanova, L. E. Hueso, Accepted in *Appl. Phys. Lett.* (2018)
- *Boron nitride nanoresonators for phonon-enhanced molecular vibrational spectroscopy at the strong coupling limit.*
  M. Autore, P. Li, I. Dolado, F. Javier Alfaro-Mozaz, R. Esteban, A. Atxabal, F.Casanova, L. E. Hueso, P. Alonso-González, J. Aizpurua, A. Y. Nikitin, S. Vélez and R .Hillenbrand, *Light Sci. Appl*. **7**, 17172 (2018).
- *Hot Electrons and Hot Spins at Metal-Organic Interfaces*
  A. Thorsten, A. Atxabal, S. Parui, L.E. Hueso and F. Ortmann, *Adv. Funct. Matter.* **28**, 1706105 (2018).
- *Interface-Assisted Sign Inversion of Magnetoresistance in Spin Valves Based on Novel Lanthanide Quinoline Molecule.*
  A.Bedoya-Pinto, S. G Miralles, S. Vélez, A. Atxabal, P. Gargiani, M. Valvidares, F. Casanova, E. Coronado & L. E Hueso, *Adv. Funct. Matter*. **28**, 702099 (2018).
- *A molecular spin-photovoltaic device*
  X. Sun, S. Vélez, A. Atxabal, A. Bedoya-Pinto, S. Parui, X. Zhu, R. Llopis, F. Casanova & L. E. Hueso, *Science* **357**, 677 (2017).
- *Graphene as an electrode for solution-processed electron-transporting organic transistors.*
  S. Parui, M. Ribeiro, A. Atxabal, R. Llopis, F. Casanova & L.E. Hueso, *Nanoscale* **9**, 10178 (2018).
- *Synthesis and Properties of a Twisted and Stable Tetracyano-Substituted Tetrabenzoheptacene.*
  M. Martínez-Abadía, G. Antonicelli, E. Zuccatti, A. Atxabal, M. Melle-Franco, L. E. Hueso & A. Mateo-Alonso, *Org. Lett.* **19**, 1718 (2017).
- *Spin Doping Using Metal Phthalocyanine Molecules.*
  A. Atxabal, M. Ribeiro, S. Parui, L. Urreta, E. Sagasta, X. Sun, R. Llopis, F. Casanova & L.E. Hueso, *Nat. Commun.* **7**, 13751 (2016).
- *K-Conjugated Dibenzoazahexacenes*

G. Antonicelli, C. Gozalvez, A. Atxabal, M. Melle-Franco, L. E. Hueso & A. Mateo-Alonso, *Org. Lett.* **18**, 4694 (2016).

- *Frequency driven inversion of tunnel magnetoimpedance and observation of positive tunnel magnetocapacitance in magnetic tunnel junctions.*
  S. Parui, M. Ribeiro, A. Atxabal, A. Bedoya-Pinto, X. Sun, R. Llopis, F. Casanova & L. E. Hueso*, Appl. Phys. Lett.* **109**, 052401 (2016).

- *A Bis(triisopropylsilylethynyl)-Substituted Pyrene-Fused Tetraazaheptacene: Synthesis and Properties.*
  A. B. Marco, C. Gozalvez, M. Olano, X. Sun, A. Atxabal, M. Melle-Franco, L. E. Hueso & A. Mateo-Alonso, *Phys. Chem. Chem. Phys.* **18**, 11616 (2016).

- *Active Morphology Control for Concomitant Long Distance Spin Transport and Photoresponse in a Single Organic Device.*
  X. Sun, A. Bedoya-Pinto, Z. Mao, M. Gobbi, W. Yan, Y. Guo, A. Atxabal, R. Llopis, G. Yu, Y. Liu, A. Chuvilin, F. Casanova & L. E. Hueso, *Adv. Mater.* **28**, 2609 (2016).

- *Reliable determination of the Cu/n-Si Schottky barrier height by using in-device hot-electron spectroscopy.*
  S. Parui, A. Atxabal, M. Ribeiro, A. Bedoya-Pinto, X. Sun, R. Llopis, F. Casanova & L. E. Hueso, *Appl. Phys. Lett.* **107**, 183502 (2015).

- *An electron-conducting pyrene-fused phenazinothiadiazole.*
  A. B. Marco, D. Cortizo-Lacalle, C. Gozalvez, M. Olano, A. Atxabal, X. Sun, M. Melle-Franco, L. E. Hueso & A. Mateo-Alonso, *Chem. Comm.* **51**, 10754 (2015).

- *Determination of energy level alignment at metal/molecule interfaces by in-device electrical spectroscopy.*
  M. Gobbi, L. Pietrobon, A. Atxabal, A. Bedoya-Pinto, X. Sun, F. Golmar, R. Llopis, F. Casanova & L.E. Hueso, *Nat. Commun.* **5**, 4161 (2014).